University of Liège

Doctoral Thesis

Dynamic Stall modelling at low Reynolds Numbers

Author:
Johan Boutet

Supervisor:
Prof. Grigorios Dimitriadis

A thesis submitted in fulfillment of the requirements for the degree of Doctor of Philosophy

Aerospace & Mechanical engineering department

December 22, 2020

"*Not all those who wander are lost*"

J.R.R.Tolkien

UNIVERSITY OF LIÈGE

Abstract

Faculty of applied science
Aerospace & Mechanical engineering department

Doctor of Philosophy

Dynamic Stall modelling at low Reynolds Numbers

by Johan BOUTET

Dynamic stall is described by Mac Croskey et al. [1], [2] as a phenomenon that occurs on airfoils subjected to unsteady motion with high amplitude or frequency. The phenomenon occurs at higher angles of attack and lift values than steady stall. Dynamic stall can also be associated with the shedding of a vortex from the leading edge. This vortex usually affects the flow around the airfoil such that it increases further the instantaneous lift acting on the wing and produces a nose down pitching moment when the vortex is swept toward the trailing edge. The modeling of dynamic stall is challenging even in 2D because it involves separated and turbulent flow. Typical 2D approaches range from semi-empirical, such as the Leishman-Beddoes (LB) [3] or the ONERA models, [4], [5] to Computational Fluid Dynamic (CFD) methods.

This thesis makes two major contributions towards the development of a dynamic stall model for 3D wings at low Reynolds number based on the 2D Leishman-Beddoes model. The LB model has not been conceived with very low Reynolds number in mind. The first contribution of this thesis is the development of a modified Leishman-Beddoes model able to handle dynamic stall at low Reynolds number ranges. It uses Wagner theory for the incompressible attached flow and adapts the stall onset criterion by Sheng et al to low Reynolds numbers. In order to calibrate and validate the model, an extensive set of dynamic stall experiments were carried out in a low-speed wind tunnel for three airfoils: a flat plate, a NACA0012 wing, and a NACA0018 wing. This modified Leishman-Beddoes model results in better aerodynamic load predictions than the original model for low and medium reduced pitch rates. For the highest reduced pitch rates, neither model yields fully satisfactory predictions.

The second contribution is the development of a closed-form unsteady attached flow model for 3D wings. It combines the 2D Wagner unsteady aerodynamic loads calculation with Prandtl's lifting line, by means of the unsteady Kutta-Joukowsky theorem. This new model was validated by means of comparison to the predictions of an unsteady vortex lattice model for impulsive and oscillatory motions of wings of different planforms and aspect ratios. An additional validation involved the calculation of the flutter speed and frequency of finite rectangular wings with pitch and plunge degrees of freedom and comparison to the predictions of an aeroelastic vortex lattice formulation.

Acknowledgements

I want to thank professor Dimitriadis for his guidance and his support during my work on this thesis. I found his friendliness very helpful. He quickly managed to ease the nervous person I am. I also thank Xavier Amandolese for the opportunity he gave me to perform the experiments I used to validate my models, in the present work. Lastly, I thank professor Kerschen for financing this thesis with his ERC grant.

I thank my mother, a true force of nature, who is the pillar holding me when I was at my lowest. She has always been there with care and support. Even if she doesn?t always understand what I'm talking about. I love you, mom.

I believe my anxiety and depression have been brewing out of control for quite a few years. The writing of this thesis was merely the final blow that knocked me out of balance. I will forever thank Dr. Mourad for his help to get me back on my feet, as well as my therapist, Virginie Smets, who helped me get back on track and finish what was left of my thesis.

With Covid pushing us toward new forms of socializing, I would like to thank the online friends I made recently. They have been a great source of comfort and support while I resumed my thesis.

Contents

Abstract iii

Acknowledgements v

1 Introduction 1
1.1 2D Dynamic stall . . . 1
1.1.1 Static stall . . . 1
1.1.2 Dynamic stall . . . 4
1.2 Models . . . 8
1.3 3D dynamic stall . . . 10
1.3.1 3D lift distribution . . . 10
1.3.2 lifting line . . . 10
1.3.3 Stall cells . . . 12
1.3.4 Omega vortex shedding . . . 13
1.4 Objectives of this thesis . . . 14
1.5 Outline of this thesis . . . 14

2 Leishman-Beddoes 17
2.1 State space Leishman-Beddoes model . . . 17
2.1.1 Attached flow . . . 17
2.1.2 Vortex onset . . . 20
2.1.3 Trailing edge separation . . . 21
Computation of $s(\alpha)$ . . . 21
Computation of $g(s)$ . . . 22
Dynamic effects on $s(\alpha)$ and $g(s)$ . . . 23
2.1.4 Dynamic stall modelling . . . 24
2.1.5 Coupling of the stall mechanisms . . . 25
2.1.6 Complete equations . . . 26
2.2 Modified Leishman-Beddoes model . . . 27
2.2.1 Attached flow module . . . 28
Circulatory lift . . . 28
Impulsive loads . . . 31
2.2.2 Detached flow module . . . 31
Computation of $s(\alpha)$ . . . 32
Computation of $g(\alpha)$ . . . 33
Cubic spline curve fit . . . 34
2.2.3 Dynamic stall module . . . 35
Dynamic stall onset . . . 36
Dynamic stall and stall delay . . . 39
Leading edge vortex . . . 40
Estimation of T_{vl} . . . 40
2.2.4 Unsteady flow module . . . 42
Loads associated with trailing edge separation . . . 42

Circulation change . . . 42
Vortex shedding effects . . . 43
2.2.5 Complete equations . . . 43

3 Application of the modified LB model 45
3.1 Experimental setup . . . 45
3.1.1 Three wing models . . . 45
3.1.2 Measurement setup . . . 46
3.2 Data processing . . . 47
3.3 Static stall experiments . . . 48
3.4 Dynamic stall experiments . . . 50
3.4.1 Prescribed pitch motion . . . 50
3.4.2 Dynamic stall onset criteria . . . 50
3.4.3 Flat plate Dynamic stall onset . . . 52
3.5 Vortex shedding . . . 54
3.6 Validation of the modified Leishman-Beddoes model . . . 55
3.6.1 Original Leishman-Beddoes . . . 55
3.6.2 Comparison . . . 55

4 3D unsteady attached flow 61
4.1 Closed form solutions . . . 61
4.2 Method . . . 62
4.2.1 Lifting line theory . . . 63
4.2.2 Unsteady Kutta-Jukowsky . . . 64
4.2.3 Wagner's sectional circulatory lift . . . 64
4.2.4 Added mass effect . . . 67
4.2.5 Assembling the pieces together . . . 67
4.2.6 Asymptotic behavior for a rectangular wing ($c = c_0$) . . . 68
4.3 Wagner lifting line aeroelastic matrix computation . . . 69
4.3.1 Sectional normal lift . . . 69
4.3.2 Downwash . . . 70
4.3.3 Wagner lifting line . . . 70
4.3.4 Trapezoidal rule . . . 71
4.3.5 Non-circulatory loads . . . 71
4.3.6 Total aerodynamic loads . . . 72
4.3.7 Structural equations . . . 72
4.3.8 Aeroelastic system matrix . . . 72

5 3D model comparisons 73
5.1 Test cases . . . 73
5.1.1 Types of motion . . . 74
5.1.2 Validation . . . 74
5.2 Convergence . . . 75
5.2.1 Runge-Kutta convergence . . . 75
5.2.2 Vortex lattice convergence . . . 76
5.3 Lift and moment results for rectangular wing . . . 77
5.4 Lift and moment results for tapered wing . . . 78
5.5 Computational cost . . . 80
5.6 Aeroelastic test case . . . 81
5.6.1 Aeroelastic equations of motion . . . 82
5.6.2 Results . . . 83

5.7 Conclusions 83

6 Conclusion **85**
6.1 Summary of contribution 85
6.2 Suggestion for further work 86

A Publication from this thesis **87**

B Full models comparison **89**

Bibliography **105**

List of Figures

1.1 Sketch of the three different stall types taken from Bak et al. [12] . . . 2
1.2 Flow sketches of thin airfoil stall mechanisms . . . 3
1.3 Flow sketches of leading edge stall mechanisms . . . 4
1.4 Flow sketches of Trailing edge stall mechanisms . . . 5
1.5 Stall mechanisms of 2D airfoils as a function of Reynolds number and the upper surface ordinate of the airfoil sections at 0.0125 chord (based on data from Gault [9]) . . . 6
1.6 Evolution of normal lift with unsteady angle of attack for a thick airfoil (S809 airfoil taken from NREL data [23]) . . . 7
1.7 Evolution of normal lift with unsteady angle of attack for a thin airfoil (N0012 data taken from chapter 3) . . . 8
1.8 Flow sketches of dynamic stall mechanisms . . . 9
1.9 Finite wing schematic (reproduced from Anderson [40]) . . . 10
1.10 Effect of downwash on a typical airfoil section of a finite wing (Reproduced from Anderson [40]) . . . 11
1.11 Schematic of the superposition of horseshoe vortices for Prandtl lifting line theory. (Reproduced from Anderson [40]) . . . 11
1.12 Surface oil flow pattern on a stalled, finite rectangular wing with a Clark Y-14 airfoil section. $AR = 3.5$, $\alpha = 22.8°$, $Re = 245,000$ (based on chord length). (Taken from Anderson [40]) . . . 13
1.13 Visualization of two stall cells formed over the S826 airfoil at $Re = 160000$ and $\alpha = 12°$ (Taken from Sarlak et al. [45]) . . . 13
1.14 Leading edge vortex or omega vortex on unsteady finite wing . . . 14

2.1 Critical normal force separation onset boundary for the NACA0012 airfoil. . . . 21
2.2 Flow separation scheme for a flat plate . . . 22
2.3 Leishman-Beddoes fitting of the separation point for the normal force . 23
2.4 Leishman-Beddoes fitting of the separation point for the pitching moment 23
2.5 Modified Leishman Beddoes overview . . . 27
2.6 Rigid thin plate airfoil scheme . . . 29
2.7 Curve fitting function s(α) for the NACA0012 wing using cubic splines 33
2.8 Position of the point of application of the normal force under separated flow conditions. . . . 33
2.9 Curve fitting function $g(\alpha)$ for the NACA0012 wing using cubic splines 34
2.10 Curve fitting function $s(\alpha)$ and $g(\alpha)$ for the NACA0012 wing showing the cubic splines nodes . . . 35
2.11 Aerodynamic loads for a NACA0012 oscillating with amplitude $A = 10°$, frequency $f = 5$ Hz and mean angle $A_0 = 10°$ and Reynolds number $Re \simeq 1.8 \times 10^4$. . . . 37
2.12 Comparison between equivalent reduced pitch rate and reduced pitch rate with angle of dynamic stall onset for a NACA0012 . . . 38

2.13 Comparison of two curve fitting methods for the dynamic stall onset angle applied to NACA0012 at high and low Reynolds. 38
2.14 Two methods used to compute time lag T_a for a NACA0012 at Reynolds $\simeq 1.8 \times 10^4$ 39
2.15 Determination of the time taken by the vortex to travel over the airfoil t_{vl}, for a NACA0012 airfoil and Reynolds number $Re \simeq 1.8 \times 10^4$. . . . 41
2.16 Variation of T_{vl} with r for the two NACA wings (left), $1/T_{vl}$ vs r for the NACA 0012 (right). 41

3.1 Side view of the tested wings. 46
3.2 NACA0012 in mounted configuration inside the wind tunnel. 47
3.3 Summary of the unsteady measurement process for a NACA0012 airfoil with a pitching motion of amplitude 15°, frequency $f = 2.5$ Hz, wind velocity $U = 7.25$ m/s and reduced frequency $k = 0.043$. 49
3.4 Normal force c_n and pitching moment c_m coefficient variation with angle of attack from static tests 51
3.5 Dynamic stall onset angle variation with instantaneous reduced pitch rate for the NACA 0012 and 0018 airfoils. 52
3.6 Static and dynamic stall criterion for the flat plate. 53
3.7 Stall angle variation with instantaneous reduced pitch rate for the flat plate. 53
3.8 Variation of T_{vl} with r for the two NACA wings. 54
3.9 Comparison between model and experiment for the flat plate. 57
3.10 Comparison between model and experiment for the NACA0012. 58
3.11 Comparison between model and experiment for the NACA0018. 59

4.1 Rigid thin plate airfoil scheme 65
4.2 Representation of m strips along the wing span and their respective local variables 68

5.1 Rectangular wing with pitch axis at the leading edge and quarter chord. 73
5.2 Tapered wing with pitch axis at the leading edge and quarter chord. . 74
5.3 WLL convergence with tolerance parameter and number of spanwise strips for a rectangular wing 75
5.4 VLM convergence with number of chordwise panels. 76
5.5 Comparison between VLM, WLL and strip theory for a rectangular wing undergoing a step motion 77
5.6 Lift comparison between VLM, WLL and strip theory for a rectangular wing undergoing an oscillation motion. 78
5.7 Moment comparison between VLM, WLL and strip theory for a rectangular wing undergoing an oscillation motion. 79
5.8 NRMSD between VLM and WLL aerodynamics responses for a rectangular wing $AR = 6$ undergoing oscillations motion. 79
5.9 Comparison between VLM, WLL and strip theory for a tapered wing, $AR = 6$, undergoing a step motion 80
5.10 NRMSD between VLM and WLL aerodynamic responses for a tapered wing $AR = 6$ undergoing oscillations motion 81
5.11 Comparison of flutter with aeroelastic axis for 3D wing, computed with vortex lattices (dashed line) and Wagner lifting line (solid) 84

B.1 Comparison between the modified LB model and experimental results for the flat plate with $f = 1$ Hz. 90

B.2 Comparison between the modified LB model and experimental results for the flat plate with $f = 2.5$ Hz. 91
B.3 Comparison between the modified LB model and experimental results for the flat plate with $f = 5$ Hz. 92
B.4 Comparison between the modified LB model and experimental results for the flat plate with $f = 7.5$ Hz. 93
B.5 Comparison between the modified LB model and experimental results for the flat plate with $f = 10$ Hz. 94
B.6 Comparison between the modified LB model and experimental results for the NACA0012 with $f = 1$ Hz. 95
B.7 Comparison between the modified LB model and experimental results for the NACA0012 with $f = 2.5$ Hz. 96
B.8 Comparison between the modified LB model and experimental results for the NACA0012 with $f = 5$ Hz. 97
B.9 Comparison between the modified LB model and experimental results for the NACA0012 with $f = 7.5$ Hz. 98
B.10 Comparison between the modified LB model and experimental results for the NACA0012 with $f = 10$ Hz. 99
B.11 Comparison between the modified LB model and experimental results for the NACA0018 with $f = 1$ Hz.. 100
B.12 Comparison between the modified LB model and experimental results for the NACA0018 with $f = 2.5$ Hz. 101
B.13 Comparison between the modified LB model and experimental results for the NACA0018 with $f = 5$ Hz. 102
B.14 Comparison between the modified LB model and experimental results for the NACA0018 with $f = 7.5$ Hz. 103
B.15 Comparison between the modified LB model and experimental results for the NACA0018 with $f = 10$ Hz. 104

List of Tables

2.1 Leishman-Beddoes indicial functions parameters 18
2.2 Variation of the trailing edge separation lag parameters T_f during the vortex shedding phase. 25
2.3 Variation of the vortex dissipation time parameters T_v during the vortex shedding phase. 25

3.1 Wings dimensions and Reynolds numbers 46
3.2 Equivalent reduced pitch rate for the flat plate as a function of the frequency and amplitude of motion. 50
3.3 Equivalent reduced pitch rate for the NACA 0012 and 0018 as a function of the frequency and amplitude of motion. 52
3.4 Curve fit coefficients of the dynamic stall onset angle for each airfoils . 53
3.5 Vortex passage time curve fit coefficients for each airfoil 54
3.6 Original Leishman-Beddoes parameters for each airfoil 55

5.1 Computation time comparison between VLM and WLL 81

List of Abbreviations

AR	**A**spect **R**atio
CFD	**C**omputational **F**luid **D**ynamic
DLM	**D**oublet **L**attice **M**ethod
LB	**L**eishman-**B**eddoes
LE	**L**eading **E**dge
LEV	**L**eading **E**dge **V**ortex
NACA	**N**ational **A**dvisory **C**ommittee for **A**eronautics
NREL	**N**ational **R**enewable **E**nergy **L**aboratory
NRMSD	**N**ormalized **R**oot **M**ean **S**quare **D**eviation
ONERA	**O**ffice **N**ational d'**E**tudes et de **R**echerches **A**érospatiales
PID	**P**roportional **I**ntegral **D**erivative
RMSD	**R**oot **M**ean **S**quare **D**eviation
TE	**T**railing **E**dge
VLM	**V**ortex **L**attice **M**ethod
WLL	**W**agner **L**ifting **L**ine

List of Symbols

a_0	Wing root lift curve slope
$a, b, c_{T_{vl}}$	Coefficients used to fit $1/T_{vl}(\alpha)$ with a second order equation
a, b, c_{ds}	Coefficients used to fit $\alpha_{ds}(\alpha)$ with a second order equation
A	Angle of attack amplitude of experiments
A_0	Mean angle of attack of experiments
AR	Aspect ratio
α	Geometric angle of attack
α_0	Zero lift angle of attack
α_{ds}	Dynamic stall angle onset
$\alpha_e = \frac{\omega}{U}$	Wagner equivalent angle of attack
α_{eff}	Local effective angle of attack from 3D flow effects
α_i	Induced angle of attack
α_s	Delayed effective angle of attack
b	Half-chord
$\beta = \sqrt{1 - M^2}$	Compressibility factor
β_1	Normal force vortex induced overshoot parameter
β_2	Moment vortex induced overshoot parameter
c	Chord
c_0	Wing root chord
c_l	2D lift coefficient
c_l^c	Attached circulatory lift coefficient
c_m	Moment coefficient
c_{m0}	Zero lift moment coefficient
$c_{m_{1/4}}$	Measured moment at quarter chord
$c^0_{m_{1/4}}$	Measured zero lift moment at quarter chord
c_m^c	2D circulatory moment coefficient
c_m^f	detached moment coefficient
c_m^I	2D non-circulatory moment coefficient
c_m^v	Vorticity induced moment coefficient
c_n	Normal lift coefficient
c_{n1}	Vortex onset criterion based on normal lift coefficient
c_n^c	2D circulatory normal force coefficient
c_n^f	detached normal force coefficient
c_n^I	2D non-circulatory normal force coefficient
c_n^v	Vorticity induced normal force coefficient
c_v	Difference between attached and detached lift coefficients for a given α
CP_v	Center of pressure motion due to Vortex shedding
Δc_n^v	Vortex induced Normal force coefficient overshoot
Δc_m^v	Vortex induced Moment coefficient overshoot
f	Frequency
f_α	Pitch natural frequency
f_h	Plunge natural frequency

g	Center of pressure position from quarter chord
g_s	Set of cubic splines function used to fit g
Γ	Circulation
h	Plunge
I_w	Wing moment of inertia around the pitching axis
$k = \frac{2\pi f b}{U}$	reduced frequency
k_h	Plunge stiffness
k_α	Pitch stiffness
$K_{0,1,2}$	Original LB parameters used to represent $g(s)$
l	2D lift
m_w	Wing mass
M	Mach
$r = \frac{\dot{\alpha} u}{b}$	Reduced pitch rate
Re	Reynolds number
ρ_∞	Free stream density
s	Separation point
s_s	Set of cubic splines function used to fit s
$S_{1,2}\,, \alpha_1^0$	Original LB parameters used to represent $s(\alpha)$
S_w	Wing static imbalance around the pitching axis
t_v	Time parameter used to track the position of the leading edge vortex
t_{vl}	Time needed by the leading edge vortex to reach the trailing edge
T_a	Unsteady boundary layer delay time constant
T_p	Pressure delay time constant
T_v	Circulation dissipation time constant
T_{vl}	Non-dimensional time needed by the LEV to reach the trailing edge
U	Airspeed
V_∞	Free stream velocity
V_x	Vortex induced overshoot shape function
$\omega(y)$	Downwash on position y along the wing span
x_{ac}	Position of the aerodynamic center from leading edge
x_e	The distance between the pitch axis and the half-chord

Chapter 1

Introduction

1.1 2D Dynamic stall

Dynamic stall is described by Mac Croskey et al. [1], [2] as a phenomenon that occurs on airfoils subjected to any kind of unsteady motion. The phenomenon occurs at higher angles of attack and lift values than steady stall. Dynamic stall can also be associated with the shedding of a vortex from the leading edge. This vortex usually affects the flow around the airfoil such that it increases further the instantaneous lift acting on the wing and produces a nose down pitching moment when the vortex travels over the rear of the airfoil. The modeling of dynamic stall is challenging because it involves detached and turbulent flow. Typical approaches range from semi-empirical, such as the Leishman-Beddoes (LB) [3] or the ONERA models, [4], [5] to Computational Fluid Dynamic (CFD) methods.

1.1.1 Static stall

The phenomenon known as stall was first defined in the case of steady measurements of the aerodynamic lift acting on an airfoil. It was first extensively studied as a function of Reynolds, flow turbulence and boundary layer by Eastman [6] as well as Millikan and Klein [7] A sketch of different lift curves as a function of the angle of attack is shown on figure 1.1. All three curves are linear at low angles of attack but become non linear at higher angles. The phenomenon known as stall is the passage from linear to non linear behavior of a lift curve. The different types of stall are : trailing edge, leading edge and thin airfoil, as described by McCulough and Gault [8], [9], McCormick [10] and detailed by Broeren [11]. Thin airfoil and trailing edge stall are described as 'soft' because the lift curve slope decreases slowly. Leading edge stall is described as 'hard' because there is a sudden loss of lift with the increase of the angle of attack.

The changes in the lift curve slope with respect of the angle of attacks reflect modifications of the flow around the airfoil. When the relation is linear, the flow is fully attached to the airfoil. At stall however, the flow field starts to detach from the surface of the airfoil, which increases the pressure on the suction side and decreases the lift generated by the airfoil, with respect to the lift that would have been generated if the flow had remained attached.

Figure 1.2 represents the thin airfoil stall mechanism. At the low angle of attack of Figure 1.2(a) the flow is fully attached on the airfoil and the relation between the angle of attack and the lift is linear. In the case of the moderate angle of attack shown in Figure 1.2(b), the flow starts to detach from the sharp leading edge and reattach quickly on the airfoil. This small region of detached flow is known as a separation bubble and increases the pressure on the suction side. As shown in Figure 1.2(c), the

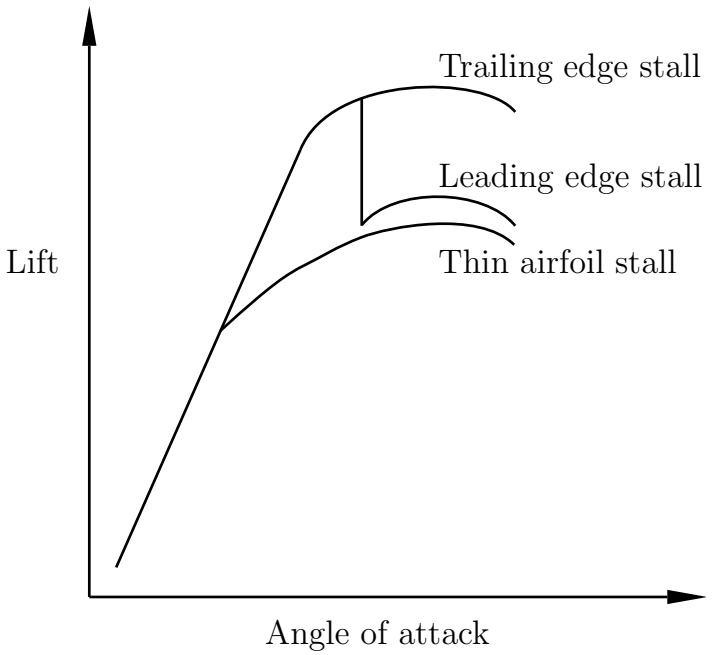

FIGURE 1.1: Sketch of the three different stall types taken from Bak et al. [12]

size of the separation bubble increases with the angle of attack. Finally, the bubble covers the whole airfoil and the flow becomes fully detached.

According to McCormick [10], thin airfoil stall occurs at low angles of attack inducing a lower maximum lift coefficient. One way to improve airfoil performance is to round the leading edge and increase the thickness of the airfoil, so that the flow can more easily follow the contour of the leading edge. As a result, there is an increase in the maximum lift coefficient and a modification of the stall mechanism in the form of either leading edge or trailing edge stall.

The leading edge stall mechanism is shown in Figure 1.3. At low angles of attack the flow is fully attached as seen in Figure 1.3(a) and the lift curve relation is again linear. For moderate angles of attack the flow is still mostly attached to the airfoil but there is the formation of a small separation bubble near the leading edge, as seen on Figure 1.3(b). As the angle of attack increases, the bubble will burst suddenly and disrupt the flow field over the entire airfoil and so the flow over the upper surface is separated, as shown in Figure 1.3(c).

Leading edge stall leads to a better aerodynamic behavior compared to thin airfoil stall as the maximum lift coefficient is usually higher. However, it leads to a very dangerous type of stall as the lift will drop suddenly at stall, which can result in the destruction of the aircraft.

The trailing edge stall mechanism is shown in Figure 1.4. Once again, the relation between the lift and the angle is linear at low angle of attack and the flow is fully attached, as seen in Figure 1.4(a). Once the angle of attack increases, one can see flow separation starting at the trailing edge of the airfoil in Figure 1.4(b) and moving towards the leading edge in Figure 1.4(c).

This can be seen as the best stall mechanisms because it leads to higher lift than thin airfoil stall and the stall occurence is relatively smooth. However, the airfoils with

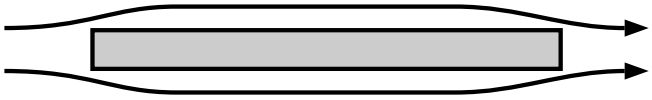

(a) Low angle of attack

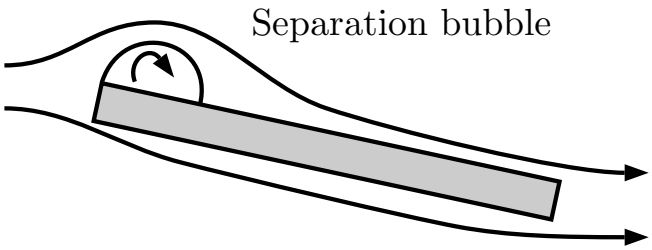

(b) Medium angle of attack

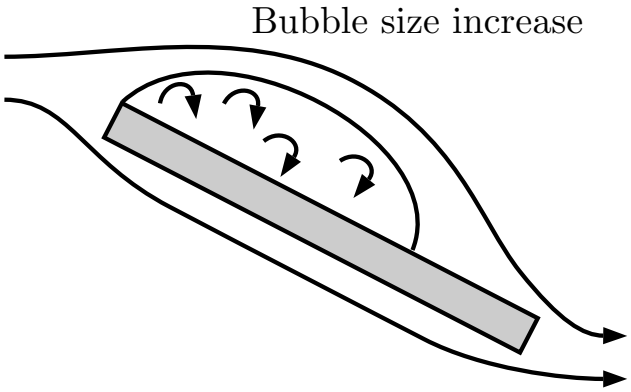

(c) High angle of attack

FIGURE 1.2: Flow sketches of thin airfoil stall mechanisms

this kind of stall mechanisms are usually heavier and create a higher drag because they are thicker.

Each steady stall mechanism has been studied separately but the extensive study by Broeren [11] showed that a trailing edge stall can occur simultaneously with leading edge or thin airfoil stall. This is possible because trailing edge stall occurs at the trailing edge while the two other stall types are located at the leading edge. It should also be noted that the abrupt nature of leading edge stall can hide the occurence of slower trailing edge stall, as illustrated in Figure 1.1 where the sudden drop of lift differentiate leading and trailing edge stall.

The stall mechanism is a function of airfoil thickness but also of the Reynolds number. Gault [9] carried out an extensive analysis of airfoil stall for different Reynolds numbers and airfoil thicknesses, as shown reported in Figure 1.5. The figure shows the different regions of stall mechanisms in the plane of Reynolds number and thickness of

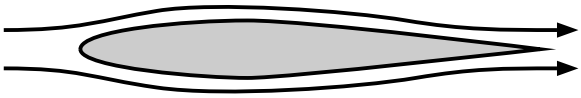

(a) Low angle of attack

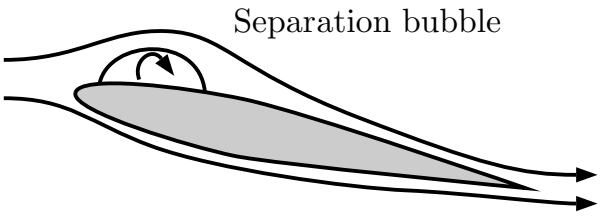

(b) Medium angle of attack

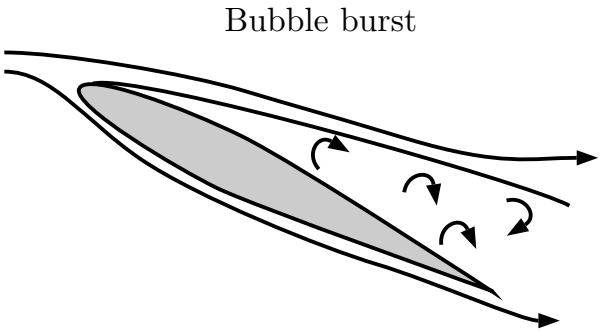

(c) High angle of attack

FIGURE 1.3: Flow sketches of leading edge stall mechanisms

the airfoil sections used. It clearly shows that the type of stall is also a function of the Reynolds number. The results obtained by Gault seem to indicate that with Reynolds numbers below $Re \simeq 3 \times 10^5$ the leading edge stall mechanism disappear leaving only the thin airfoil and trailing edge mechanisms. However, Broeren [11] found all three types of stall mechanism, as well as combined leading and trailling edge stall, for a Reynolds number of $Re = 3 \times 10^5$. These discrepancies between the two results could be explained by the fact that Gault only studied NACA airfoils while Broeren used other types of airfoil profile. Furthermore, Gault had fewer data points to separate the different stall mechanism regions for low Reynolds numbers.

1.1.2 Dynamic stall

Following the definition of MacCroskey et. al. [1], [2], [13], dynamic stall occurs on airfoils subjected to any unsteady motion and involves, flow separations, a stall delay, a complex reattachment process and, in some cases, a Leading Edge Vortex (LEV), which is shed near the leading edge and travels downstream.

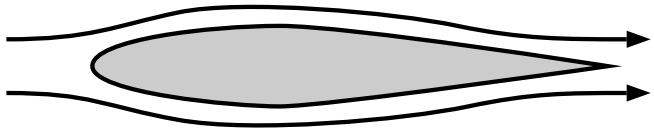

(a) Low angle of attack

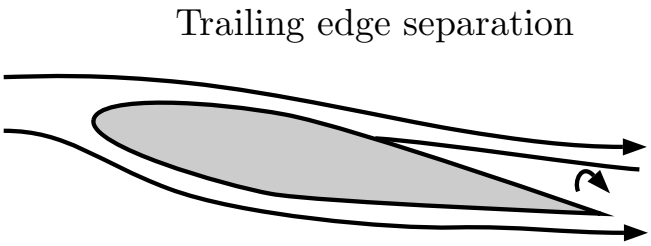

(b) Medium angle of attack

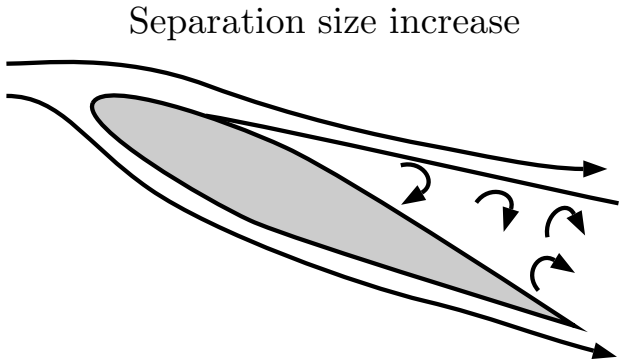

(c) High angle of attack

FIGURE 1.4: Flow sketches of Trailing edge stall mechanisms

The first thorough analysis of dynamic stall was performed by Halfman et. al.[14] who discussed their own experimental results and those of their contemporaries. Ericsson and Reding [15]–[17] carried out a lot of early work on stall delay phenomena associated with dynamic stall. Ham [18] showed later on that the position of the separation point at the trailing edge was not constant. The trailing edge separation effect on dynamic stall was further explored by MacCroskey et. al. [2] and Carr et. al. [19]. Ham and Young [20] described the spilling of a vortex which increased the lift generated by the airfoil. The onset of this leading edge vortex was studied by Currier and Fung [21]. The flow reattachment process was more recently studied by Green and Galbraith [22] for the case of constant pitch rate ramp-down motions.

The underlying physical process is similar to static stall but does not occur at the same instantaneous angle of attack. One of the important differences between static and dynamic stall is that the instantaneous aerodynamic load measurements are not

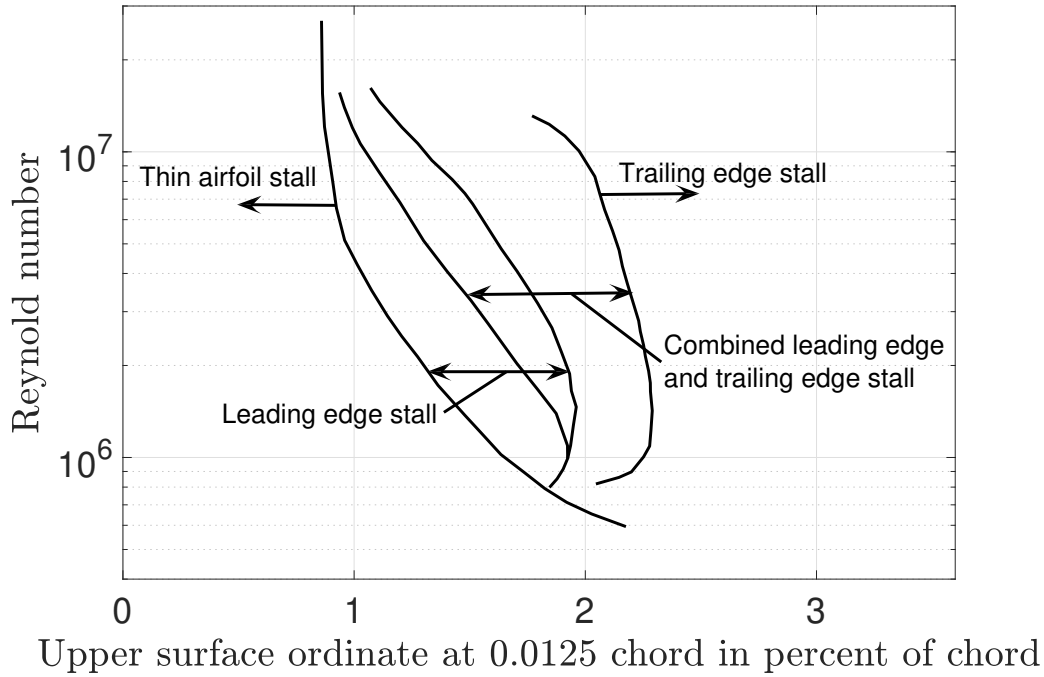

FIGURE 1.5: Stall mechanisms of 2D airfoils as a function of Reynolds number and the upper surface ordinate of the airfoil sections at 0.0125 chord (based on data from Gault [9])

averaged in time for the latter. Phenomena such as the bursting of the separation bubble from figure 1.3 are on only inferred from the before and after state of the steady flow for static stall while observed directly for dynamic stall.

Dynamic stall can occur when unsteady effective angles of attack are involved. This can include: moving helicopters and the change of angle of attack between the advancing and retreating blades [13]; wind turbines [24], [25] with wind gusts, tower shadow and yaw misalignment; flapping wings; gust or unsteady wind changes affecting otherwise steady airfoils. Dynamic stall, even if it is associated with greater lift generation, is usually not welcome in aerodynamic design. The increase in lift only occurs during part of the motion, while the lift is lower during the rest of the motion. Furthermore, a significant increase in drag is associated with the phenomenon. In some cases, dynamic stall is characterized by the formation of a vortex that is shed over the airfoil. This vortex disturbs the flow and creates a nose-down pitching moment, which increases the torque loads on the apparatus which and could result in fatigue of the material. Dynamic stall is also associated with an aeroelastic instability known as stall flutter which causes limit cycle oscillations resulting in an even worse risk of fatigue.

Looking at Figure 1.6, plotting the normal force curve against angle of attack for a S809 airfoil under steady and unsteady conditions, and the associated flow snapshots of figure 1.8, one can describe the dynamic stall mechanism:

Unsteady attached flow 1.8(a) : The motion of the airfoil creates trailing edge vortices which have an effect on the flow field around the airfoil. These reduce the effective angle of attack seen by the airfoil and add an effective camber, both of which delay the apparition of stall.

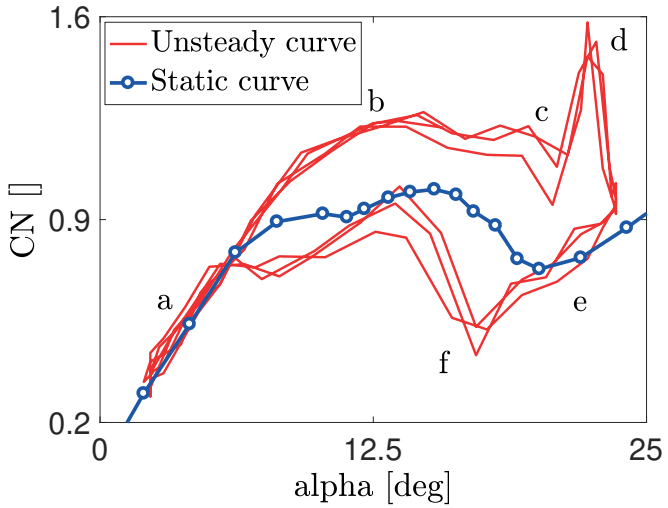

FIGURE 1.6: Evolution of normal lift with unsteady angle of attack for a thick airfoil (S809 airfoil taken from NREL data [23])

Unsteady detached flow 1.8(b) : For thick airfoils, a delayed trailing edge separation will occur similarly to steady trailing edge stall 1.4. The delay is also caused by the various unsteady effects.

Vortex onset 1.8(c) : At some point, a separation bubble will form at the leading edge, akin to the steady leading edge stall 1.3. However, the effects of the bubble burst will only be visible while the resulting leading edge vortex travels toward the trailing edge. This vortex will further decrease the pressure on the airfoil's suction side, increasing the generated lift. The flow field around the airfoil is also disturbed by the vortex, so that the center of pressure moves towards the mid-chords which induces a nose-down pitching moment.

Vortex leaves airfoil 1.8(d) : When the leading edge vortex reaches the trailing edge, its effects quickly vanish.

Full separation 1.8(e) : The flow was heavily disrupted by the vortex and is now fully separated.

Reattachment 1.8(f) : Once the angle of attack starts to decrease, the flow will slowly start to reattaches.

The description of dynamic stall presented in figures 1.6 and 1.8 shows mechanism very similar to the combination of trailing and leading edge static stall detailed in section 1.1.1. The main differences lie in effective angle of attack being different from the steady one and the non average of unsteady effects such as the vortex onset.

As the bubble burst from static stall and the leading edge vortex from dynamic stall are linked, it is expected that the vortex onset angle, that is the angle of attack at which the leading edge vortex starts to shed, is higher for thicker airfoil. This can be seen for the S809 airfoil on figure 1.6, the vortex shedding occurs at a very high angle of attack (point (c) on figure 1.6) and the dynamic trailing edge separation is easy to locate (point (b) on figure 1.6). For thinner airfoil, it is expected that the vortex shedding starts at lower angle and can hide the trailing edge separation effects. This can be seen on figure 1.7 representing the dynamic stall loop for a NACA0012

airfoil. Here, the vortex onset is more difficult to locate as it begins before any real trailing edge separation as seen on figure 1.6. The only effect visible is an increase in the slope of the curve starting around (point a) on figure 1.7. Similarly to static stall, one can expect that for some airfoil there is no vortex formation during dynamic stall. The vortex either never form, never detach or is too weak to be really noticed. In these cases, steps 1.8(c) and 1.8(d) for the dynamic stall are ignored and the flow is fully detached in step 1.8(e) thanks to the trailing edge separation mechanism.

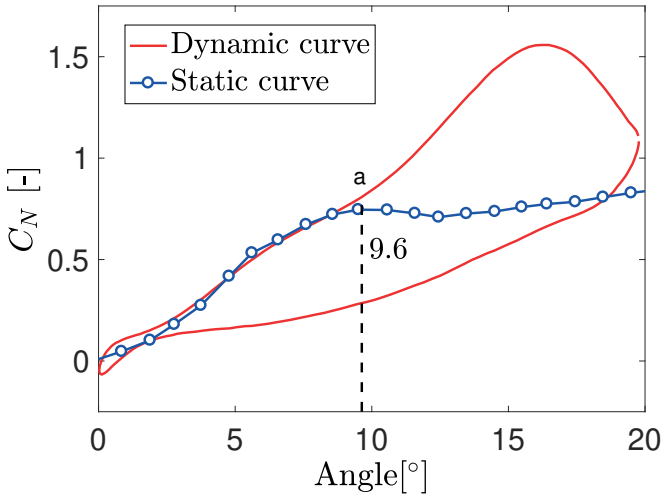

FIGURE 1.7: Evolution of normal lift with unsteady angle of attack for a thin airfoil (N0012 data taken from chapter 3)

1.2 Models

The model by Gormont[26] arising from earlier work by Harris et. all. [27], and Tarzanin [28], was developed in the 1970s and is one of the first to use semi experimental results to compute the aerodynamic loads in dynamic stall conditions. The model starts by the flow around an oscillating airfoil using Theodorsen theory. However, this only allows to represent the unsteady aerodynamic loads before stall. Stall can be included by incorporating the change in the slopes of the lift and moment curves of static airfoils. Finally, the effect of stall delay can be added by defining a delayed angle of attack. This angle evolution is determined experimentally from wind tunnel experiments on oscillating airfoils..

The model by Gangwani and Bielawa [29]–[31] proposed in the 1980s focused more on the physics of dynamic stall. Their model defined three important angles : the dynamic stall onset angle, the angle at which the LEV reaches the trailing edge of the airfoil, and the reattachment angle. Gangwani and Bielawa defined relationships able to predict the three angles for specific airfoils, Mach, and Reynold numbers. Then, the effects of dynamic motion on the value of these parameters is evaluated using a combination of the instantaneous angle of attack, the reduced pitch rate $r = \dot{\alpha}\frac{b}{U}$, and the equivalent angle of attack defined by Wagner.

So far, the dynamic stall modelling was always based on the different flow mechanisms involved in the phenomenon. The Onera [4], [5] model took a different approach however. It directly uses a set of differential equations to separately compute the lift and the moments. In the base model, there are 22 coefficients that are functions of

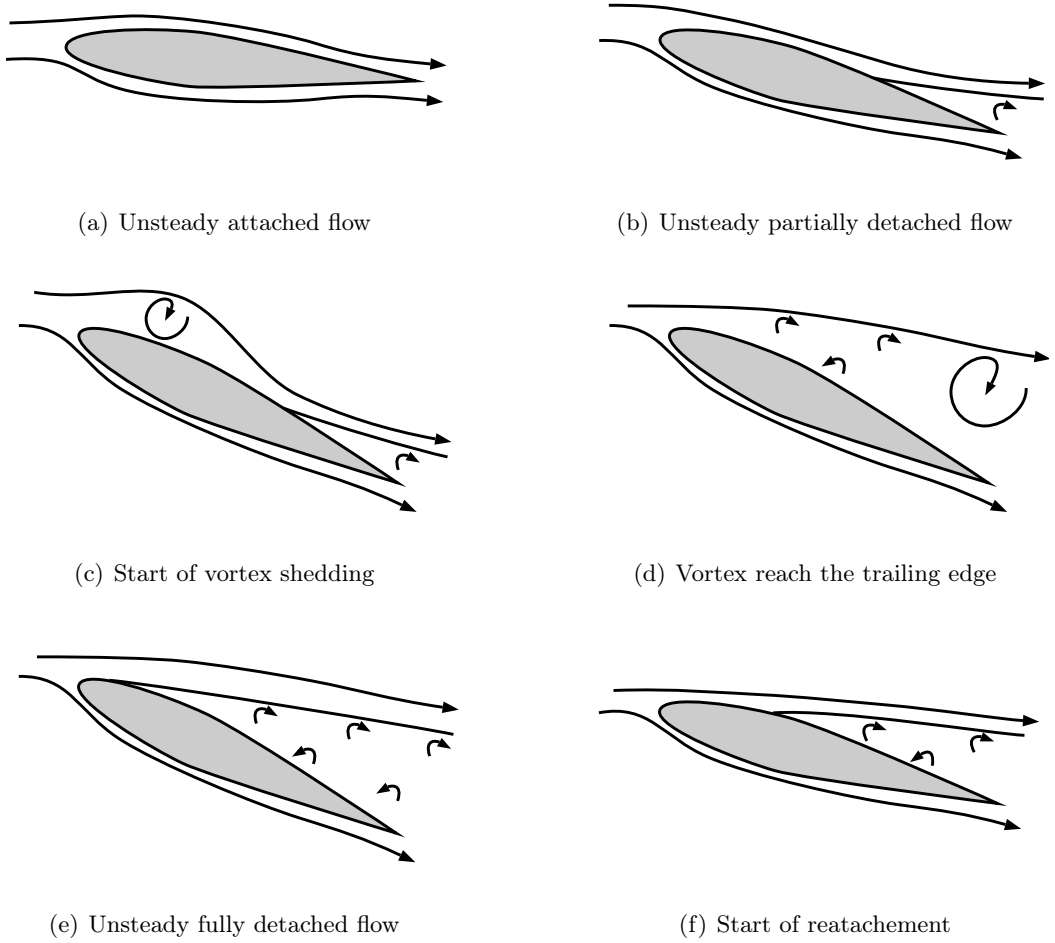

(a) Unsteady attached flow

(b) Unsteady partially detached flow

(c) Start of vortex shedding

(d) Vortex reach the trailing edge

(e) Unsteady fully detached flow

(f) Start of reatachement

FIGURE 1.8: Flow sketches of dynamic stall mechanisms

the angle of attack, the airfoil profile, and the Mach number. As they represent time derivatives, they have to be experimentally determined from a set of small amplitude oscillations for different reduced frequencies and mean angles of attack

The Leishman-Beddoes [3] model was developed towards the end of 1980s aim to compute the aerodynamic loads of airfoils undergoing stall. Its emphasis was put on a complete physical representation of dynamic stall while keeping the complexity as low as possible. The model is composed of three modules aiming to represent different physical phenomena, an attached flow module to represent the unsteady attached flow, a detached flow module using Kirchhoff-Helmholtz theory to link the separated lift to the position of the separation point and, a dynamic stall module to take into account the effects of the leading edge vortex on the airloads.

The Leishman-Beddoes model is often adapted and modified for different applications. Riso [32] simplified the model for wind turbine application, they removed compressibility and leading edge separations effects since these do not usually occurs on thicker windturbine airfoil. Sheng and Galbraith [33]–[36] on the other hand aimed to change the leading edge separations onset criterion for low Mach numbers.

Examples of CFD solutions for 2-D and 3-D dynamic stall can be found in Srinivasan et. al. [37], Ekaterinaris et. al. [38] or Spentzos et. al. [39] works. The disadvantage of such approaches is that they are very computationally expensive and

are therefore unsuitable for design purposes. Empirical models are much faster but they must be well calibrated for each individual airfoil, Mach number and Reynolds number.

1.3 3D dynamic stall

1.3.1 3D lift distribution

When a finite wing is considered, the flow inevitably has a third dimensional component along the span of the wing. Indeed, as the wing is generating lift, there is a difference of pressure between the top side and down side. At the wingtip, this difference of pressure will create a sideway airflow going from the high to low pressure side as can be seen in figure 1.9(a). As the wing moves, these transversal flow at the

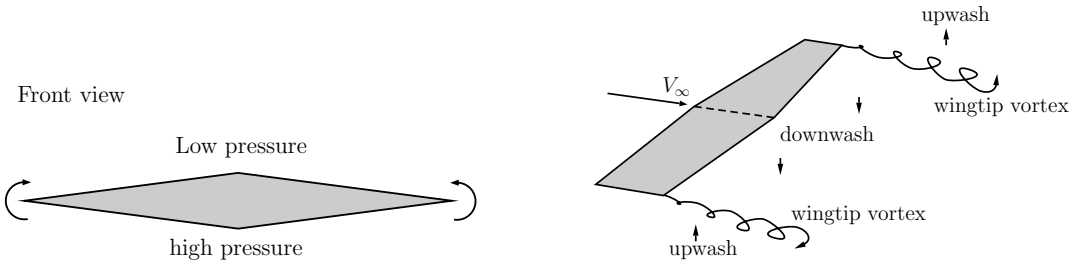

(a) Wing tip flow (b) Wing tip vortices

FIGURE 1.9: Finite wing schematic (reproduced from Anderson [40])

wingtip will generate the so called wingtip vortex downstream of the wing as shown on figure 1.9(b). The flow will be influenced by these vortices, creating a downwash between the wingtips and an upwash outside. This downwash affects the wing and reduces the effective angle of attack seen by each of its airfoil section because the geometric angle of attack α is reduced by an induced angle of attack α_i

$$\alpha_{eff} = \alpha - \alpha_i \tag{1.1}$$

The downwash will also change the direction of application of the lift which lower the effective lift and create an induced drag as shown on figure 1.10. Furthermore, the effective lift and induce drag are not constant along the span of the wing because, usually, the downwash is stronger near the wingtips.

1.3.2 lifting line

The idea of Prandtl to compute the effect of the downwash on the wing started by considering a bound vortex of circulation Γ located on the wing. However, due to Helmholtz theorem, this bound vortex cannot end in the fluid, two free trailing vortices that extend toward infinity must be added at the wingtip. This vortices structure shown on figure 1.11(a) is called a horseshoe vortex.

Now, a representation of the wingtip vortices exists as two trailing edge vortices of circulation Γ, it is possible to simply compute the downwash generated by these vortices with the Bio Savart law. The expression of the downwash is then simply

$$w(y) = \frac{-\Gamma}{4\pi\left(s/2 + y\right)} - \frac{-\Gamma}{4\pi\left(s/2 - y\right)} \tag{1.2}$$

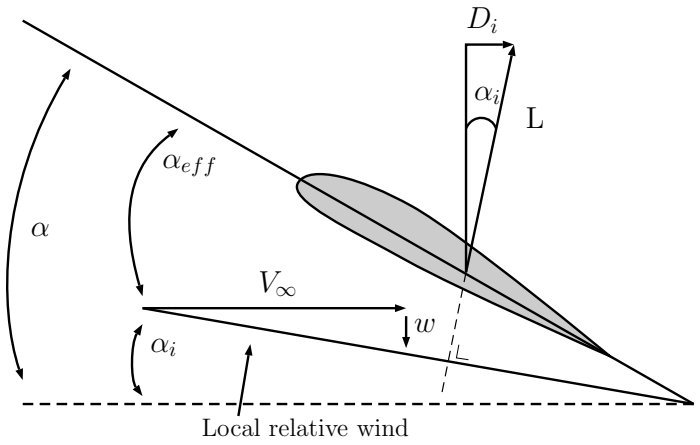

FIGURE 1.10: Effect of downwash on a typical airfoil section of a finite wing (Reproduced from Anderson [40])

with $w(y)$ the downwash on the airfoil section in location y and s the wing span. However, this equation does not represent realistically the downwash on a finite wing. Furthermore there are two singularities at the wingtips ($\mid y \mid = s/2$) where the downwash increases to infinity.

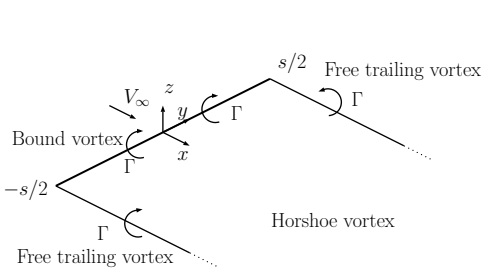

(a) Single horseshoe vortex

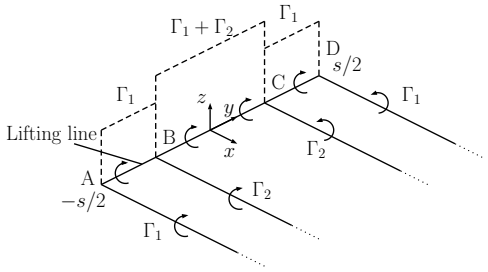

(b) Multiple horseshoe vortices

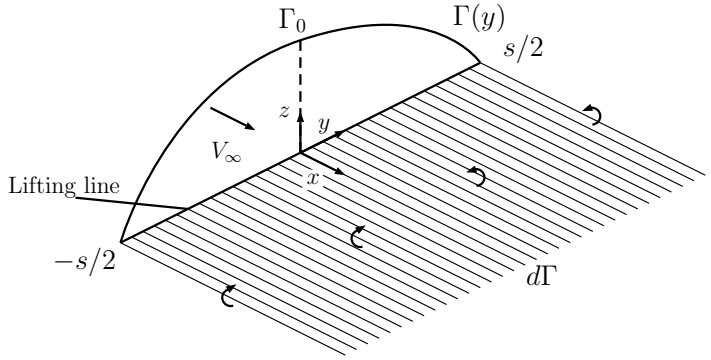

(c) Infinite number of horseshoe vortices

FIGURE 1.11: Schematic of the superposition of horseshoe vortices for Prandtl lifting line theory. (Reproduced from Anderson [40])

To solve these problem, Prandtl added multiple horseshoe vortices of different length along the span to represent the vorticity around the wing. One example is shown on figure 1.11(b) where there are two horseshoe vortices : the first one of

circulation Γ_1, extends on the entirety of the wingspan from point A to D and the second one with a circulation Γ_2 is smaller and extend from point B to C. As a result, the circulation on the wing between AB and CD are only affected by the first horseshoe vortex and is Γ_1. On the other hand, between BC, the circulation is changed by both horseshoe vortices and the circulation is $\Gamma_1 + \Gamma_2$. At the end of the day, this approach allows for a discreet variation of the vorticity along the wing span.

The next step consist to use an infinity of horseshoes vortex as shown on figure 1.11(c). This result in the continuous variation of the circulation on the wing and the presence of a vortex sheet trailing behind the wing. The downwash applied on the wing can then be computed with the integral

$$w(y) = -\frac{1}{4\pi}\int_{-s/2}^{s/2} \frac{d\Gamma/dy_0}{y - y_0}\, dy_0 \tag{1.3}$$

and the induced angle of attack, for small angle, is

$$\alpha_i(y) = -\frac{w(y)}{V_\infty} \tag{1.4}$$

Finally, it is possible to link the circulation $\Gamma(y)$ and the lift applied on the finite wing with the Kutta-Joukowski theorem at the location y_0.

$$l(y_0) = \rho_\infty V_\infty \Gamma_{y_0} \tag{1.5}$$

$$c_l(y_0) = \frac{2\Gamma(y_0)}{V_\infty c(y_0)} \tag{1.6}$$

with ρ_∞ the free stream density, V_∞ the free stream speed and $c_l(y_0)$ the lift coefficient at location y_0. We know that in the case of steady airfoil with attached flow, the lift is simply

$$c_l = a_0\,(\alpha_{eff} - \alpha_0) \tag{1.7}$$

where α_0 is the angle of attack of zero lift of the airfoil section. Substituting 1.6 and solving for α_{eff} one get,

$$\alpha_{eff} = \frac{2\Gamma(y_0)}{a_0 V_\infty c(y_0)} + \alpha_0 \tag{1.8}$$

Substituting equation 1.4 and 1.8 into 1.1, one get the fundamental equation of prandtl's lifting-line theory

$$\alpha(y_0) = \frac{2\Gamma(y_0)}{a_0 V_\infty c(y_0)} + \alpha_0 + \frac{1}{4\pi}\int_{-s/2}^{s/2} \frac{d\Gamma/dy_0}{y - y_0}\, dy_0 \tag{1.9}$$

Finally, to solve integral 1.9 and find the distribution of circulation $\Gamma(y)$ on the wing. The circulation is usually represented with a truncated Fourier series

$$\Gamma(y) = \frac{1}{2}\, a_0\, c_0\, U \sum_{n=1}^{m} A_n \sin(n\theta) \tag{1.10}$$

with a_0 the lift curve slope at the wing root, and c_0 the chord at the wing root.

1.3.3 Stall cells

To talk about 3D dynamic stall, one must first consider the behavior of separation over a finite wing. The equivalent of the 2D leading edge vortex will be ignored in

this section for simplicity and only trailing edge separation or already separated flow over the wing will be considered. One can expect that the downwash applied on the wing is preventing or retarding the occurence of flow separation. As the downwash is strongest near the wingtip, one would expect the flow to detach at the wing centerline and be attached at the wingtip. This stall cells has a so called mushroom shape as presented by Winkelmann [41], [42] and shown on figure 1.12.

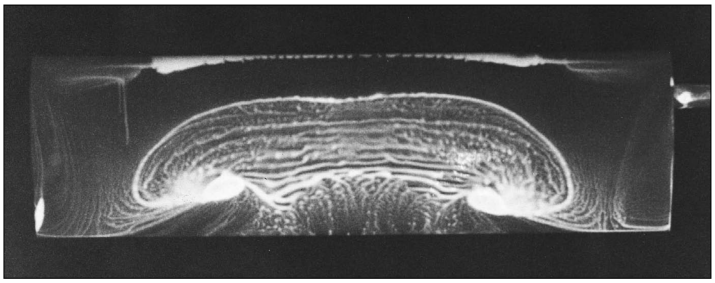

FIGURE 1.12: Surface oil flow pattern on a stalled, finite rectangular wing with a Clark Y-14 airfoil section. $AR = 3.5$, $\alpha = 22.8°$, $Re = 245,000$ (based on chord length). (Taken from Anderson [40])

However, stall cells are not that simple. As early as the 70s Gregory et al. [43], [44] observed the stalled patterns was not stable and multiple stall cells could form on a single wing. This can be seen on figure 1.13 from the experimental results of Sarlak et al. [45]. Yon and Katz [46] also showed that the stall cells were not always stationary and the whole flow structure can move along the wing span. Furthermore, the shape, numbers and apparition of stall cells are a function of the angle of attack, the aspect ratio and the Reynold number. Winkelmann and Barlow [47] and Schewe [48] showed that the number of stall cells increase with span for the same Reynold and angle of attack. Winkelmann and Barlow [47] also observed that increasing the angle of attack leads to smaller but wider stall cells. The location of the stall cells can be forced by locally disturbing the flow as shown by Marinos [49].

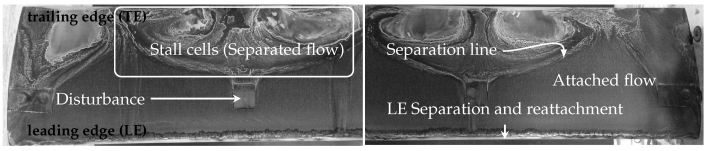

FIGURE 1.13: Visualization of two stall cells formed over the S826 airfoil at $Re = 160000$ and $\alpha = 12°$ (Taken from Sarlak et al. [45])

1.3.4 Omega vortex shedding

The next step to consider 3D dynamic stall is to look at the 3D leading edge vortex if there is any Freymuth [50] was the first to visualise the complex vortex structure occurring on unsteady wing which he dubbed a "omega vortex". This structure can be seen on figure 1.14(a). Further experiment performed by Pizziali [51], Shrek and Helin [52], Tang and Dowel [53], Werner et. al. [54] and, Coton and Galbraith [55] on 3D oscillating wing also showed this omega vortex structure for different Reynolds number, reduced frequency and aspect ratio.

At first, a leading edge vortex forms along the span of wing. This vortex interacts with the wing tip vortices which prevent it to freely moves away from the wing surface.

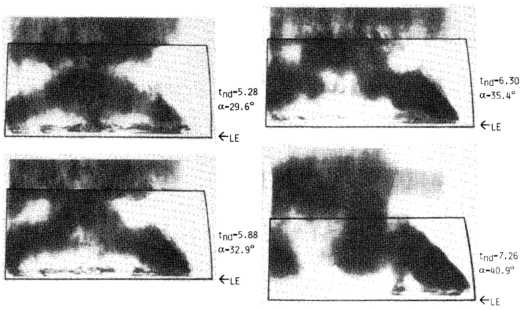

(a) Flow visualization taken from Shrek and Helin [52]

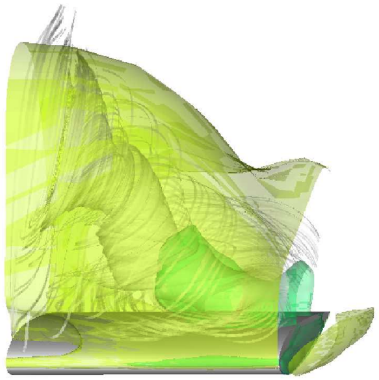

(b) CFD representation taken from Spentzos et. al.[56]

FIGURE 1.14: Leading edge vortex or omega vortex on unsteady finite wing

However, with increasing angle of attacks, the part of the leading edge vortex located at the wing root moves away from the wing while its edges stays connected to the wing tip vortices close to the wing. Once fully developed, the structure composed of the wing tip vortices and the partially separated leading edge vortex has an omega shape.

1.4 Objectives of this thesis

The ultimate aim of this thesis was to build a model able to compute the lift produced by a wing during 3D dynamic stall at low Reynolds numbers. From the available models to represent dynamic stall, it was decided to focus on the Leishman-Beddoes model.

This model wast not conceived with very low Reynolds numbers in mind. The first step is to create a modified Leishman-Beddoes model able to handle dynamic stall at these low Reynolds numbers. In order to extend this modified model to 3D, first a 3D unsteady attached flow model is developed in the present work.

1.5 Outline of this thesis

- Chapter two presents a modified Leishman-Beddoes model able to model dynamic stall at low Reynolds numbers. The classical LB model is presented first, which is built from three parts, the unsteady attached flow, the separated flow, and the dynamic stall. In the second part of this chapter, a low Reynolds modification of the LB model is presented.

- Chapter three implements both the LB and modified LB models and compares their respective predictions to data from a set of experiments. Three wing sections were chosen, a flat plate, a NACA0012, a NACA0018 because they are supposed to exhibit three distinct types of stall behaviour at intermediate Reynolds numbers [9].

- Chapter four presents an analytical unsteady 3D lift model that is required as a basis for a 3D dynamic stall model. This novel model is a combination of

2D Wagner theory and 3D Lifting Line theory and therefore is known as the Wagner Lifting Line model.

- Chapter five compares the result of the Wagner lifting line model with those of from a numerical Vortex Lattice simulation
- Chapter six presents the conclusions of the thesis and discusses avenues for further research.

Chapter 2

Leishman-Beddoes

This chapter starts by introducing the LB model which was selected to model dynamic stall in the present thesis. Then, a low Reynolds modification of the LB model is presented.

2.1 State space Leishman-Beddoes model

The popular Leishman-Beddoes dynamic stall empirical model was developed initially for helicopter rotor applications and tuned for Mach numbers higher than 0.3. It is designed to represent the unsteady lift and pitching moment of a two dimensional airfoil undergoing dynamic stall. Leishman and Beddoes built their model around different modules which represent the different physical phenomena associated with dynamic stall. They are :

- The computation of the unsteady attached flow, which is the foundation of the model.
- The computation of the vortex onset criterion and its effect on the aerodynamic loads.
- Kirchhoff-Helmholtz theory, which is used to represent trailing edge separation and link the attached and separated aerodynamic loads.

2.1.1 Attached flow

One popular method to compute the unsteady aerodynamic loads is the use of the Wagner indicial function. However, the Leishman-Beddoes model was initially built for compressible flow which cannot be directly represented using Wagner theroy. This is why Leishman and Crouse [57] developed their own indicials functions to compute the unsteady normal load and pitching moment acting on a 2D airfoil moving in compressible flow . These aerodynamic loads are computed for a step change in angle of attack $\Delta\alpha$ and pitch rate $\Delta q = \frac{\Delta\dot{\alpha}c}{V}$.

$$c_n^c = \frac{2\pi}{\beta}\phi_\alpha^C \Delta\alpha + \frac{\pi}{\beta}\phi_q^C \Delta q \tag{2.1}$$

$$c_m^c = \frac{2\pi}{\beta}\phi_\alpha^C \left(0.25 - x_{ac}(M)\right)\Delta\alpha - \frac{\pi}{8\beta}\phi_{qm}^c \Delta q \tag{2.2}$$

$$c_n^I = \frac{4}{M}\phi_\alpha^I \Delta\alpha + \frac{1}{M}\phi_q^I \Delta q \tag{2.3}$$

$$c_m^I = -\frac{1}{M}\phi_{\alpha m}^I \Delta\alpha - \frac{7}{12M}\phi_{qm}^I \Delta q \tag{2.4}$$

where c_n^c and c_m^c represent the indicial circulatory normal force and pitching moment coefficients, c_n^I and c_m^I represent the indicial non circulatory normal force and moment coefficients which are analogous to the apparent mass terms used for incompressible flow, β is the compressibility factor $\sqrt{1-M^2}$ and $x_{ac}(M)$ is the distance of the aerodynamic center from the leading edge.

The indicial functions ϕ_α^C , ϕ_q^C , ϕ_{qm}^C , ϕ_α^I , ϕ_q^I , $\phi_{\alpha m}^I$, ϕ_{qm}^I are respectively defined as

$$\phi_\alpha^C = 1 - A_1 \exp\left(-b_1\beta^2\frac{2V}{c}t\right) - A_2 \exp\left(-b_2\beta^2\frac{2V}{c}t\right) \tag{2.5}$$

$$\phi_q^C = \phi_\alpha^C \tag{2.6}$$

$$\phi_{qm}^C = 1 - \exp\left(-b_5\beta^2\frac{2V}{c}t\right) \tag{2.7}$$

$$\phi_\alpha^I = \exp\left(\frac{-t}{K_\alpha T_I}\right) \tag{2.8}$$

$$\phi_q^I = \exp\left(\frac{-t}{K_q T_I}\right) \tag{2.9}$$

$$\phi_{\alpha m}^I = A_3 \exp\left(\frac{-t}{b_3 K_{\alpha M} T_I}\right) + A_4 \exp\left(\frac{-t}{b_4 K_{\alpha M} T_I}\right) \tag{2.10}$$

$$\phi_{qm}^I = \exp\left(\frac{-t}{K_{qM} T_I}\right) \tag{2.11}$$

$$T_I = c/a \tag{2.12}$$

$$K_\alpha = \frac{1}{(1-M) + \pi\beta M^2(A_1 b_1 + A_2 b_2)} \tag{2.13}$$

$$K_q = \frac{0.75}{(1-M) + \pi\beta M^2(A_1 b_1 + A_2 b_2)} \tag{2.14}$$

$$K_{\alpha m} = \frac{A_3 b_4 + A_4 b_3}{b_3 b_4 (1-M)} \tag{2.15}$$

$$K_{qm} = \frac{7}{15(1-M) + 3\pi\beta M^2 b_5} \tag{2.16}$$

The numerical values of the different parameters, used in equations 2.5 to 2.16, are shown in table 2.1.

$A_1 = 0.3$	$b_1 = 0.14$
$A_2 = 0.7$	$b_2 = 0.53$
$A_3 = 1.5$	$b_3 = 0.25$
$A_4 = -0.5$	$b_4 = 0.1$
	$b_5 = 0.5$

TABLE 2.1: Leishman-Beddoes indicial functions parameters

The load step responses given by equations 2.1-2.4 can be rewritten in the following continuous state space representation by using Duhamel's principle

$$\dot{\mathbf{x}} = \mathbf{A}\mathbf{x} + \mathbf{B}\begin{bmatrix}\alpha(t)\\ q(t)\end{bmatrix} \tag{2.17}$$

$$\begin{bmatrix}c_n^c\\ c_m^c\end{bmatrix} = \mathbf{C}_c\mathbf{x} \tag{2.18}$$

$$\begin{bmatrix}c_n^I\\ c_m^I\end{bmatrix} = \mathbf{C}_I\mathbf{x} + \mathbf{D}\begin{bmatrix}\alpha(t)\\ q(t)\end{bmatrix} \tag{2.19}$$

where $c_n = c_n^I + c_n^c$ and $c_m = c_m^I + c_m^c$ and $\mathbf{x}$ is the 8x1 vector.

First, for the circulatory normal force c_n^c, the state equations for x_1 and x_2 are expressed as follows

$$\begin{bmatrix}\dot{x}_1\\ \dot{x}_2\end{bmatrix} = \left(\frac{2V}{c}\right)\beta^2\begin{bmatrix}-b_1 & 0\\ 0 & -b_2\end{bmatrix}\begin{bmatrix}x_1\\ x_2\end{bmatrix} + \begin{bmatrix}1 & 0.5\\ 1 & 0.5\end{bmatrix}\begin{bmatrix}\alpha\\ q\end{bmatrix} \tag{2.20}$$

and the normal circulatory force coefficient is given by

$$c_n^c(t) = \frac{2\pi}{\beta}\left(\frac{2V}{c}\right)\beta^2\begin{bmatrix}A_1b_1 & A_2b_2\end{bmatrix}\begin{bmatrix}x_1\\ x_2\end{bmatrix} \tag{2.21}$$

For the non circulatory normal force coefficient, c_n^I, the state space equations are

$$\begin{bmatrix}\dot{x}_3\\ \dot{x}_4\end{bmatrix} = \begin{bmatrix}-\frac{1}{K_\alpha T_I} & 0\\ 0 & -\frac{1}{K_q T_I}\end{bmatrix}\begin{bmatrix}x_3\\ x_4\end{bmatrix} + \begin{bmatrix}1 & 0\\ 0 & 1\end{bmatrix}\begin{bmatrix}\alpha\\ q\end{bmatrix} \tag{2.22}$$

and the non circulatory normal force is given by

$$c_n^I(t) = \frac{4}{M}\left(-\frac{x_3}{K_\alpha T_I} + \alpha\right) + \frac{1}{M}\left(-\frac{x_4}{K_q T_I} + q\right) \tag{2.23}$$

For the circulatory moment coefficient, c_m^c, the state space equation is

$$\dot{x}_7 = -b_5\beta^2\left(\frac{2V}{c}\right)x_7 + q \tag{2.24}$$

and the circulatory moment coefficient is

$$c_m^c(t) = c_n^c(0.25 - x_{ac}) - \frac{\pi}{8\beta}\left(\frac{2V}{c}\right)\beta^2 b_5 x_7 \tag{2.25}$$

Finally, for the non circulatory moment coefficient, c_m^I, the state space equations are

$$\begin{bmatrix}\dot{x}_5\\ \dot{x}_6\\ \dot{x}_8\end{bmatrix} = \begin{bmatrix}-\frac{1}{b_3 K_{\alpha m} T_I} & 0 & 0\\ 0 & -\frac{1}{b_4 K_{\alpha m} T_I} & 0\\ 0 & 0 & -\frac{1}{K_{qm} T_I}\end{bmatrix}\begin{bmatrix}x_5\\ x_6\\ x_8\end{bmatrix} + \begin{bmatrix}1 & 0\\ 1 & 0\\ 0 & 1\end{bmatrix}\begin{bmatrix}\alpha\\ q\end{bmatrix} \tag{2.26}$$

and the non circulatory moment is given by

$$\begin{aligned} c_m^I(t) &= \frac{1}{M}\begin{bmatrix}\frac{A_3}{b_3 K_{\alpha m} T_I} & \frac{A_4}{b_4 K_{\alpha m} T_I}\end{bmatrix}\begin{bmatrix}x_5 & x_6\end{bmatrix}\\ &- \frac{1}{M}\alpha - \frac{7}{12M}\left(-\frac{x_8}{K_{qm} T_I} + q\right) \end{aligned} \tag{2.27}$$

From equations 2.20-2.27, one can easily assemble the matrices in equations 2.17, 2.18 and 2.19

$$\mathbf{A} = \begin{bmatrix} a_{11} & 0 & 0 & 0 & 0 & 0 & 0 & 0 \\ 0 & a_{22} & 0 & 0 & 0 & 0 & 0 & 0 \\ 0 & 0 & a_{33} & 0 & 0 & 0 & 0 & 0 \\ 0 & 0 & 0 & a_{44} & 0 & 0 & 0 & 0 \\ 0 & 0 & 0 & 0 & a_{55} & 0 & 0 & 0 \\ 0 & 0 & 0 & 0 & 0 & a_{66} & 0 & 0 \\ 0 & 0 & 0 & 0 & 0 & 0 & a_{77} & 0 \\ 0 & 0 & 0 & 0 & 0 & 0 & 0 & a_{88} \end{bmatrix}$$

$$\mathbf{B} = \begin{bmatrix} 1 & 1 & 1 & 0 & 1 & 1 & 0 & 0 \\ 0.5 & 0.5 & 0 & 1 & 0 & 0 & 1 & 1 \end{bmatrix}^T$$

$$\mathbf{C_c} = \begin{bmatrix} c_{11} & c_{12} & 0 & 0 & 0 & 0 & 0 & 0 \\ c_{21} & c_{22} & 0 & 0 & 0 & 0 & c_{27} & 0 \end{bmatrix}$$

$$\mathbf{C_I} = \begin{bmatrix} 0 & 0 & c_{13} & c_{14} & 0 & 0 & 0 & 0 \\ 0 & 0 & 0 & 0 & c_{25} & c_{26} & 0 & c_{28} \end{bmatrix}$$

$$\mathbf{D_I} = \begin{bmatrix} \frac{4}{M} & \frac{1}{M} \\ \frac{-1}{M} & \frac{-7}{12M} \end{bmatrix}$$

where the elements of matrix $\mathbf{A}$ are

$$\begin{aligned} a_{11} &= -\frac{2V}{c} b_1 \beta^2, & a_{22} &= -\frac{2V}{c} b_2 \beta^2 \\ a_{33} &= -\frac{1}{k_\alpha T_I}, & a_{44} &= -\frac{1}{k_q T_I} \\ a_{55} &= -\frac{1}{b_3 k_{\alpha M} T_I}, & a_{66} &= -\frac{1}{b_4 k_{\alpha M} T_I} \\ a_{77} &= -\frac{2V}{c} b_5 \beta^2, & a_{88} &= -\frac{1}{k_{qM} T_I} \end{aligned} \tag{2.28}$$

and the elements of matrices $\mathbf{C}_c$ and $\mathbf{C}_I$ are given by

$$\begin{aligned} c_{11} &= \frac{2\pi}{\beta} \frac{2V}{c} \beta^2 A_1 b_1, & c_{12} &= \frac{2\pi}{\beta} \frac{2V}{c} \beta^2 A_2 b_2 \\ c_{13} &= -\frac{4}{M} \left(\frac{1}{k_\alpha T_I} \right), & c_{14} &= -\frac{1}{M} \left(\frac{1}{k_q T_I} \right) \\ c_{21} &= c_{11}(0.25 - x_{ac}), & c_{22} &= c_{12}(0.25 - x_{ac}) \\ c_{25} &= \frac{-1}{M} \left(\frac{-A_3}{b_3 K_{\alpha M} T_I} \right), & c_{26} &= \frac{-1}{M} \left(\frac{-A_4}{b_4 K_{\alpha M} T_I} \right) \\ c_{27} &= -\frac{2\pi}{16\beta} \frac{2V}{c} \beta^2 b_5, & c_{28} &= \frac{-7}{12M} \left(-\frac{1}{k_{qM} T_I} \right) \end{aligned} \tag{2.29}$$

2.1.2 Vortex onset

One important aspect of dynamic stall that needs to be represented is vortex onset. A criterion described by Evan and Morts [58] is the existence of an extremum in pressure at the airfoil's leading edge, followed by its collapse. Leishman and Beddoes chose to define a criterion based on the normal force coefficient c_n because the leading

edge pressure applied on the airfoil can be directly linked to the normal force. They used a critical normal force static value $c_n(static) = c_{n1}$ as the criterion representing the steady lift at which vortex onset occurs for a given Mach number. Figure 2.1, built from data extracted from Leishman and Beddoes [3], shows the variation of this normal force critical criterion with Mach number for a NACA0012 airfoil. For higher Mach Numbers they used instead the shock reversal criterion where the flow separation of the boundary layer is created by adverse pressure gradient caused by shock waves on the airfoil.

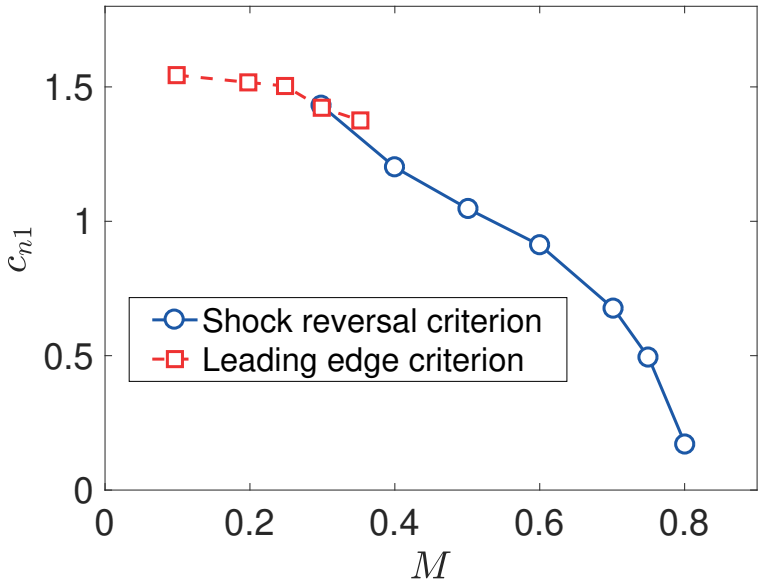

FIGURE 2.1: Critical normal force separation onset boundary for the NACA0012 airfoil.

There is a lag in the leading edge pressure response during unsteady motion. This also leads to a lag in the normal force $c_n(t)$ and, hence, vortex onset occurs at a higher instantaneous angle of attack. To implement this time delay on the vortex onset criterion, a first order lag T_p is applied to the normal lift as follows

$$\dot{c_n^{'}} = \frac{c_n^c + c_n^I - c_n^{'}}{T_p} \tag{2.30}$$

where c_n^c is the attached circulatory normal lift and c_n^I is the non circulatory normal lift. The time constant T_p is a function of Mach number and mostly independent of airfoil shape according to Leishman and Beddoes [3]. Finally, $c_n^{'}$ represent the lagged normal lift, so that vortex onset is simply reached when

$$|c_n^{'}| = c_{n1}(M) \tag{2.31}$$

assuming that the airfoil is symmetrical.

2.1.3 Trailing edge separation

Computation of $s(\alpha)$

Trailing edge stall is characterized by flow separation from the airfoil's trailing edge. The Leishman-Beddoes model uses Kirchhoff-Helmholtz [13] theory to approximate

the normal force coefficient acting on a static airfoil as

$$c_n = \frac{2\pi}{\beta}\left(\frac{1+\sqrt{s}}{2}\right)^2 \alpha \tag{2.32}$$

where $\frac{2\pi}{\beta}$ is the compressible lift curve slope, α is the angle of attack and s is the position of the separation point on the airfoil. A drawing defining the separation point s is shown in figure 2.2, $s = 1$ when the flow is fully attached and $s = 0$ when the flow is fully separated.

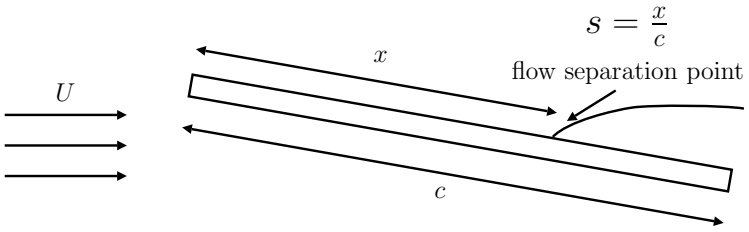

FIGURE 2.2: Flow separation scheme for a flat plate

By inverting relation 2.32, an expression for the position of the separation point s can be deduced from airfoil experimental steady data.

$$s = \left(2\sqrt{\frac{c_{n,exp}}{\frac{2\pi}{\beta}(\alpha - \alpha_0)}} - 1\right)^2 \tag{2.33}$$

This gives a value of s at each angle of attack at which c_n was measured but an analytic function $s(\alpha)$ is required by the model. Leishman and Beddoes [3] chose the relation

$$s = \begin{cases} 1 - 0.3\exp\left\{(\alpha - \alpha_1)/S_1\right\} & \alpha \leq \alpha_1 \\ 0.04 + 0.66\exp\left\{(-\alpha + \alpha_1)/S_2\right\} & \alpha > \alpha_1 \end{cases} \tag{2.34}$$

where coefficients S_1 and S_2 define static stall characteristics and α_1 corresponds to the static stall angle which, for most airfoils, occurs when $s \simeq 0.7$. These coefficients are chosen to fit the data obtained from equation 2.33. Figure 2.3 shows an example of such a fit from data obtained during the course of the present research. The fit is very good for $\alpha > 6$ but unsatisfactory for $alpha < 6$, due to the presence of a laminar separation bubble near the leading edge at these low angles of attack. The phenomenon will be discussed in more detail in a later chapter.

Computation of $g(s)$

A general expression for the pitching moment around the quarter chord cannot be obtained from Kirchhoff theory. Leishman [57] chose to empirically represent the position of the center of pressure as a function of the position of the separation point. The center of pressure position can be determined from the ratio $\frac{c_m - c_{m0}}{c_n}$ where c_{m0} is the steady moment coefficient at zero lift. Leishman proposed the following fit

$$g(s) = \frac{c_m - c_{m0}}{c_n} = K_0 + K_1(1-s) + K_2\sin(\pi s^m) \tag{2.35}$$

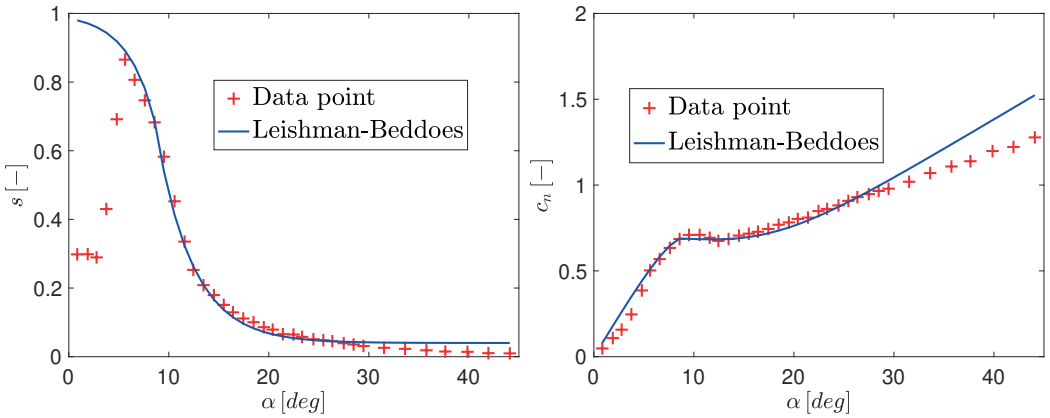

(a) Curve fitting of function s(α) (b) reconstructed c_n

FIGURE 2.3: Leishman-Beddoes fitting of the separation point for the normal force

Parameters K_0, K_1, K_2 and m can be adjusted for different airfoils to give the best moment reconstruction using a least squares fit; An exemple of curve fit of the function $g(f)$ and the reconstructed pitching moment coefficient is shown in figure 2.4.

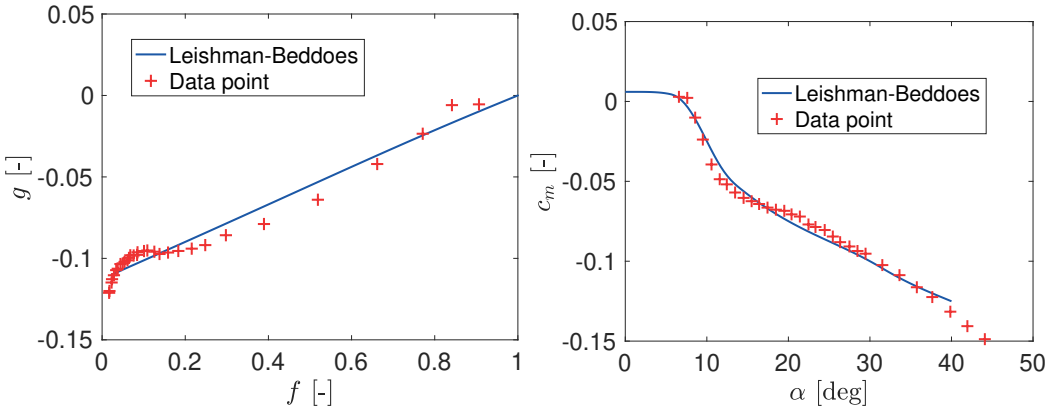

(a) Curve fitting of function g(α) (b) reconstructed c_m

FIGURE 2.4: Leishman-Beddoes fitting of the separation point for the pitching moment

Dynamic effects on $s(\alpha)$ and $g(s)$

For dynamic cases, flow separation will occur at a higher angle of attack than in the static case. This is caused by a delay in the airfoil pressure distribution and boundary layer dynamic response.

The delay in the pressure distribution can be expressed using an effective angle of attack $\alpha_s(t)$ which is computed from the delayed normal lift response $c_n^{'}$, computed using equation 2.30, as follows

$$\alpha_s(t) = \frac{c_n^{'}}{2\pi/\beta} \tag{2.36}$$

This effective angle of attack is used to represent the first order T_p which, as explained previously, represents a delay in the pressure response.

The effect of the unsteady boundary layer is represented by applying a first order lag to the computation of $s(\alpha_s)$. This gives the following unsteady trailing edge separation point $s^{'}$

$$\dot{s^{'}} = \frac{s(\alpha_s) - s^{'}}{T_a} \tag{2.37}$$

As for T_p, the constant time delay T_a is Mach number dependent.

Finally, the unsteady nonlinear normal force c_n^f is given by

$$c_n^f(t) = c_n^c \left(\frac{1 + \sqrt{s^{'}}}{2} \right)^2 \tag{2.38}$$

and the unsteady nonlinear pitching moment c_m^f is

$$c_m^f = g(s^{'}) c_n^c + c_{m_0} \tag{2.39}$$

2.1.4 Dynamic stall modelling

One of the aspects of dynamic stall involves the formation of a vortex at the leading edge. At some point this vortex detaches and travels downstream, disturbing the flow field as explained in the previous section 1.1.2.

Leishman [3] proposed to add a normal lift term c_n^v that represents an excess of circulation that has not shed until some critical condition is reached. This critical condition, is the vortex onset which was defined in sections 2.1.2 as

$$c_n^{'}(t) \geq c_{n_1} \tag{2.40}$$

At vortex onset, the accumulated circulation is shed over the airfoil. This process is represented by equation

$$\dot{c_n^v}(t) = \frac{\dot{c_v} - c_n^v}{T_v} \tag{2.41}$$

where

$$c_v = \begin{cases} c_n^c - c_n^f & \text{for } \tau_v \leq 2T_{vl} \\ 0 & \text{for } \tau_v > 2T_{vl} \end{cases} \tag{2.42}$$

In this formulation, the accumulation of circulation c_n^v is proportional to the rate of change of circulation $\frac{d\Gamma}{dt} \propto \dot{c_v}$ and dissipates with a time constant T_v. As a result, c_n^v can only increases or accumulates when there is a rates of change greater than the dissipation term T_v. At lower rates of change, the dissipation term dominates and the airload will revert smoothly back to the steady nonlinear condition with $c_n^v = 0$.

When the critical conditions for leading edge separation occurs, i.e. $c_n^{'}(t)$ exceeds c_{n_1}, there is an abrupt loss of leading edge suction and the accumulated vortex starts to convect over the airfoil's chord. At this point, a non dimensional time $\tau_v = 0$ is defined to track the position of the vortex. The time taken by the vortex to reach the trailing edge is defined as $\tau_v = T_{vl}$. The Leishman beddoes model assumes that the circulation keeps building up during the convection process. Finally, the build up is assumed to stop when the vortex is located far enough from the airfoil $\tau_v = 2T_{vl}$.

The position of the center of pressure is disturbed by the movement of the vortex along the airfoil, affecting the pitching moment acting on the airfoil. The Leishman-Beddoes model proposes the following approximation of the motion of the center of pressure,

$$C_{P_v} = 0.25 \left[1 - \cos\left(\frac{\pi \tau_v}{T_{vl}} \right) \right] \tag{2.43}$$

The center of pressure is assumed to reach the mid-chord when the vortex is located at the trailing edge ($\tau_v = T_{vl}$).

The pitching moment perturbation created by the vortex, c_m^v, is then simply

$$c_m^v = -C_{P_v} \; c_n^v \tag{2.44}$$

2.1.5 Coupling of the stall mechanisms

As noted by Leishman and Beddoes [59], the model described in the previous section involves different mechanisms associated with dynamic stall which are assumed to be uncoupled.

In reality, these different mechanisms can interact with each other. First of all, vortex shedding, which is a leading edge phenomenon, has an effect on trailing edge separation. In fact, vortex shedding increases the speed with which the trailing edge separation point moves towards the leading edge. To represent this behavior, the model discreetly changes the time constant T_f associated with trailing edge separation as a function of the position of the vortex on the airfoil, as shown in table 2.2 summarized by Chantharasenawong [60].

$c_n^{'} \geq c_{n_1}$	$0 \leq \tau_v \leq T_{vl}$	$T_{vl} < \tau_v \leq 2T_{vl}$	$2T_{vl} < \tau_v$
$\alpha\dot{\alpha} \geq 0$	$T_f = T_{f_0}$	$T_f = \frac{1}{3} T_{f_0}$	$T_f = 4T_{f_0}$
$\alpha\dot{\alpha} < 0$	$T_f = 0.5T_{f_0}$	$T_f = 0.5T_{f_0}$	$T_f = 4T_{f_0}$

TABLE 2.2: Variation of the trailing edge separation lag parameters T_f during the vortex shedding phase.

In section 2.1.4, it is assumed that the shedding of the vortex has no effect on the accumulation and dissipation of the term c_n^v while the vortex is close to the airfoil. However, when the vortex starts to move, the model should increase the dissipation rate of the accumulated circulation. This can be done by decreasing the time constant T_v as a function of the position of the vortex, as shown in table 2.3 summarized by Chantharasenawong [60].

$c_n^{'} \geq c_{n_1}$	$0 \leq \tau_v \leq T_{vl}$	$T_{vl} < \tau_v \leq 2T_{vl}$	$2T_{vl} < \tau_v$
$\alpha\dot{\alpha} \geq 0$	$T_v = T_{v_0}$	$T_v = 0.25T_{v_0}$	$T_v = 0.9T_{v_0}$
$\alpha\dot{\alpha} < 0$	$T_v = 0.5T_{v_0}$	$T_v = 0.5T_{v_0}$	$T_v = 0.9T_{v_0}$

TABLE 2.3: Variation of the vortex dissipation time parameters T_v during the vortex shedding phase.

2.1.6 Complete equations

Finally, the equations for the total unsteady aerodynamic loads can be assembled. First the state space variables are computed from the following state space equations.

$$\begin{aligned}
\dot{\mathbf{x}} &= \mathbf{A}\mathbf{x} + \mathbf{B}\begin{bmatrix}\alpha(t)\\ q(t)\end{bmatrix} \\
\dot{c_n^{'}} &= \frac{c_n^c + c_n^I - c_n^{'}}{T_p} \\
\dot{s^{'}} &= \frac{s(\alpha_s) - s^{'}}{T_a} \\
\dot{c_n^v}(t) &= \frac{\dot{C}_v - c_n^v}{T_v}
\end{aligned}$$

Then, the aerodynamic loads are defined by the relations

$$\begin{aligned}
\begin{bmatrix}c_n^c\\ c_m^c\end{bmatrix} &= \mathbf{C_c}\mathbf{x} \\
\begin{bmatrix}c_n^I\\ c_m^I\end{bmatrix} &= \mathbf{C_I}\mathbf{x} + \mathbf{D_l}\begin{bmatrix}\alpha(t)\\ q(t)\end{bmatrix} \\
c_n^f(t) &= c_n^c\left(\frac{1+\sqrt{s^{'}}}{2}\right)^2 \\
c_m^f &= g(s^{'})c_n^c + c_{m_0} \\
c_m^v &= -C_{P_v}\, c_n^v \\
c_n &= c_n^f + c_n^v + c_n^I \\
c_m &= c_m^f + c_m^v + c_m^I
\end{aligned}$$

2.2 Modified Leishman-Beddoes model

Sheng et al.[33]–[35] showed that at lower Mach numbers the LB model required modifications in order to better correspond to experimental observations. In particular, the computation of dynamic stall onset and vortex onset must be modified at such Mach numbers.

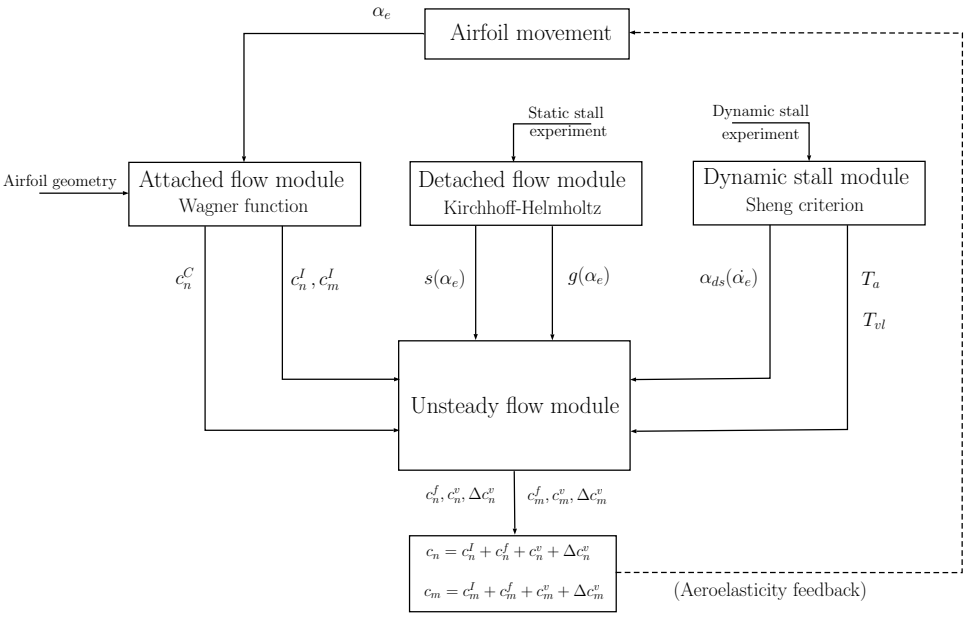

FIGURE 2.5: Modified Leishman Beddoes overview

As discussed in section 2.1, the Leishman Beddoes model applies to rigid airfoils with pitch and/or plunge degrees of freedom undergoing forced motion, usually sinusoidal or constant pitch-up. It can represent stall delay, trailing edge separation and the shedding of leading edge vortices. Its inputs are the airfoil geometry, flight condition and motion and its outputs are the unsteady aerodynamic loads as a function of time. The modified version of the model proposed here can be visualized as a block diagram (see figure 2.5) containing the following blocks:

- **Attached flow module:** This module computes the circulatory and impulsive normal loads acting on the airfoil, c_n^c and c_n^I respectively. It will take as inputs :
  - The pitch and/or plunge motion of the rigid airfoil section;
  - The airfoil geometry.
- **Detached flow module:** This module represents the nonlinear effects of separation and stall delay on the aerodynamic load responses. It will use as input :
  - The experimental static stall characteristics for pitching moment and normal force.

  Flow separation is represented by the location of the separation point s and the position of the center of pressure g which are obtained from the static experimental data. Leishman and Beddoes [3] used a preset function to fit the experimental result 2.34. In the current model, the functions s and g are curve fitted with a series of cubic splines. The position of the center of pressure is also

defined directly as a function of the angle of attack $g(\alpha)$ instead of a function of the separation point $g(s)$ as previously defined by Leishman and Beddoes 2.35.

- **Dynamic stall module:** This module creates a function $\alpha_{ds}(r(t))$ that estimates the angle of attack at which vortex shedding will begin, if there is one. It also calculates a characteristic unsteady time lag T_a applied to the angle of attack and to the separation point

$$\dot{\alpha'} = \frac{U}{b}\frac{\alpha_e - \alpha'}{T_a} \tag{2.45}$$

$$\dot{s'} = \frac{U}{b}\frac{s_s(\alpha_e) - s'}{T_a} \tag{2.46}$$

  where α_e is the effective angle of attack due to the motion, to be defined in section 2.2.1. Finally, this module also calculates the time taken by the vortex to shed over the airfoil, T_{vl}. It will take as input :

  – The airfoil experimental dynamic stall characteristics at different amplitudes and reduced frequencies.

  The angle of vortex shedding onset α_{ds} was defined by Sheng et. al. [33] to replace the Leishman [3] criterion at low Reynold numbers. Sheng et. al. curve fitted the result with a set of two linear function. In the present model, the function α_{ds} is fitted with the inverse of a second order polynomial.

- **Unsteady flow module:** This final module computes the aerodynamic loads acting on the airfoil.

2.2.1 Attached flow module

Circulatory lift

In the classical Leishman-Beddoes model, the circulatory loading associated with the unsteady attached flow is computed by means of indicial compressible aerodynamic response functions. As the flow is assumed incompressible in the present work, the step change in lift coefficient, for an airfoil undergoing a step change in downwash $\Delta w << U$, is expressed using the Wagner function, $\Phi(t)$, as follows :

$$c_n^c(t) = a_0 \Phi(t) \frac{\Delta w}{U} \tag{2.47}$$

where a_0 is the lift curve slope of the airfoil, which is usually approximated by 2π for thin airfoils, while $\Phi(t)$ is Jones' [61] approximation of the Wagner function

$$\Phi(t) = 1 - \Psi_1 e^{-\frac{\epsilon_1 U}{b} t} - \Psi_2 e^{-\frac{\epsilon_2 U}{b} t}$$

with $\Psi_1 = 0.165$, $\Psi_2 = 0.335$, $\epsilon_1 = 0.0455$, $\epsilon_2 = 0.3$.

Duhamel's principle can be applied to equation 4.9 in order to express a continuous lift response as the time integral of infinitesimal step responses [62]

$$c_n^c(t) = a_0 \left(\frac{w(0)}{U}\Phi(t) + \int_0^t \frac{1}{U}\frac{\partial w(\tau)}{\partial \tau}\Phi(t-\tau)\, d\tau \right) \tag{2.48}$$

where $w(t)$ is the downwash at time t and τ is an integration variable. The troublesome $\frac{\partial w(\tau)}{\partial \tau}$ term inside the integral can be removed by applying integration by parts, such

that

$$c_n^c(t) = a_0 \left(\frac{w(t)}{U} \Phi(0) - \int_0^t \frac{1}{U} \frac{\partial \Phi(t-\tau)}{\partial \tau} w(\tau)\, \mathrm{d}\tau \right) \tag{2.49}$$

The downwash $w(t)$ must now be computed as a function of the kinematics of the wing. In this work, the modified Leishman-Beddoes model is presented in a general formulation involving pitch and plunge degrees of freedom. Figure 4.1 defines the plunge, $h(t)$, and pitch, $\alpha(t)$, degrees of freedom, the chord c, and the distance between the pitch axis and the half-chord, x_e. The downwash becomes

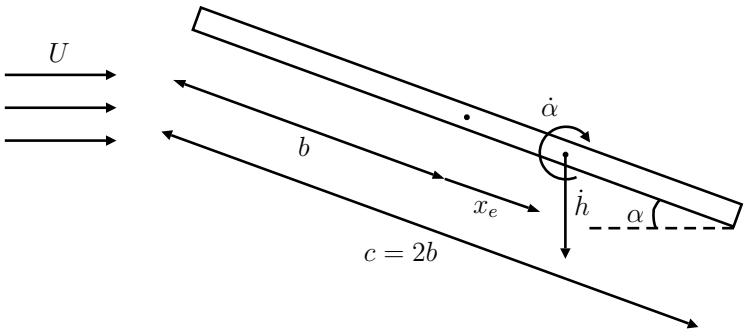

FIGURE 2.6: Rigid thin plate airfoil scheme

$$w(t) = U\alpha(t) + \dot{h}(t) + \dot{\alpha}(t)d \tag{2.50}$$

where $d = (1/2 - a)b$ and $a = x_e/b$. Note that this definition of $w(t)$ assumes low pitch and plunge velocities and small angles of attack. Nevertheless, the definition is retained for higher angles of attack, because the lift is modified by the detached flow module, as explained in section 2.2.2. From the downwash, an effective angle of attack is defined as

$$\alpha_e = \frac{w}{U} \tag{2.51}$$

After combining equations 4.11 and 4.12, the circulatory normal force coefficient becomes

$$\begin{aligned} \frac{c_n^c(t)}{a_0} &= \left(\alpha + \frac{\dot{h}}{U} + \frac{\dot{\alpha} d}{U} \right) \Phi(0) \\ &+ \underbrace{\int_0^t \Psi_1 \epsilon_1 \frac{U}{b} e^{\frac{-\epsilon_1 U}{b}(t-\tau)} \left(\alpha(\tau) + \frac{\dot{h}(\tau)}{U} + \frac{\dot{\alpha}(\tau) d}{U} \right) d\tau}_{I} \\ &+ \underbrace{\int_0^t \Psi_2 \epsilon_2 \frac{U}{b} e^{\frac{-\epsilon_2 U}{b}(t-\tau)} \left(\alpha(\tau) + \frac{\dot{h}(\tau)}{U} + \frac{\dot{\alpha}(\tau) d}{U} \right) d\tau}_{II} \end{aligned} \tag{2.52}$$

Following Lee et al. [63], the following changes of variables are performed in order to eliminate the integrals from equation 4.13

$$\begin{aligned} z_1(t) &= \int_0^t e^{\frac{-\epsilon_1 U}{b}(t-\tau)} h(\tau)\, d\tau & z_3(t,y) &= \int_0^t e^{\frac{-\epsilon_1 U}{b}(t-\tau)} \alpha(\tau)\, d\tau \\ z_2(t) &= \int_0^t e^{\frac{-\epsilon_2 U}{b}(t-\tau)} h(\tau)\, d\tau & z_4(t,y) &= \int_0^t e^{\frac{-\epsilon_2 U}{b}(t-\tau)} \alpha(\tau)\, d\tau \end{aligned} \tag{2.53}$$

where the variables $z_i(t)$ are called aerodynamics states. Working through the integrals,

$$\begin{aligned} I &= \Psi_1 \epsilon_1 \frac{U}{b} \int_0^t e^{\frac{-\epsilon_1 U}{b}(t-\tau)} \left(\underbrace{\alpha(\tau)}_{e_1} + \underbrace{\frac{\dot{h}(\tau)}{U}}_{e_2} + \underbrace{\frac{\dot{\alpha}(\tau) d}{U}}_{e_3} \right) d\tau \\ e_1 &= \int_0^t e^{\frac{-\epsilon_1 U}{b}(t-\tau)} \alpha(\tau)\, d\tau = z_3(t) \\ e_2 &= \int_0^t e^{\frac{-\epsilon_1 U}{b}(t-\tau)} \frac{\dot{h}(\tau) d}{U} d\tau = \left[e^{\frac{-\epsilon_1 U}{b}(t-\tau)} \frac{h(\tau)}{U} \right]_0^t - \int_0^t \frac{\epsilon_1 U}{b} e^{\frac{-\epsilon_1 U}{b}(t-\tau)} \frac{h(\tau)}{U} d\tau \\ &= \frac{h(t)}{U} - \frac{h(0)}{U} e^{-\frac{\epsilon_1 U}{b}} - \frac{\epsilon_1}{b} z_1(t) \\ e_3 &= \frac{\alpha(t) d}{U} - \frac{\alpha(0) d}{U} e^{-\frac{\epsilon_1 U}{b}} - \frac{\epsilon_1 d}{b} z_3(t) \\ I &= \Psi_1 \epsilon_1 \frac{U}{b} \left(\frac{h}{U} + \frac{\alpha d}{U} - \left(\frac{h(0)}{U} + \frac{\alpha(0) d}{U} \right) e^{-\frac{\epsilon_1 U}{b}} - \frac{\epsilon_1}{b} z_1 + \left(1 - \frac{\epsilon_1 d}{b} \right) z_3 \right) \\ II &= \Psi_2 \epsilon_2 \frac{U}{b} \left(\frac{h}{U} + \frac{\alpha d}{U} - \left(\frac{h(0)}{U} + \frac{\alpha(0) d}{U} \right) e^{-\frac{\epsilon_2 U}{b}} - \frac{\epsilon_2}{b} z_2 + \left(1 - \frac{\epsilon_2 d}{b} \right) z_4 \right) \end{aligned} \tag{2.54}$$

The unsteady normal force coefficient is then expressed as follows:

$$\begin{aligned} \frac{c_n^c(t)}{a_0} &= \left(\alpha + \frac{\dot{h}}{U} + \frac{\dot{\alpha} d}{U} \right) \Phi(0) - \dot{\Phi}(t) \left(\frac{h(0)}{U} + \frac{\alpha(0) d}{U} \right) \\ &+ \dot{\Phi}(0) \left(\frac{h}{U} + \frac{\alpha d}{U} \right) - \Psi_1 \epsilon_1^2 \frac{U}{b^2} z_1 - \Psi_2 \epsilon_2^2 \frac{U}{b^2} z_2 \\ &+ \Psi_1 \epsilon_1 \frac{U}{b} \left(1 - \frac{\epsilon_1 d}{b} \right) z_3 + \Psi_2 \epsilon_2 \frac{U}{b} \left(1 - \frac{\epsilon_2 d}{b} \right) z_4 \end{aligned} \tag{2.55}$$

First order differential equations for the aerodynamic state variables can be obtained by applying Leibnitz's integral rule, such that

$$\begin{aligned} \dot{z_1}(t) &= h - \frac{\epsilon_1 U}{b} z_1(t) & \dot{z_3}(t) &= \alpha - \frac{\epsilon_1 U}{b} z_3(t) \\ \dot{z_2}(t) &= h - \frac{\epsilon_2 U}{b} z_2(t) & \dot{z_4}(t) &= \alpha - \frac{\epsilon_2 U}{b} z_4(t) \end{aligned} \tag{2.56}$$

Finally, the continuous unsteady circulatory lift coefficient can be written as follows

$$c_n^c(t) = \mathbf{C}\dot{\mathbf{q}} + \mathbf{D}\mathbf{q} + \mathbf{E}\mathbf{z} + \chi\dot{\Phi}(t) \tag{2.57}$$
$$\dot{\mathbf{z}} = \mathbf{W}\mathbf{z} + \mathbf{F}\mathbf{q} \tag{2.58}$$

where

$$\begin{aligned}
\mathbf{q} &= \begin{bmatrix} h(t) & \alpha(t) \end{bmatrix}^T \\
\mathbf{z} &= \begin{bmatrix} z_1(t) & z_2(t) & z_3(t) & z_4(t) \end{bmatrix}^T \\
\mathbf{D} &= \frac{a_0}{U}\begin{bmatrix} \dot{\Phi}(0) & U\Phi(0) + d\dot{\Phi}(0) \end{bmatrix} \\
\mathbf{E} &= \frac{a_0 U}{b}\begin{bmatrix} -\frac{\Psi_1\epsilon_1^2}{b} & -\frac{\Psi_2\epsilon_2^2}{b} & \Psi_1\epsilon_1\left(1-\epsilon_1\frac{d}{b}\right) & \Psi_2\epsilon_2\left(1-\epsilon_2\frac{d}{b}\right) \end{bmatrix} \\
\mathbf{C} &= \frac{a_0}{U}\Phi(0)\begin{bmatrix} 1 & d \end{bmatrix} \\
\chi &= -\frac{a_0}{U}\left(h(0) + d\alpha(0)\right) \\
\mathbf{W} &= -\frac{U}{b}\mathrm{diag}\left(\epsilon_1\,,\epsilon_2\,,\epsilon_1\,,\epsilon_2\right) \\
\mathbf{F} &= \begin{bmatrix} 1 & 1 & 0 & 0 \\ 0 & 0 & 1 & 1 \end{bmatrix}^T
\end{aligned}$$

while the pitching moment coefficient around the pitching axis is obtained from

$$c_m^c(t) = \frac{1}{2}\left(\frac{1}{2} + a\right)c_n^c(t) - \frac{1}{2}\left(\frac{1}{2} - a\right)\frac{\pi b}{U}\dot{\alpha} \tag{2.59}$$

There is also an additional moment coefficient associated with the circulatory flow, given by Fung [62]

$$c_{m_1}^c(t) = -\frac{1}{2}\left(\frac{1}{2} - a\right)\frac{\pi b}{U}\dot{\alpha} = \mathbf{B_m}\dot{\mathbf{q}} \tag{2.60}$$

As this term is circulatory, it will be affected by flow separation.

Impulsive loads

The non-circulatory sectional lift and moment coefficients, also known as the added mass effect, can be computed from the non-circulatory terms derived by Theodorsen [64] and presented by Fung [62]

$$c_n^I = \frac{\pi b}{U^2}\left(\ddot{h} - a\,b\,\ddot{\alpha}\right) + \frac{\pi b}{U}\dot{\alpha} = \mathbf{A_n}\ddot{\mathbf{q}} + \mathbf{B_n}\dot{\mathbf{q}} \tag{2.61}$$
$$c_m^I = \frac{\pi b}{2U^2}\left[a\ddot{h} - \left(a^2 + \frac{1}{8}\right)b\ddot{\alpha}\right] = \mathbf{A_m}\ddot{\mathbf{q}} \tag{2.62}$$

As these termes are non-circulatory, they are assumed to be unaffected by flow separation.

2.2.2 Detached flow module

This module aims to compute the non linear effect of flow separation on the normal force and pitching moment coefficients. To this end, empirical functions $s(\alpha)$ and $g(\alpha)$ are developed from steady experimental data. Furthermore, this module represents

the stall delay phenomenon by applying a time delay T_a to the instantaneous effective angle of attack.

Computation of $s(\alpha)$

Similarly to equation 2.32, Kirchhoff-Helmholtz theory [13] is used to represent the effects of the flow separation on the normal force coefficient.

$$c_n = a_0 (\alpha - \alpha_0) \left(\frac{1 + \sqrt{s(\alpha)}}{2} \right)^2 \tag{2.63}$$

where a_0 is the lift curve slope, α is the angle of attack, α_0 is the zero lift angle and s is the position of the separation point on the airfoil, as defined in figure 2.2.

Equation 2.63 is a simple model to compute the nonlinear force and moment behavior due to a progressive trailing edge separation process. However, it can also be used to represent separation created by leading edge stall. As explained in section 1.1.1, leading edge stall induces the sudden separation of the whole flow around the airfoil, which can be represented with equation 2.63 with a sudden change of the position of the separation point $s(\alpha)$.

By inverting relation 2.63, an expression for the separation point s can be deduced from experimental steady normal load data,

$$s(\alpha) = \left(2\sqrt{\frac{c_n}{a_0 (\alpha - \alpha_0)}} - 1 \right)^2 \tag{2.64}$$

This expression gives the values of s at all the discrete angles of attack at which c_n was measured but an analytic function $s(\alpha)$ is required by the model.

In this modified version of the Leishman-Beddoes model, the static separation function s is curve fitted by a set of cubic splines to obtain the function $s_s(\alpha)$, where the subscript s denotes steady conditions. This choice affords much greater flexibility for modelling $s(\alpha)$ data from any lift curve in comparison to equation 2.34.

Figure 2.7 demonstrates the proposed fitting process for a NACA 0012 static lift curve obtained in chapter 3. Equation 2.64 is applied to this lift curve in order to obtain the data points (crosses) in figure 2.7(a). These points are then curve-fitted by cubic splines in order to obtain the solid line. The figure also plots the best fit obtained with the classic Leishman-Beddoes method from equation 2.34 (line and circles), demonstrating that the cubic spline approach follows the data much better for all angles $\alpha > 5°$. Function $s_s(\alpha)$ can then be substituted into equation 2.63 to reconstruct the normal force curve. Figure 2.7(b) shows that the reconstruction obtained from the cubic spline fit is much more accurate than the one obtained from equation 2.34, especially for angles of attack $\alpha > 25°$. Furthermore, as cubic splines are analytic, function $s_s(\alpha)$ is also analytic.

It should be noted that both curve fits in figure 2.7 are inaccurate for angles $\alpha < 5°$ because the Kirchhoff-Helmholtz model only represents a “trailing edge" stall mechanism, whereas the experimental data suggest that a laminar separation bubble forms near the leading edge at low angles of attack. Nevertheless, function $s(\alpha)$ only aims to represent the trailing edge separation process, so the impact of the laminar separation bubble near the leading edge has been ignored when computing the curve fit of $s_s(\alpha)$.

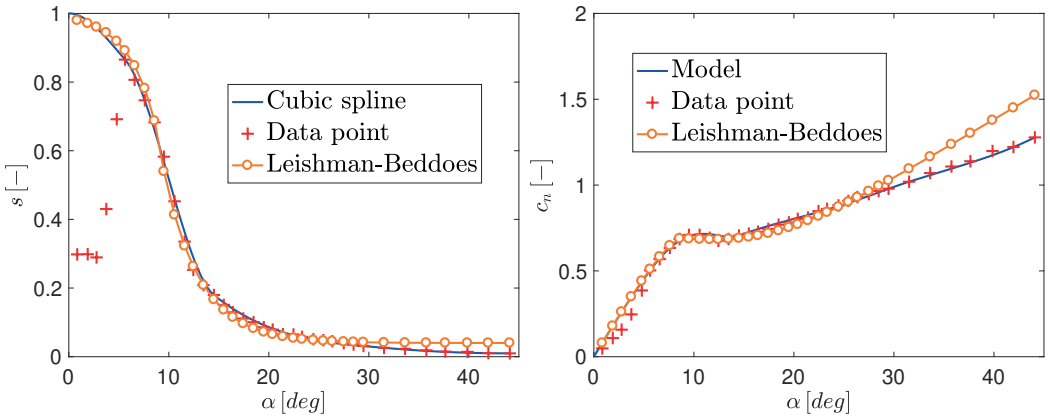

(a) Curve fit of function s(α) (b) Reconstructed c_n

FIGURE 2.7: Curve fitting function s(α) for the NACA0012 wing using cubic splines

Computation of $g(\alpha)$

Under attached flow conditions and thin airfoil theory assumptions the aerodynamic centre of a 2D wing section lies on the quarter chord, which means that the pitching moment around $c/4$ is constant with angle of attack. As the flow separates this is no longer the case and the aerodynamic centre starts to move downstream, as shown in figure 2.8. Function $g(\alpha)$ is estimated experimentally in a similar way as for the classical Leishman-Beddoes [3] in equation 2.35 which is repeated here

$$g(\alpha) = \frac{c^0_{m_{1/4}} - c_{m_{1/4}}}{c_n} \tag{2.65}$$

where $c_{m_{1/4}}$ is the measured moment coefficient at the quarter chord, c_n is the measured normal force coefficient and $c^0_{m_{1/4}}$ is the zero lift moment coefficient at the quarter chord.

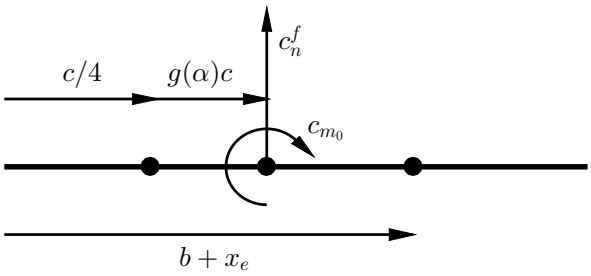

FIGURE 2.8: Position of the point of application of the normal force under separated flow conditions.

As in the case of the separation point position $s(\alpha)$, equation 2.65 gives $g(\alpha)$ at the discrete angles of attack at which the normal force and pitching moment coefficients were measured from static tests. In order to obtain an analytical expression for $g(\alpha)$,

the empirical relation g is computed directly as a function of the angle of attack and cubic splines are used in order to curve fit $g_s(\alpha)$ from experimental data, as shown in figure 2.9. Again, cubic splines can fit the data with better accuracy than equation 2.35, as cubic splines are more flexible. Furthermore $g_s(\alpha)$ can be easily extended to negative angles of attack, which is not as straightforward for $g(s)$ from equation 2.35.

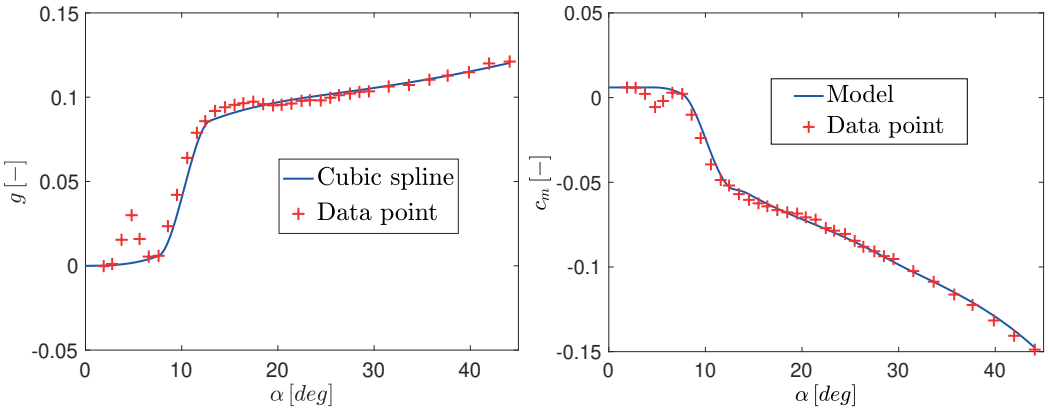

(a) Curve fit of function $g(\alpha)$ (b) Reconstructed c_m

FIGURE 2.9: Curve fitting function $g(\alpha)$ for the NACA0012 wing using cubic splines

In figure 2.9(a), obtained with data from chapter 3 ,$g_s(\alpha)$ is equal to zero at angles $\alpha < 5°$ and at around $\alpha = 10°$, denoting fully attached flow. In the interval $5° < \alpha < 10°$, $g_s(\alpha)$ increases up to 0.03 and then decreases again. Again, this phenomenon is assumed to be due to a laminar separation bubble at this low Reynolds number; it is ignored in the computation of $g(\alpha)$ because the model does not aim to represent the effects of separation bubbles. Once the function $g_s(\alpha)$ has been evaluated, the pitching moment coefficient around the pitch axis can be computed from

$$c_m = \left(\frac{1}{2}\left(\frac{1}{2} + a\right) - g_s(\alpha)\right) c_n + c^0_{m_{1/4}} \tag{2.66}$$

Cubic spline curve fit

The functions $s(\alpha)$ and $g(\alpha)$ are curve fitted with a series of cubic splines defined by a chosen number of N nodes as follows

$$v(\alpha) = \begin{cases} i_{1,0}\alpha^3 + j_{1,0}\alpha^2 + k_{1,0}\alpha + l_{1,0} & \text{for} \quad \alpha \leq \alpha_0 \\ i_{n,n-1}\alpha^3 + j_{n,n-1}\alpha^2 + k_{n,n-1}\alpha + l_{n,n-1} & \text{for} \quad \alpha_{n-1} \leq \alpha \leq \alpha_n \\ i_{N,N-1}\alpha^3 + j_{N,N-1}\alpha^2 + k_{N,N-1}\alpha + l_{N,N-1} & \text{for} \quad \alpha \geq \alpha_N \end{cases} \tag{2.67}$$

Each node is defined by its position and the slope of the function going trough the node $(v(\alpha_n), \frac{dv(\alpha_n)}{d\alpha})$. These nodes are fixed in order to get a solution for the parameters i_n, j_n, k_n and l_n.

The positions of the nodes are chosen manually. Two nodes are placed at each extremity of the dataset to avoid unwanted extrapolation. Nodes are placed at angles of attack where the slope changes abruptly in order to prevent exaggerated oscillations of the spline. The slopes at each node are obtained by a least squares fit of the

experimental data points (α_i, f_i) using the following error criterion

$$e = \sum_{i=1}^{E} (v(x_i) - v_i)^2 \tag{2.68}$$

except for the slopes of the first and last nodes, which are set manually. For the computation of $s(\alpha)$, the effects of the laminar bubble are ignored by removing the first few data points of $s(\alpha)$ up to the first local maximum of $s_s(\alpha)$. At this point, we assume that "trailing edge" separation is the dominant effect. The first node is fixed manually at $\alpha_0 = 0°$. The airflow is expected to be fully attached at zero angle of attack and $s(\alpha)$ should decrease as the angle of attack becomes positive or negative. Consequently, the first node is defined as

$$\alpha_0 = 0°, \quad s(\alpha_0) = 1, \quad \frac{ds(\alpha_0)}{d\alpha} = 0 \tag{2.69}$$

The complete node locations for $s(\alpha)$ are shown in figure 2.10(a) for the NACA0012 airfoil, obtained with data from chapter 3.

For the computation of $g(\alpha)$, the effects of the laminar bubble are removed by ignoring the same data points as for the computation of $s(\alpha)$. Again, the first node is set manually. The center of pressure is assumed to be located at the quarter chord at zero angle of attack and should slowly move toward the mid-chord as the angle of attack increases. The first node is then

$$\alpha_0 = 0, \quad g(\alpha_0) = 0, \quad \frac{dg(\alpha_0)}{d\alpha} = 0 \tag{2.70}$$

Figure 2.10(b) plots the node locations for the NACA0012 and for the $g(\alpha)$ function.

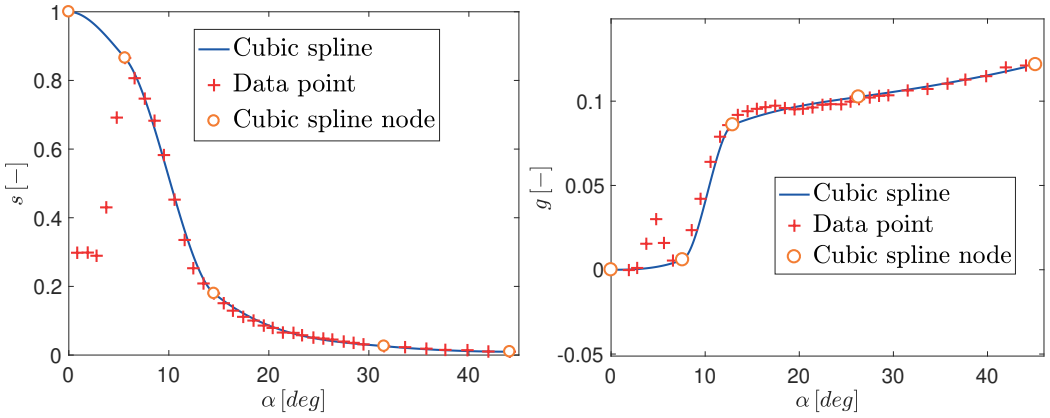

(a) Curve fit of function $s(\alpha)$ (b) Curve fit of function $g(\alpha)$

FIGURE 2.10: Curve fitting function $s(\alpha)$ and $g(\alpha)$ for the NACA0012 wing showing the cubic splines nodes

2.2.3 Dynamic stall module

This module models dynamic stall, stall delay and the effect of the shedding and motion of the leading edge vortex. In particular, the time instance at which the vortex is shed and the time it takes to clear the trailing edge are estimated from the

load measurements obtained during the dynamic tests. Furthermore, the aerodynamic load overshoot due to the passage of the vortex is included in the model.

Dynamic stall onset

Dynamic stall onset angle, α_{ds}, is defined as the angle at which the vortex is shed. If no LEV is involved, the dynamic stall onset angle can be defined as the angle at which the lift versus instantaneous pitch angle curve starts to depart from linearity.

It is therefore important to determine the dynamic stall onset angle for all the different airfoils. Sheng and Galbraith [33] stated that the dynamic stall onset involving a Leading Edge Vortex can be identified from experimental plots of the aerodynamic loads against instantaneous angle of attack by looking for one or more of the following:

- A change of slope in the normal force coefficient;
- A local maximum in the upstroke section of the chordwise force coefficient;
- A sudden drop in the pitching moment coefficient by $\Delta c_m = 0.05$.

More generally, these criteria stem from the collapse of the pressure coefficient at the airfoil's leading edge, which occurs when the leading edge vortex start to shed over the airfoil and leave the leading edge.

Figures 2.11(a), 2.11(b), and 2.11(c) show an example of the experimentally measured median and interquartile envelopes for the normal force, chordwise force and pitching moment coefficients respectively, plotted against instantaneous pitch angle. The airfoil is the NACA0012 showcased in chapter 3, oscillating with mean angle of $A_0 = 10°$, amplitude $A = 10°$ and frequency $f = 5$ Hz. On each of the figures, the dynamic stall onset angle is identified, according to the three criteria given above.

Sheng and Galbraith [33] showed that there is a degree of uncertainty in the measurement of the angle of dynamic stall onset depending on the choice of onset criterion. In their case, the dispersion was of the order of around one degree. Figures 2.11(a), 2.11(b), and 2.11(c) show a greater dispersion for the onset angle (of the order of 3 degrees). Of the three criteria, the change of slope in c_n is difficult to locate precisely and the drop of $\Delta c_m = 0.05$ seems arbitrary. The maximum of the chordwise force coefficient, figure 2.11(b), is the most robust criterion for locating the dynamic stall onset in this example.

Sheng et al [33], [35] related the dynamic stall angle for airfoils at low Mach numbers to the constant reduced pitch rate for pitch ramp experiments

$$r(t) = \dot{\alpha}\frac{b}{U} \tag{2.71}$$

where $\dot{\alpha}$ is the constant pitch velocity. For sinusoidal motion, the pitch velocity oscillates so that the reduced pitch rate is a function of time, i.e.

$$r \quad = A\tfrac{\omega b}{U}\cos(\omega t) = Ak\cos(\omega t) \tag{2.72}$$

Sheng et al [33], [35] defined an equivalent (or maximum) reduced pitch rate as

$$r^{'} = Ak \tag{2.73}$$

They plotted graphs of the variation of the dynamic stall angle, α_{ds}, against r' and derived a bilinear relationship between these two quantities. The alternative proposed in the present work is to relate the dynamic stall angle to the instantaneous reduced pitch rate, as given by equation 2.71. The procedure is the following:

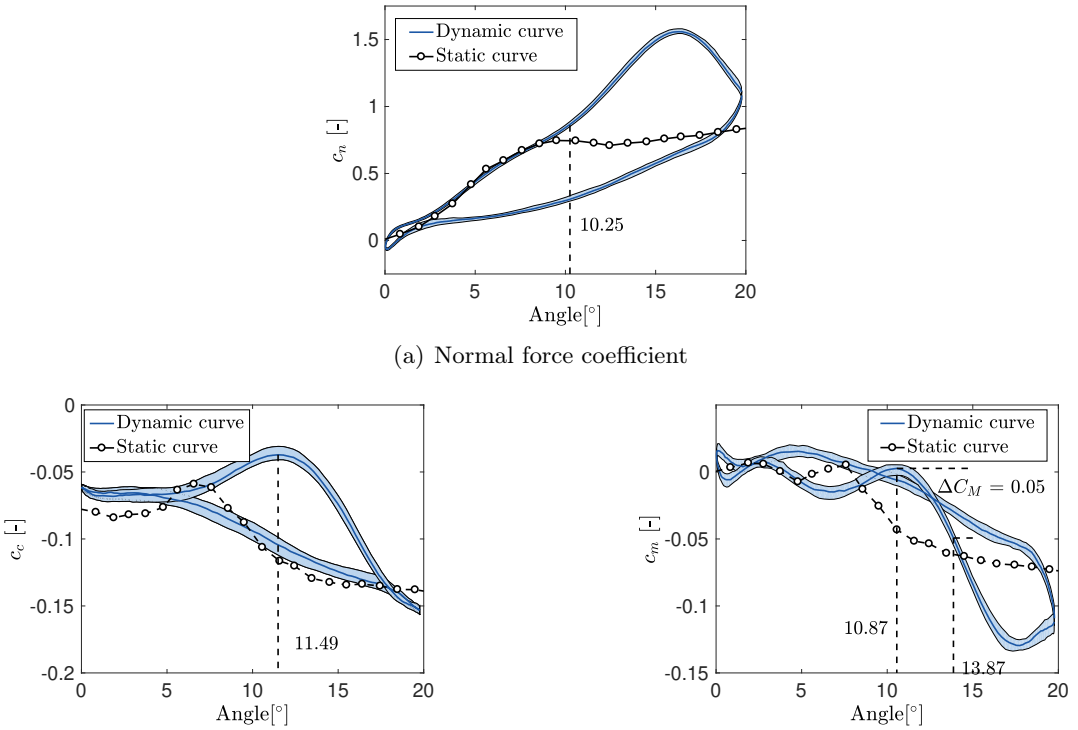

(a) Normal force coefficient

(b) Chordwise force coefficent

(c) Pitching moment coefficient

FIGURE 2.11: Aerodynamic loads for a NACA0012 oscillating with amplitude $A = 10°$, frequency $f = 5$ Hz and mean angle $A_0 = 10°$ and Reynolds number $Re \simeq 1.8 \times 10^4$.

1. For a particular choice of airfoil, amplitude and frequency, plot $c_c(t)$ against $\alpha(t)$ and identify the point where $c_c(t)$ is a maximum.

2. Evaluate the time at which the maximum value of $c_c(t)$ occurs, t_{ds}, and the corresponding pitch angle $\alpha_{ds} = \alpha(t_{ds})$, pitch velocity $\dot{\alpha}_{ds} = \dot{\alpha}(t_{ds})$ and reduced pitch rate $r(t_{ds})$.

3. Plot α_{ds} against $r(t_{ds})$.

4. Choose a test with different amplitude and frequency values and repeat from step 1.

Figure 2.12 compares the results obtained from plotting α_{ds} against r' and $r(t_{ds})$ for the NACA 0012 airfoil. At low dynamic stall angles the two plots are nearly identical but, for the highest stall angles, there is a difference of up to 0.005 between r' and $r(t_{ds})$. The advantage of plotting α_{ds} against $r(t_{ds})$ rather than r' is that the pitch rate is calculated from instantaneous values and therefore applies to any general type of motion, not just sinusoidal oscillations. This characteristic is particularly useful when one would use $\alpha_{ds}(r)$ to model the aeroelastic responses of airfoils at high angles of attack, which are generally not sinusoidal. During such a response, if the flow is initially attached, dynamic stall will occur when $\alpha(t)$ and $r(t)$ are such that $\alpha(t) = \alpha_{ds}(r(t))$ and $\alpha(t)\dot{\alpha}(t) > 0$.

As mentioned earlier, Sheng and Galbraith [33] derived a bilinear relationship between dynamic stall angle and reduced pitch rate, as shown in figure 2.13(a). The figure plots the dynamic stall angles obtained by Sheng and Galbraith for the NACA

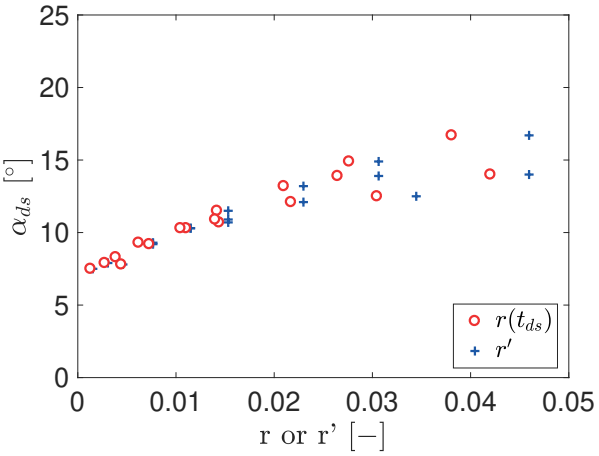

FIGURE 2.12: Comparison between equivalent reduced pitch rate and reduced pitch rate with angle of dynamic stall onset for a NACA0012

0012 undergoing pitch ramp up tests at a Reynolds number of 1.5×10^6, along with the data measured in chapter 3 for the same airfoil, against r. The relationship between dynamic stall onset angle and reduced pitch rate can indeed be represented as bilinear, with the break between the two linear regions occurring around $r = 0.01$. The dynamic stall angles identified at $Re \simeq 1.8 \times 10^4$ are all much lower than the ones obtained by Sheng and Galbraith due to the much more laminar nature of the boundary layer at this low Reynolds number.

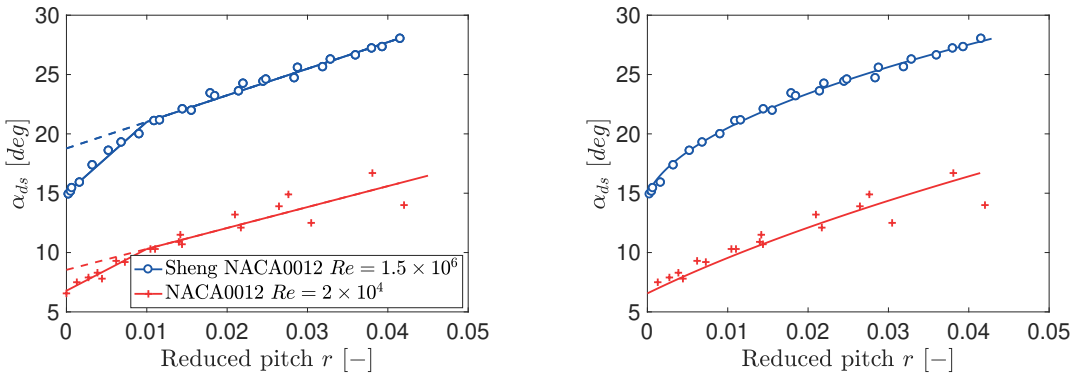

(a) Bilinear representation

(b) Continuous representation

FIGURE 2.13: Comparison of two curve fitting methods for the dynamic stall onset angle applied to NACA0012 at high and low Reynolds.

The bilinear model used by Sheng and Galbraith is not the only possible representation of the $\alpha_{ds}(r)$ relationship. Figure 2.13(b) shows that the same data can also be represented by a continuous function, in this case a square root of the form

$$\alpha_{ds}(r) = \frac{-b_{ds} + \sqrt{b_{ds}^2 - 4a_{ds}(c_{ds} - r)}}{2a_{ds}} \tag{2.74}$$

where a_{ds}, b_{ds}, c_{ds} are coefficients to be evaluated by a curve fit and α_{ds} is the angle of dynamic stall onset in degrees. Again, the advantages of using a continuous model for $\alpha_{ds}(r)$ become evident when modelling general motions that are not pitch ramps or sinusoidal oscillations, in particular aeroelastic responses. The absence of a discontinuity makes the time integration of the equations of motion simpler and less prone to numerical instabilities.

Dynamic stall and stall delay

The functions $s_s(\alpha)$ and $g_s(\alpha)$ only apply to static stall and so do the normal and pitching moment coefficients of equations 2.63 and 2.80. During pitching and plunging motion, the positions of the separation point and centre of pressure must be calculated as functions of the effective angle of attack of equation 2.51. Furthermore, as mentioned earlier, dynamic stall occurs at instantaneous pitch angles higher than those at which static stall occurs, due to the stall delay effect. As for the standard Leishman-Beddoes model, the stall delay is representend by applying a time lag to the instantaneous separation point, such that

$$\dot{s}' = \frac{U}{b}\frac{s_s(\alpha_e) - s'}{T_a}$$

where s' is the lagged separation point and T_a is the time lag.

For the standard LB model, the position of the center of pressure g is computed as a function of the lagged separation point $g_s(s^{'})$. In the present modified approach, the center of pressure displacement is computed as a function of the angle of attack instead. A lagged equivalent angle $\alpha^{'}$ is introduced such that

$$\dot{\alpha}' = \frac{U}{b}\frac{\alpha_e - \alpha'}{T_a}$$

Hence, the position of the center of pressure is $g_s(\alpha^{'})$.

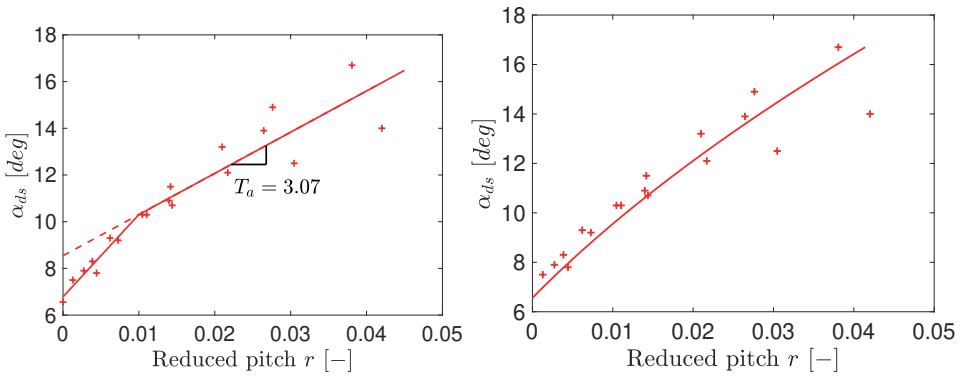

(a) Sheng method (b) Continuous method

FIGURE 2.14: Two methods used to compute time lag T_a for a NACA0012 at Reynolds $\simeq 1.8 \times 10^4$

Sheng et al. [34] defined the time lag T_a as the slope of the second straight line fitting the dynamic stall onset data, as shown in figure 2.14(a). As the present modelling of $\alpha_{ds}(r)$ is based on a square root curve fit, the definition of T_a is generalized

as

$$T_a(r) = \frac{d\alpha_{ds}}{dr} = \frac{1}{\sqrt{b_{ds}^2 - 4a_{ds}\left(c_{ds} - r\right)}} \frac{2\pi}{180} \tag{2.75}$$

Leading edge vortex

A vortex is created at the leading edge and starts to shed over the airfoil when the following conditions are met

$$\alpha_e \geq \alpha_{ds}(r) \tag{2.76}$$

$$\dot{\alpha}_e \alpha_e \geq 0 \tag{2.77}$$

Hence, the shedding of the vortex occurs during the upstroke and is related to the onset of dynamic stall. As discussed in section 2.1.4, once the vortex starts to shed, a non dimensional time variable

$$t_v = (t - t_0)\frac{V}{b} \tag{2.78}$$

is defined to keep track of the position of the vortex over the airfoil, where t is the current time and t_0 is the last time at which the stall onset criterion was met. The vortex clears the trailing edge when $t_v = t_{vl}$, the total time it takes for the vortex to travel over the entire surface of the airfoil. A non-dimensional version of t_{vl} is given by

$$T_{vl} = \frac{U}{b} t_{vl}$$

Estimation of T_{vl}

The parameter T_{vl} represents the time taken by the vortex to shed over the airfoil. It can be estimated with these different experimental methods :

- Time-resolved particle image velocimetry (PIV) to identify the vortex and its motion;
- Unsteady pressure data to identify the vortex pressure effects along the chord;
- Infer the position of the vortex from the measured unsteady aerodynamic load responses.

In the current work, only the last method can be used as there is no PIV or pressure data available for the test cases from sections 3.

The time taken by the vortex to shed over the airfoil can be obtained from two time instances:

- The dynamic stall onset time, computed in section 2.2.3.
- The time when the normal load is maximum, assumed to be the time when the vortex reaches the trailing edge of the airfoil.

These two time instances are shown in the normal force plot of figure 2.15(a) and in the $\alpha(t)$ plot of 2.15(b). Estimating T_{vl} for all the test cases and plotting it against instantaneous reduced pitch frequency leads to figure 3.8. It can be seen that T_{vl} can be curve-fitted as a continuous hyperbolic function of r. Plotting $1/T_{vl}$ against

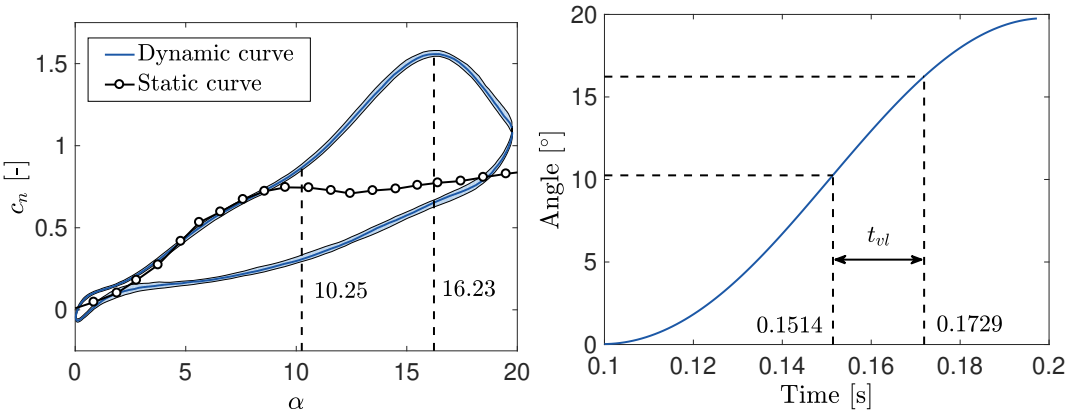

(a) Normal force coefficient versus angle of attack (b) angle of attack versus time

FIGURE 2.15: Determination of the time taken by the vortex to travel over the airfoil t_{vl}, for a NACA0012 airfoil and Reynolds number $Re \simeq 1.8 \times 10^4$.

r for the NACA0012 (figure 2.16(b)) results in a square-root behaviour, so that a reasonable choice for the curve fit is

$$T_{vl} = \frac{2a_{T_{vl}}}{-b_{T_{vl}} + \sqrt{b_{T_{vl}}^2 - 4a_{T_{vl}}(c_{T_{vl}} - r)}}$$

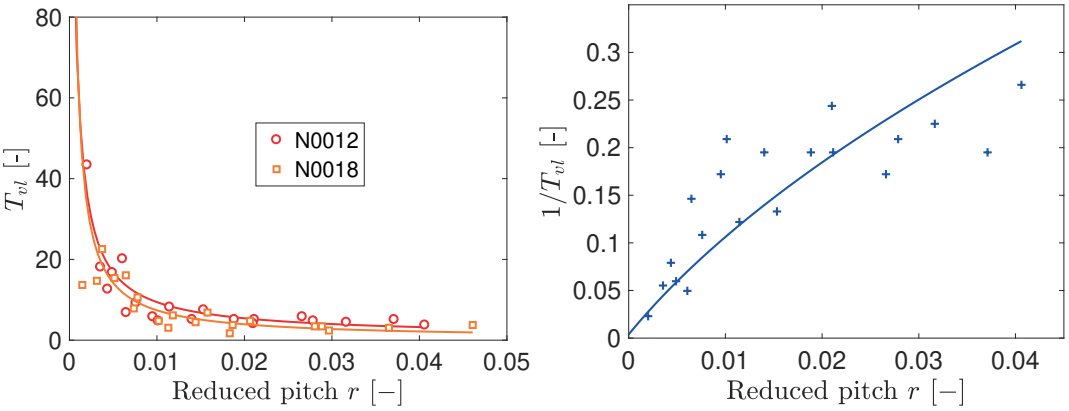

(a) T_{vl} vs r (b) $1/T_{vl}$ vs r

FIGURE 2.16: Variation of T_{vl} with r for the two NACA wings (left), $1/T_{vl}$ vs r for the NACA 0012 (right).

Looking at figure 3.8, T_{vl} increases significantly for very low reduced pitch rates. In their original paper [3], Leishman and Beddoes simply stated that this parameter should be constant for a given Mach number and did not study its variation with reduced pitch rate. This phenomenon is perhaps linked to a shielding effect of the airfoil as discussed by Choudhry et al. [65] in the case of ramp tests with the airfoil stopping at the end of the ramp motion.

2.2.4 Unsteady flow module

This module calculates the total aerodynamic loads applied on the wing section. It assembles the loads due to the attached flow, the trailing edge separation and the vortex shedding.

Loads associated with trailing edge separation

As in the classical formulation of the LB model [3], the normal force due to the unsteady trailing edge separation process, c_n^f, can be estimated by means of a modified formulation of the Kirchhoff-Helmholtz relation. It is done by using the circulatory normal force computed by the attached flow module with the lagged static flow separation location $s^{'}$, i.e.

$$c_n^f = c_n^c \left(\frac{1+\sqrt{s'}}{2} \right)^2 \tag{2.79}$$

The associated pitching moment coefficient, c_m^f, is then obtained using the separated c_n^c, an expression for the variation of the centre of pressure with respect to the delayed angle of attack $\alpha^{'}$ and the moment induced by the wake, so that

$$c_m^f = \left[\left(\frac{1}{2} \left(\frac{1}{2} + a \right) - g_s(\alpha') \right) c_n^c - \frac{1}{2} \left(\frac{1}{2} - a \right) \frac{\pi b}{U} \dot{\alpha} \right] \left(\frac{1+\sqrt{s'}}{2} \right)^2 + c_{m_{1/4}}^0 \tag{2.80}$$

Circulation change

Leishman [57] added a vortex-induced normal lift coefficient c_n^v to represent the effects of the vortex on the total lift. As explained in section 2.1.4, it is an accumulation of vorticity that is lost in the wake when vortex shedding occurs. This vortex lift is represented by the following differential equation

$$\dot{c_n^v} = \dot{c_v} - \frac{U}{b} \frac{c_n^v}{T_v} \tag{2.81}$$

In the modified model, the interpretation of the vortex-induced normal lift coefficient c_n^v is adapted. It is not directly linked to vortex shedding effects but mostly represents the delay in the change of circulation around the airfoil for abrupt motion. This lagged change of circulation is estimated from the difference between the attached and separated lift, i.e.

$$c_v = c_n^c - c_n^f = c_n^c \left(1 - \left(\frac{1+\sqrt{s'}}{2} \right)^2 \right) \tag{2.82}$$

This change of circulation is also allowed to decay exponentially with a non dimensional time constant T_v. By combining the circulation buildup and decay one gets an added normal force that can be computed using equation 2.81 This force represents unsteady effects on the circulation caused by high pitch rates; c_n^v decreases with pitch rate, becoming equal to zero at static conditions. In the present, work, the decay time of this circulation was chosen equal to the dynamic stall time delay, i.e. $T_v = T_a$ to reduced the number of free parameters.

The normal force c_n^v is linked to the circulation around the airfoil and applied to the center of pressure of the airfoil. Therefore, the pitching moment coefficient due to

the excess accumulation of circulation in the vicinity of the airfoil is given by

$$c_m^v = \left(\frac{1}{2}\left(\frac{1}{2}+a\right) - g_s(\alpha')\right) c_n^v \tag{2.83}$$

Vortex shedding effects

The aerodynamic load overshoot caused by the motion of the vortex over the airfoil can be computed following Sheng's [35] assumption that this overshoot is proportional to the difference between the lagged $s(\alpha^{'})$ and non-lagged $s(\alpha_e)$ separation points, i.e.

$$\Delta c_n^v = B_1\left(s^{'} - s_s(\alpha_e)\right) V_x \tag{2.84}$$

$$\Delta c_m^v = -B_2 \Delta c_n^v \tag{2.85}$$

where B_1 and B_2 are parameters controlling the amplitude of the overshoot and V_x is a modified shape function proposed in this paper,

$$V_x = \left|\sin\left(\tfrac{\pi t_v}{2T_{vl}}\right)\right| \tag{2.86}$$

$$\tag{2.87}$$

The shape function is periodic in order to represent the possibility of multiple vortex shedding and its effects on the aerodynamic loads. The coefficients B_1 and B_2 are assumed to be independent of the pitch rate and estimated to best fit the available data.

2.2.5 Complete equations

Finally, the total unsteady aerodynamic loads can be calculated. First the state space variables are computed from the following equations

$$\dot{\mathbf{z}} = \mathbf{W}\mathbf{z} + \mathbf{F}\mathbf{q}$$

$$\dot{s^{'}} = \frac{V}{b}\frac{s_s(\alpha_e) - s^{'}}{T_a}$$

$$\dot{\alpha^{'}} = \frac{V}{b}\frac{\alpha_e - \alpha^{'}}{T_a}$$

$$\dot{c_n^v} = \dot{c_v} - \frac{V}{b}\frac{c_n^v}{T_a}$$

Then, the aerodynamic loads are defined by the relations

$$
\begin{aligned}
c_n^I &= \frac{\pi b}{U^2}\left(\ddot{h} - a\,b\,\ddot{\alpha}\right) + \frac{\pi b}{U}\dot{\alpha} \\
c_m^I &= \frac{\pi b}{2U^2}\left[a\ddot{h} - \left(a^2 + \frac{1}{8}\right)\ddot{\alpha}\right] \\
c_n^c &= \mathbf{C}\dot{\mathbf{q}} + \mathbf{D}\mathbf{q} + \mathbf{E}\mathbf{w} + r\dot{\Phi}(t) \\
c_n^f &= c_n^c\left(\frac{1+\sqrt{s'}}{2}\right)^2 \\
c_m^f &= \left[\left(\frac{1}{2}\left(\frac{1}{2}+a\right) - g_s(\alpha')\right)c_n^c - \frac{1}{2}\left(\frac{1}{2}-a\right)\frac{\pi b}{U}\dot{\alpha}\right]\left(\frac{1+\sqrt{s'}}{2}\right)^2 + c_{m_{1/4}}^0 \\
c_m^v &= \left(\frac{1}{2}\left(\frac{1}{2}+a\right) - g_s(\alpha')\right)c_n^v \\
\Delta c_n^v &= B_1\left(s' - s_s(\alpha_e)\right)V_x \\
\Delta c_m^v &= -B_2\Delta c_n^v
\end{aligned}
$$

Finally, the total loads are

$$
\begin{aligned}
c_n &= c_n^I + c_n^f + c_n^v + \Delta c_n^v \\
c_m &= c_m^I + c_m^f + c_m^v + \Delta c_m^v
\end{aligned}
$$

From here, one can compare the equations of this modified Leishman-Beddoes model equations with those of the classical model given in section 2.1.6.

Chapter 3

Application of the modified LB model

In this chapter, the predictions obtained from the modified LB model are compared to those obtained from the original LB and to experimental measurements. The unsteady loads during dynamic stall are measured on three chosen wing sections, a flat plate, a NACA0012, a NACA0018.

3.1 Experimental setup

The experiments were performed in a closed-loop low-speed wind tunnel at LadHyX, which has a rectangular test-section 0.26 m wide and 0.24 m high. Tests have been performed at a mean flow velocity $U \simeq 7.5\,m/s$ and $U \simeq 7.25\,m/s$, for which the non-uniformity in the test section is less than 1% and the turbulence intensity is close to 1.2%.

3.1.1 Three wing models

Three wing sections were chosen for the experiments, a flat plate, a NACA0012 and a NACA0018. For intermediate Reynolds numbers, $Re \simeq 10^6$, these wing sections are supposed to exhibit three distinct stall behaviours [9], a smooth thin-airfoil stall for the flat plate, a sharp leading-edge stall for the NACA0012 and a moderate trailing-edge stall for the NACA0018. At the low Reynolds number range of the present study, $Re \simeq 10^4$, these stall classifications could be still relevant, even if both the NACA models are also affected by a laminar separation bubble process at low angles of attack. This will be discussed further in section 3.3.

The flat plate model was made from a carbon fiber plate of span 130 mm, chord 35 mm and thickness 1.5 mm. This model featured a rectangular cross section with a thickness-to-chord ratio of 4.3%. The leading and trailing edges were not rounded off, so that they remained sharp. The NACA0012 and NACA0018 models of span $l = 130$ mm and chord $c = 38$ mm were produced by means of 3D printing. Hand sanding was used to smooth the residual roughness caused by the 3D printing process. The three wing models are shown in figure 3.1 and their dimensions are summarised in table 3.1. Each model was mounted horizontally in the test section. A small distance from the wall was allowed at one end to limit boundary layer perturbations. An end plate was installed at the other extremity of the model to suppress three-dimensional flow effects.

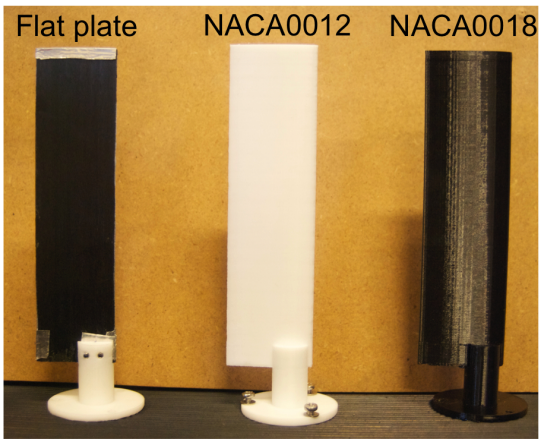

FIGURE 3.1: Side view of the tested wings.

Wing	Chord [mm]	Span [mm]	Reynolds
Flat plate	35	130	17500
NACA0012	38	130	18400
NACA0018	38	130	18400

TABLE 3.1: Wings dimensions and Reynolds numbers

3.1.2 Measurement setup

The harmonic pitching motion was directly driven by a brushless motor (Maxon flat motor EC 60, 100W). The motor was controlled by a digital position controller (EPOS2 24/5) using Proportional/Integral/Derivative (PID) control. The unsteady loads acting on the wings were measured by a six-axis force/torque sensor (ATI Nano43) mounted between the motor and the models. A 24-bit data acquisition system furnished by Muller- BBM was used to receive the analog transducer signals and convert them to force and moment using the calibration matrix provided by ATI. Figure 3.2 shows the mounting of the motor, force/torque sensor and wing (from left to right respectively) in the wind tunnel. The motion imposed by the motor was sinusoidal of the form

$$\alpha(t) = A_0 + A \sin 2\pi f t$$

where $\alpha(t)$ is the instantaneous pitch angle, A_0 the mean pitch value, A the pitch amplitude and f the frequency.

A laser displacement sensor (Keyence LB-11W) was used to measure the instantaneous angle of attack simultaneously with the unsteady forces and moments. All data were recorded with a sampling rate of 1024 kHz and the acquisition time was equal to or higher than 50 times the period of the harmonic pitching motion.

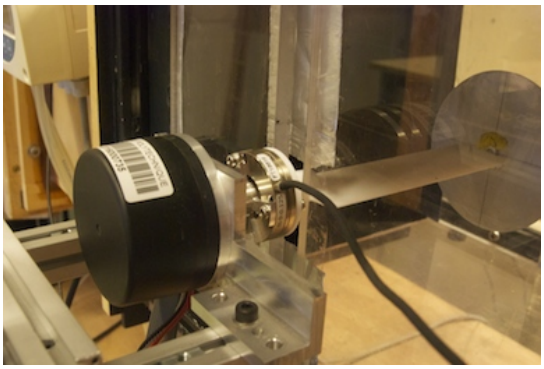

FIGURE 3.2: NACA0012 in mounted configuration inside the wind tunnel.

3.2 Data processing

The loads of interest were the normal force, N, chordwise force, C and pitching moment, M, as well as their coefficient forms

$$c_n = \frac{N}{1/2\rho U^2 S},\ c_c = \frac{C}{1/2\rho U^2 S},\ c_m = \frac{M}{1/2\rho U^2 S c}$$

where ρ is the air density, U the wind tunnel airspeed and $S = c \times l$ the wing surface. Direct unsteady load measurements on moving models are subjected to two types of error. The first source is the natural vibration of the wing and motor supports, which in this case were designed to be as light and as stiff as possible. The second source of error involves the combination of static weight and dynamic inertia effects. Dynamic tare subtraction and low-pass filtering were applied to the data during post-processing in order to remove these errors. Dynamic tare was systematically identified at wind-off conditions prior to each dynamic test for a given amplitude and frequency of motion. A brick-wall low-pass filter was used to filter the dynamic loops at frequencies above 40 Hz for the flat plate, NACA0012 and NACA0018. This cut-off frequency eliminated the first resonant frequency of the full setup, while it preserved up to the 7th harmonic of the unsteady aerodynamic load for frequencies up to 5 Hz, i.e. a reduced pulsation close 0.08 in our experiments (see Tables 3.2 and 3.3). Nevertheless, some of the higher harmonics were lost to the filter at the higher motion frequencies, 7.5 and 10 Hz.

The complete unsteady measurement and data reduction procedure is demonstrated for the normal force measurement in Figure 3.3 for a pitching motion of amplitude $A = 15°$, frequency $f = 2.5$ Hz and wind tunnel velocity $U = 7$ m/s. The reduced frequency is defined as

$$k = \frac{\omega b}{U} \tag{3.1}$$

where $\omega = 2\pi f$ and $b = c/2$ is the half-chord. For the example of figure 3.3, $k = 0.045$. It must be noted that the wind-off load measurements included added mass aerodynamic effects but their amplitude was negligible at such low reduced frequencies. Therefore, it was assumed that structural inertial loads constituted the only measurable load component at $U = 0$ m/s. The procedure was the following:

1. Simultaneous measurement of the pitching motion, normal force (figure 3.3(b)), chordwise force and pitching moment at wind-off conditions.

2. Low pass filtering of the wind-off normal force (figure 3.3(c)), chordwise force and pitching moment.

3. Calculation of the statistics of the wind-off normal force (figure 3.3(d)), chordwise force and moment over at least 50 consecutive cycles of motion.

4. Simultaneous measurement of the pitching motion (figure 3.3(a)), normal force (figure 3.3(e)), chordwise force and pitching moment at wind-on conditions.

5. Low pass filtering of the wind-on normal force (figure 3.3(f)), chordwise force and pitching moment.

6. Calculation of the statistics of the wind-on normal force (figure 3.3(g)), chordwise force and moment over at least 50 consecutive cycles of motion.

7. Subtraction of the wind-off (dynamic tare) forces and moment from the wind-on loads (Figure 3.3(h)).

8. Calculation of the resulting dynamic loops for the normal (figure 3.3(i)), chordwise and moment coefficients.

The statistics used to show the results are the median and the interquartile region defined as the area between the first and third quartiles. At each considered time point on the cycles :

- The first quartile is the value below which lie the first lower 25% of all measured points at this specific time instance of the cycle.
- The median is the value below which lie the first lower 50% of all measured points at this specific time instance of the cycle.
- The third quartile is the value below which lie the first lower 75% of all measured points at this specific time instance of the cycle.

3.3 Static stall experiments

A first set of experiments was carried out in order to measure the aerodynamic forces acting on the wings at static conditions. The measurements concerned the normal and chordwise force coefficients and the pitching moment coefficient at angles of attack, ranging from 0° to 45°. The Reynolds number was constant at $Re \simeq 1.8 \times 10^4$. For each fixed angle of attack, the average values of the load coefficients were calculated from 10 seconds of measurements acquired at a sampling frequency of 1024 Hz.

Figure 3.4 plots the variation of the normal force and pitching moment coefficients with angle of attack. Measured data are plotted along with the results obtained using semi-empirical reconstruction models that were discussed in detail in section 2.2.2. As mentioned earlier, the three airfoil shapes were chosen because they have different static stall mechanisms at intermediate and high Reynolds numbers: smooth thin airfoil stall (Flate plate), sharp leading edge stall (NACA0012) and moderate trailing edge stall (NACA0018). The thin airfoil stall behaviour is confirmed for the flat plate which exhibits a short linear region followed by a smooth stall behaviours, i.e. the lift smoothly moves away from the linear evolution, without any local maxima or minima for angles up to 40°. The NACA 0012 model exhibits a sharper stall behaviour for which a local maximum in lift is noticeable close to $\alpha = 9°$. Broeren [11] showed

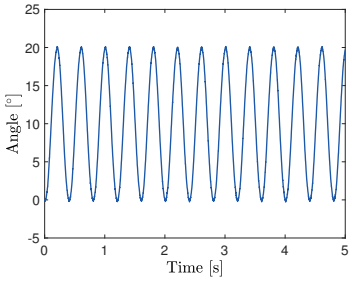

(a) Measured angle of attack

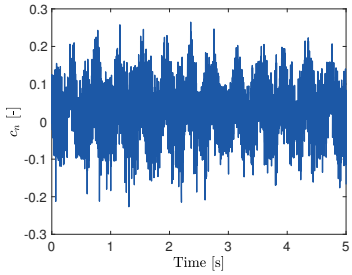

(b) Wind-off unfiltered normal force

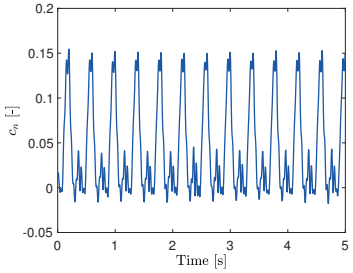

(c) Wind-off filtered normal force

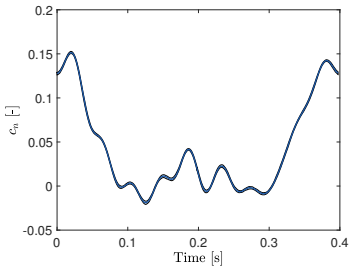

(d) Wind-off cycle median with interquartile envelope

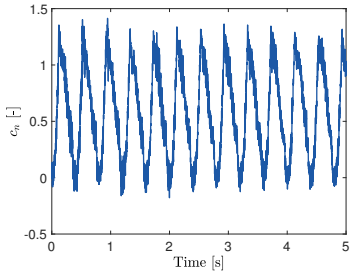

(e) Wind-on unfiltered normal force

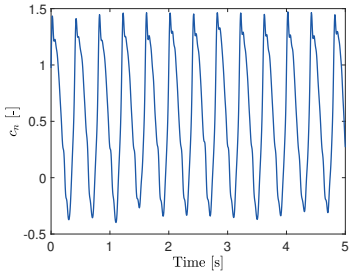

(f) Wind-on filtered normal force

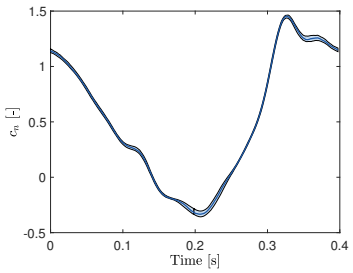

(g) Wind-on cycle median with interquartile envelope

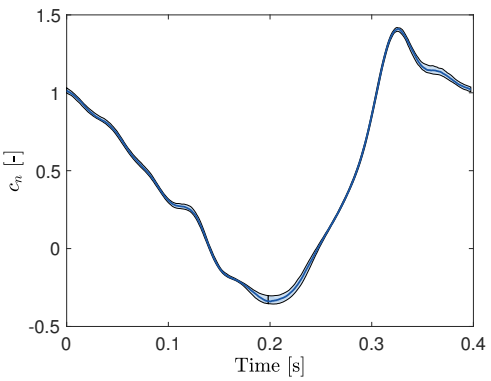

(h) Aerodynamic normal force versus time

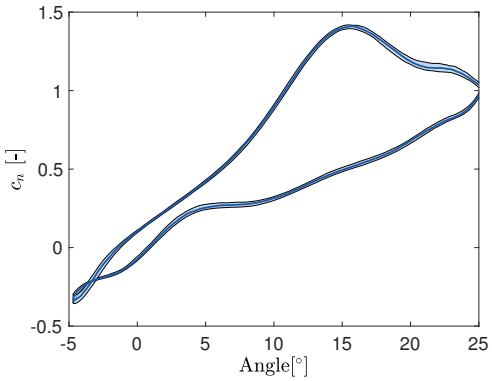

(i) Aerodynamic normal force versus instantaneous pitch angle

FIGURE 3.3: Summary of the unsteady measurement process for a NACA0012 airfoil with a pitching motion of amplitude 15°, frequency $f = 2.5$ Hz, wind velocity $U = 7.25$ m/s and reduced frequency $k = 0.043$.

that a leading edge stall mechanism is characterized by an abrupt and sudden drop in normal force coefficient; such a drop cannot be seen in figure 3.4(c) and in the absence of pressure measurements, it is not possible to confirm wether the NACA 0012 experienced a leading edge stall at the low Reynolds number tested here. The NACA 0018 exhibits a smoother stall behavior (compared with the NACA 0012), which also occurs at a rather low angle of attack, close to $\alpha = 5.5°$. Again it is difficult to say wether the stall mechanism is different between the NACA 0018 and NACA 0012, but for both airfoils a laminar separation bubble process occurs at low angles of attack, which may have an effect on the stall mechanisms.

Indeed, it is obvious that the normal force for the two NACA airfoils is not linear at low angles of attack.This phenomenon was observed by Lutz et al [66] for the NACA 0009 airfoil; they attributed it to a laminar separation bubble that is formed near the leading edge at low angles of attack. This nonlinearity is ignored in the present work, as discussed in section 2.2.2.

3.4 Dynamic stall experiments

3.4.1 Prescribed pitch motion

The frequencies chosen for the pitching oscillations were $f = [1, 2.5, 5, 7.5, 10]$ Hz. The corresponding ranges of reduced frequency are $k = [0.015, 0.15]$ for the flat plate and $k = [0.016, 0.16]$ for the two NACA wings. The mean pitch angle was always set to $A_0 = 10°$ and the oscillation amplitude to $A = [5, 10, 15, 20]°$. As a consequence, the maximum 2D wind tunnel blockage coefficient, defined as $c\sin(30°)/Hv$, where H_v is the height of the test section, was always less than 8.4%. Therefore, no blockage corrections were necessary throughout the present study. Higher frequency and amplitude combinations were not possible due to motor limitations. All tests were carried out at a a mean flow velocity of $U \simeq 7.5m/s$ for the flat plate and $U \simeq 7.25m/s$ for the two NACA wings.

The reduced frequency and equivalent reduced pitch rate, previously described in equations 3.1 and 2.73, are tabulated in table 3.2 for the flat plate and 3.3 for the two NACA wings for the different dynamic stall tests carried out in the context of the present work.

$f\,[hz]$	1	2.5	5	7.5	10
$k\,[-]$	0.015	0.037	0.073	0.11	0.15
$A = 5$	0.0013	0.0033	0.0066	0.099	0.0132
$A = 10$	0.0026	0.0066	0.0132	0.0199	0.0265
$A = 15$	0.04	0.099	0.0199	0.0298	0.0397
$A = 20$	0.0053	0.0132	0.0265	0.0397	0.0529

TABLE 3.2: Equivalent reduced pitch rate for the flat plate as a function of the frequency and amplitude of motion.

3.4.2 Dynamic stall onset criteria

The general dynamic stall onset criterion for the two NACAs has already been presented in section 2.2.3. Figure 3.5 plots the dynamic stall onset angle function $\alpha_{ds}(r)$

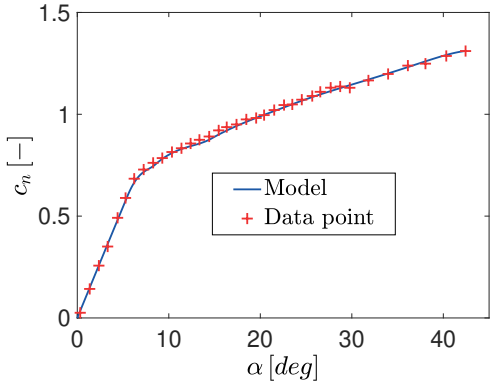

(a) Normal force coefficient for the flat plate

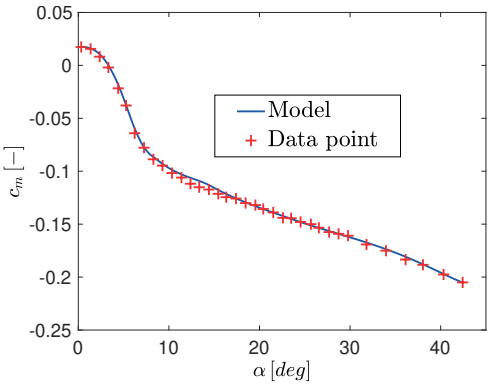

(b) Pitching moment coefficient for the flat plate

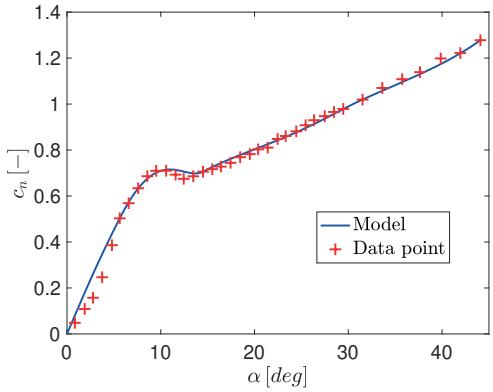

(c) Normal force coefficient for the NACA0012

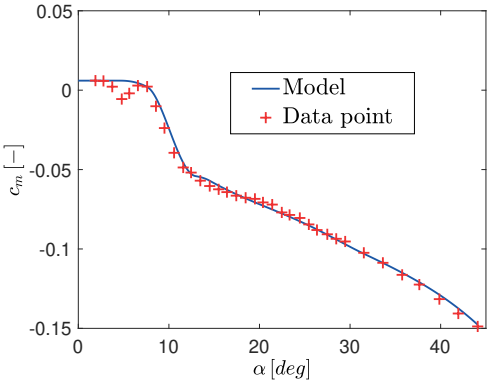

(d) Pitching moment coefficient for the NACA0012

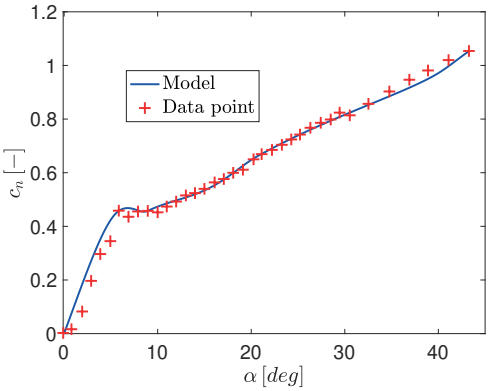

(e) Normal force coefficient for the NACA0018

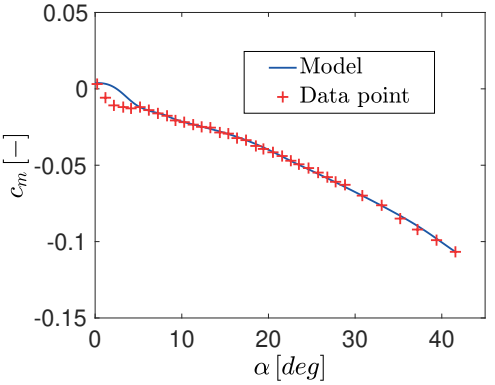

(f) Pitching moment coefficient for the NACA0018

FIGURE 3.4: Normal force c_n and pitching moment c_m coefficient variation with angle of attack from static tests

$f\,[hz]$	1	2.5	5	7.5	10
$k\,[-]$	0.016	0.041	0.082	0.12	0.16
$A = 5$	0.0015	0.0037	0.0073	0.011	0.0146
$A = 10$	0.0029	0.0073	0.0146	0.0219	0.0292
$A = 15$	0.044	0.011	0.0219	0.0329	0.0439
$A = 20$	0.0058	0.0146	0.0292	0.0439	0.0585

TABLE 3.3: Equivalent reduced pitch rate for the NACA 0012 and 0018 as a function of the frequency and amplitude of motion.

for the NACA0012 and NACA0018 airfoils, along with the square root curve fits. Table 3.4 gives the coefficient values a_{ds}, b_{ds} and c_{ds} used for the curve fit for each airfoil.

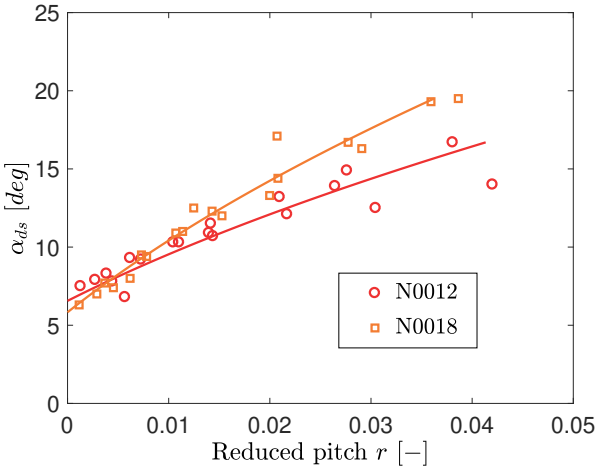

FIGURE 3.5: Dynamic stall onset angle variation with instantaneous reduced pitch rate for the NACA 0012 and 0018 airfoils.

3.4.3 Flat plate Dynamic stall onset

The chordwise force response, $c_c(t)$, for the flat plate did not exhibit a clear maximum, so that this criterion could not be used for determining the dynamic stall angle. A different criterion was used, based on observing the variation of the normal force coefficient variation with pitch angle, $c_n(\alpha)$, at both static and dynamic conditions. Figure 3.6(a) shows that the static normal force curve can be seen as an asymptote of two straight lines, one with a high slope before stall and one with a low slope after stall. A static stall angle can therefore be defined as the angle at which these two straight lines intersect. Figure 3.6(b) demonstrates that similar behaviour occurs during pitch oscillations. On the upstroke, $c_n(\alpha(t))$ can be seen as an asymptote of two straight lines. Consequently, the dynamic stall angle is defined as the angle α_{ds} at which these two lines intersect. The variation of the stall angle α_{ds} with instantaneous reduced pitch rate r for the flat plate is shown in figure 3.7. The function $\alpha_{ds}(r)$ is

curve-fitted using the square root representation of equation 2.74. Note that $\alpha_{ds}(r)$ curves upwards for the flat plate while it curves downwards for the NACA 0012 and 0018 airfoils (see figure 3.5).

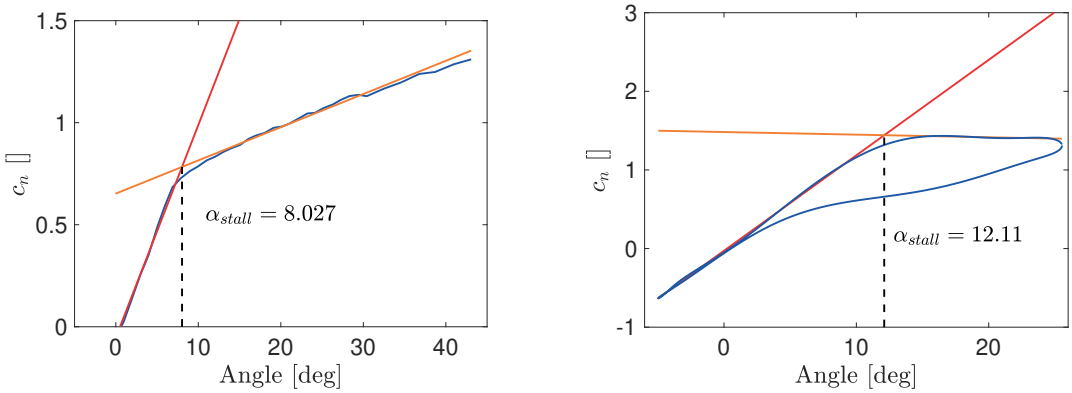

(a) Steady case (b) Unsteady case

FIGURE 3.6: Static and dynamic stall criterion for the flat plate.

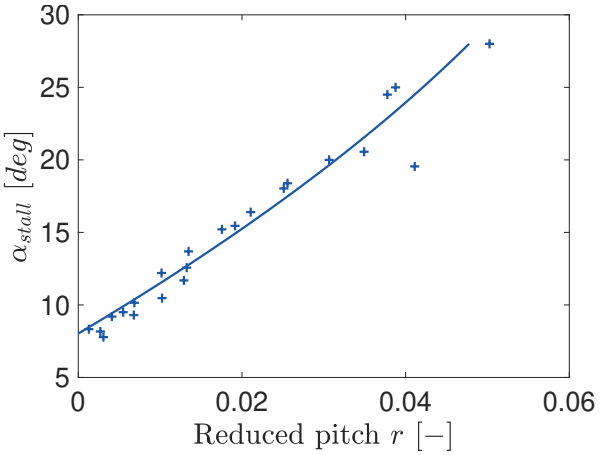

FIGURE 3.7: Stall angle variation with instantaneous reduced pitch rate for the flat plate.

The coefficient values for each airfoil are given in table 3.4

	N0012	N0018	Flat plate
a_{ds}	1.0053×10^{-4}	5.206×10^{-5}	-2.9713×10^{-5}
b_{ds}	0.0017	0.0013	0.0035
c_{ds}	−0.0157	−0.0095	−0.0259

TABLE 3.4: Curve fit coefficients of the dynamic stall onset angle for each airfoils

From the coefficients from table 3.4, one can compute the dynamic stall onset angle α_{ds} and the time lag T_a as

$$\alpha_{ds}(r) = \frac{-b_{ds} + \sqrt{b_{ds}^2 - 4a_{ds}\,(c_{ds} - r)}}{2a_{ds}} \tag{3.2}$$

$$T_a(r) = \frac{d\alpha_{ds}}{dr} = \frac{1}{\sqrt{b_{ds}^2 - 4a_{ds}\,(c_{ds} - r)}} \frac{2\pi}{180} \tag{3.3}$$

3.5 Vortex shedding

The computation of the time T_{vl} taken by the vortex to shed over the airfoil was described in section 2.2.3.

Figure 3.8, shows the variation of the vortex shedding time as a function of the reduced pitch r for the two NACA aifoils studied in this work.

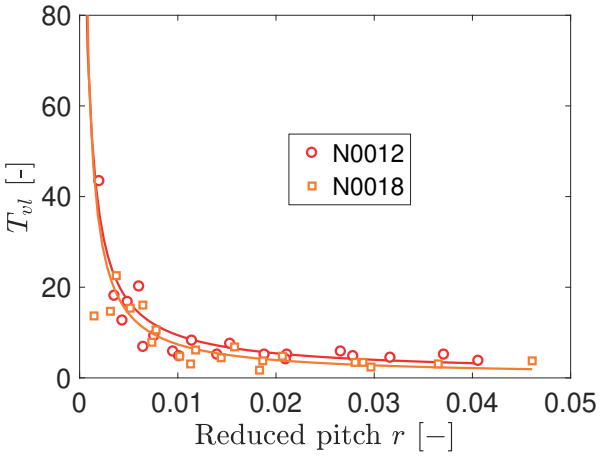

FIGURE 3.8: Variation of T_{vl} with r for the two NACA wings.

Table 3.5 gives the values of the curve fit coefficients $a_{T_{vl}}$, $b_{T_{vl}}$ and $c_{T_{vl}}$ for the two NACA airfoils studied in this work. The coefficients can be used to compute T_{vl} as follow

$$T_{vl} = \frac{2a_{T_{vl}}}{-b_{T_{vl}} + \sqrt{b_{T_{vl}}^2 - 4a_{T_{vl}}(c_{T_{vl}} - r)}}$$

	Flat Plate	N0012	N0018
a_{Tvl}	–	0.166	0.036
b_{Tvl}	–	0.0794	0.07
c_{Tvl}	–	-3.1128×10^{-4}	-1.2074×10^{-4}

TABLE 3.5: Vortex passage time curve fit coefficients for each airfoil

No coefficient are tabulated for the flat plate, since vortex shedding is assumed to not be present for this airfoil.

3.6 Validation of the modified Leishman-Beddoes model

3.6.1 Original Leishman-Beddoes

The results of the modified Leishman-Beddoes model presented in the present work are compared with experimental measurements and predictions from the original Leishman-Beddoes model [3]. The code used to compute the LB model comes from Dimitriadis [67]. The parameters used for the original Leishman-Beddoes model for each airfoil are presented in table 3.6. It should be noted that the parameter c_{n1} was set to ∞ for the flat plate in order to remove any vortex shedding in the Leishman-Beddoes model similarly to what was done for the modified LB model presented in this paper.

	Flat Plate	N0012	N0018
a_0	6.18	5.2	5.2
S_1	0.0705	0.0494	0.0494
S_2	0.0936	0.0635	0.0423
α_1°	7.89	8.5	5.8
K_0	−0.1475	0	0
K_1	−0.0027	−0.1125	−0.0719
K_2	0	0.0013	−0.0356
$c^0_{m_{1/4}}$	0.0174	0.006	0.006
c_{n1}	∞	0.5687	0.4585
T_p	1.7	1.7	1.7
T_f	8.2	8.8	8.2
T_v	4	8.8	4
T_{vl}	12	8.2	12

TABLE 3.6: Original Leishman-Beddoes parameters for each airfoil

3.6.2 Comparison

Given the large number of test cases, only three reduced pitch rates have been chosen for each airfoil in order to compare the predictions obtained from the modified Leishman-Beddoes model presented in this section (plain line), the original Leishman-Beddoes model [3] (dot dashed line) and the experimental results (dashed line) . Figures 3.9, 3.10 and 3.11 respectively show the comparison of the normal force and pitching moment coefficient for the flat plate, the NACA0012 and the NACA0018. Note that the case $f = 10\ hz$, $A = 20°$ was not shown for the NACA0018 because the experimental results were unreliable.

For the low reduced pitch rate there is good agreement between both models and the experimental results for the flat plate (see Figures 3.9(a) and 3.9(b)). For the NACA0012 and NACA0018 sections (see Figures 3.10(a), 3.10(b) and Figures 3.11(a), 3.11(a)), the modified Leishman-Beddoes model is in good agreement with the experiments and improves significantly the prediction of the normal force overshoot, nose down pitching moment and hysteresis effect, in comparison to the original LB Model.

Qualitatively, the agreement between both models and the experimental results deteriorates with increasing pitch rate. Nevertheless the modified Leishman-Beddoes model is still acceptable for intermediate pitch rates (see Figures 3.9(c), 3.9(d), 3.10(c), 3.10(d), 3.11(c), 3.11(d)). In particular, the dynamic loop shapes for both normal force and pitching moment obtained from the modified model better match the experiments. Nevertheless both models underestimate the normal force overshoot (see Figures 3.9(c), 3.10(c), 3.11(c)) and for both the NACA sections, the nose down pitching moment is overestimated with the original LB model and underestimated with the modified formulation (see Figures 3.9(d), 3.10(d), 3.11(d))).

Both model predictions become less accurate at the highest pitch rate. For the flat plate section the modified Leishman-Beddoes model gives better results than the original one for the normal force dynamic loop (Figures 3.9(e)), but the amount of hysteresis in the pitching moment is strongly overestimated. For the NACA sections both the models underestimate significantly the normal force overshoot (see Figures 3.10(e) and 3.11(e)), overestimate the pitching moment dynamic loop and, as for the intermediate pitch rate, the nose down pitching moment is overestimated with the original LB model and underestimated with the modified formulation (see Figures 3.10(f) and 3.11(f)).

Concerning the normal force overshoot for medium and high pitch rates, the modified model gives slightly better results than the original one. Nevertheless the model could be improved using B_1 and B_2 coefficients in equations 2.84 and 2.85, dependant on the pitch rate.

Concerning the pitching moment, the main issue for both models is to better capture the hysteretic effect for moderate and high pitch rates. This could be achieved with a better representation of the variation of the center of pressure position during the dynamic stall process. A better prediction of the nose down pitching moment could also be achieved with a more accurate identification of the T_{vl} nondimensional parameter.

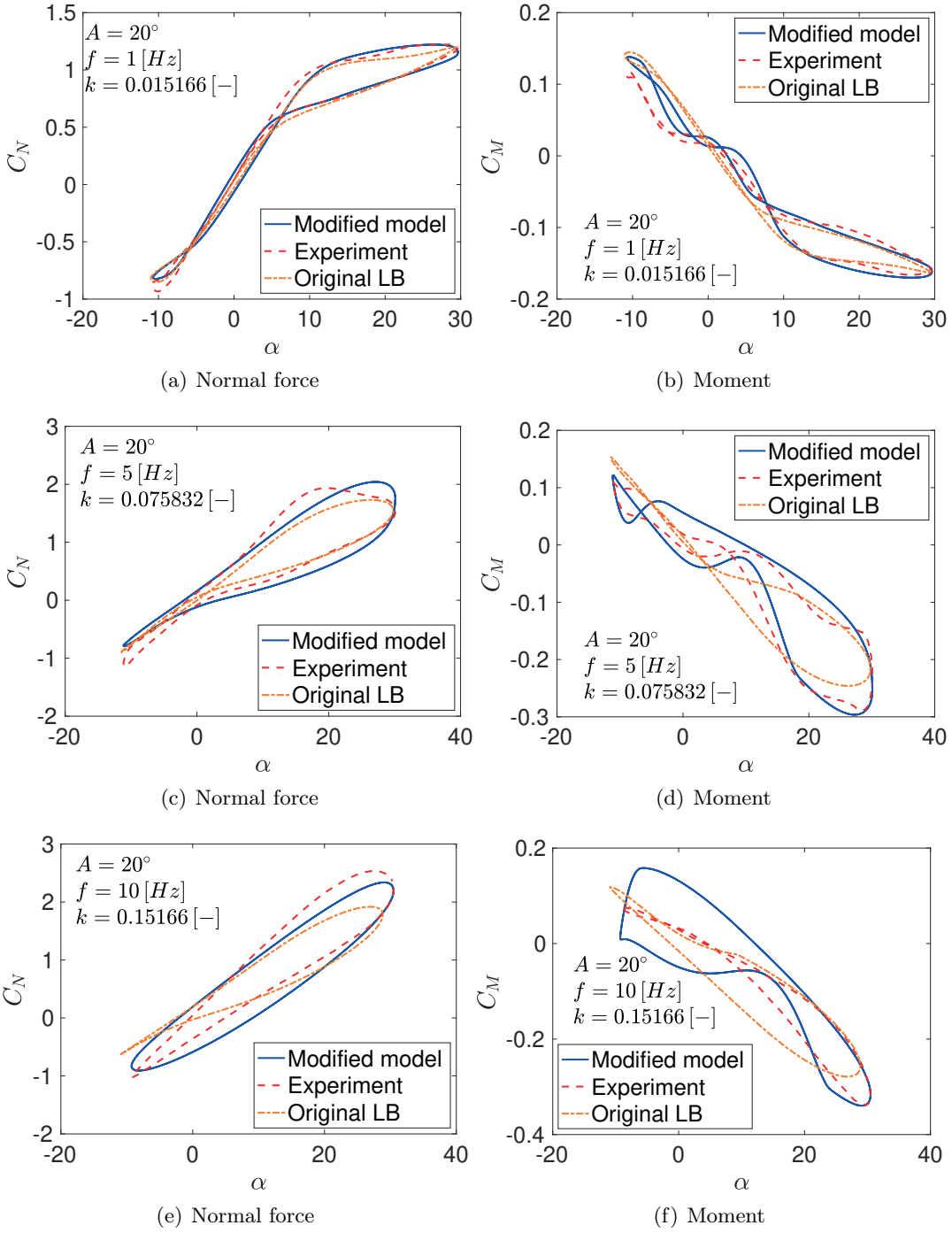

(a) Normal force (b) Moment

(c) Normal force (d) Moment

(e) Normal force (f) Moment

FIGURE 3.9: Comparison between model and experiment for the flat plate.

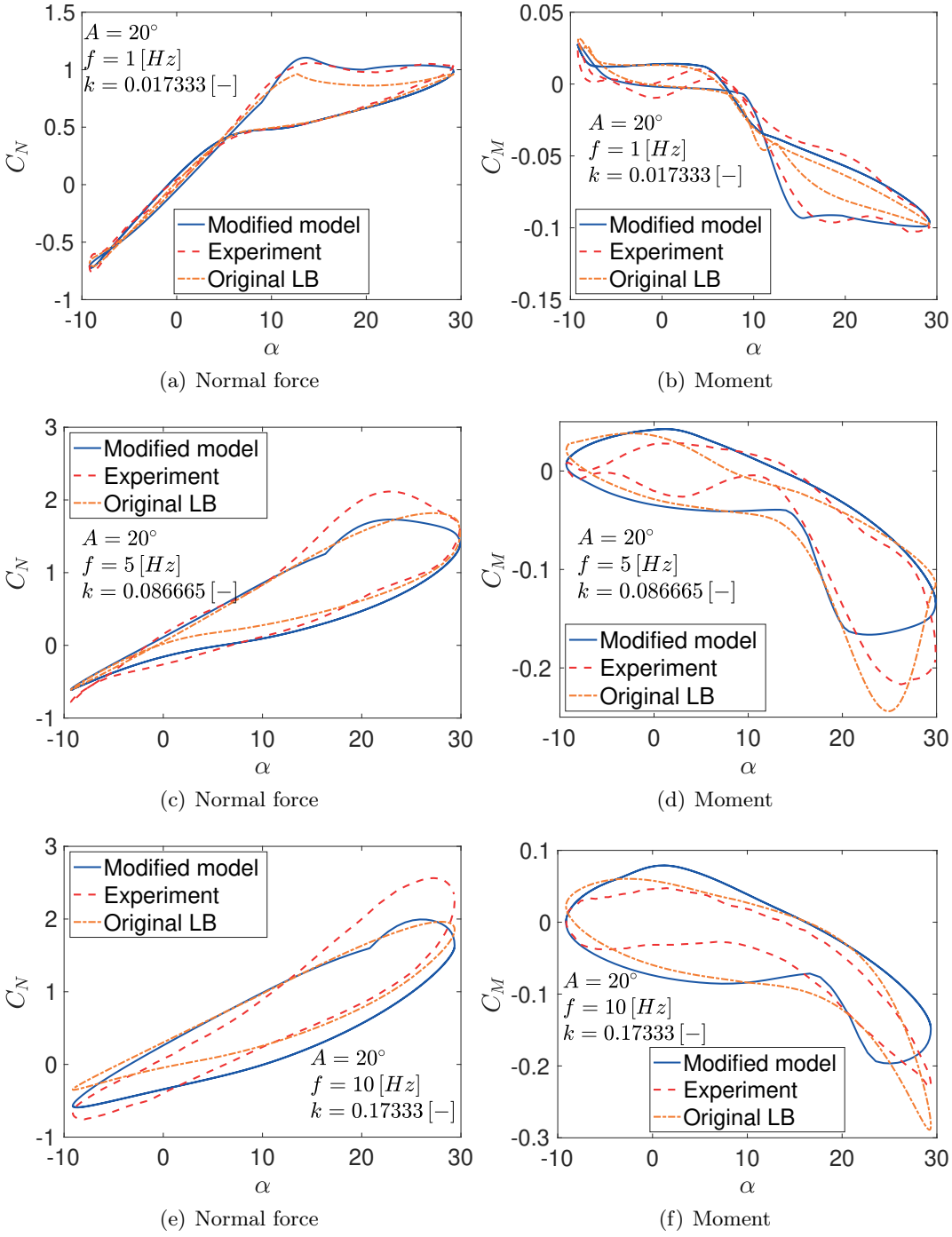

(a) Normal force (b) Moment

(c) Normal force (d) Moment

(e) Normal force (f) Moment

FIGURE 3.10: Comparison between model and experiment for the NACA0012.

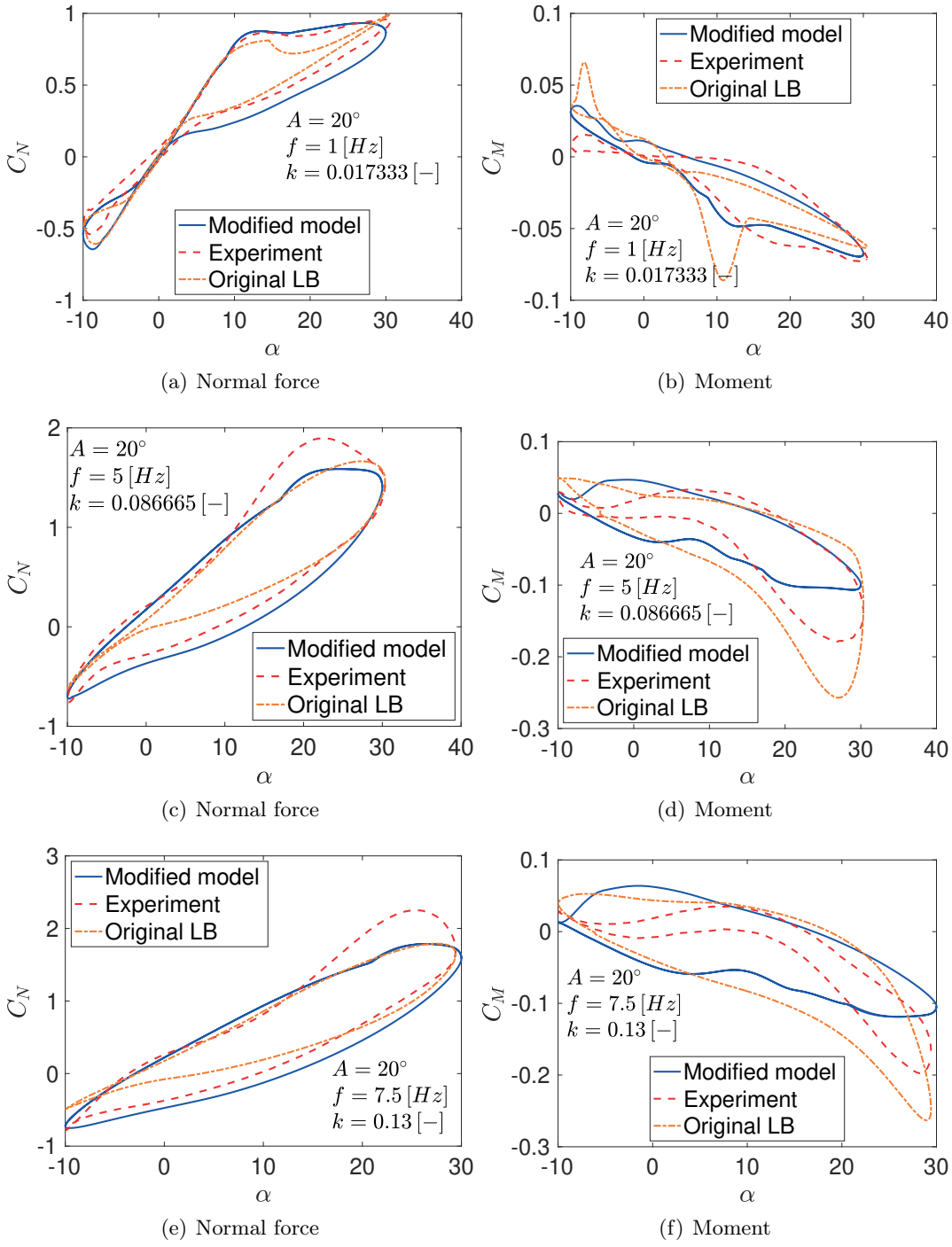

(a) Normal force (b) Moment

(c) Normal force (d) Moment

(e) Normal force (f) Moment

FIGURE 3.11: Comparison between model and experiment for the NACA0018.

Chapter 4

3D unsteady attached flow

In the previous chapters, a modified Leishman Beddoes model was developed in order to compute unsteady aerodynamic loads acting on 2D airfoils at low Reynolds number. In order to extend this model to finite wings, closed form 3D unsteady aerodynamic model must be developed first.

The current chapter presents such an analytical unsteady 3D aerodynamic model. It is constructed by combining Wagner's unsteady 2D aerodynamic theory and Prandtl's lifting line theory. It is known as the Wagner lifting line model (WLL)

4.1 Closed form solutions

Closed form solutions for the attached incompressible unsteady flow problem around a two-dimensional (2D) airfoil exist in both the frequency domain [68] and in the time domain:

- Wagner theory [69], [70]
- Finite state flow model [71]
- Leishman unsteady state-space representation [57])

For three-dimensional (3D) wings there exists one closed form solution for the unsteady aerodynamics of elliptical wings [69]. For general geometries, closed form solutions are usually obtained either from strip theory (see for example Dowell [72]) or from panel methods, such as the Doublet Lattice Method (DLM) [73] or the Vortex Lattice Method (VLM) [74]. Strip theory is based on estimating the 3D unsteady loads by integrating 2D loads along the span. It therefore ignores the downwash induced by the trailing vortices and overestimates the lift; it is mostly used on lifting surfaces with very high aspect ratios, such as helicopter or wind turbine blades. The DLM can be used to estimate modal, frequency domain aerodynamic loads in the form of the generalised aerodynamic force matrix. This matrix is evaluated numerically at discrete reduced frequency values and is interpolated in order to estimate the aerodynamic loads at intermediate frequencies. The generalised force matrix can be transformed to the time domain using rational function, Chebyshev polynomial or indicial function representations, again based on a set of discrete frequency estimations. Several efficient transformation methodologies have been developed, notably the Minimum State approach [75], but they remain approximations. The Vortex Lattice Method can also be used to derive a generalised aerodynamic force matrix [76], [77], which can then be transformed to the time domain.

Alternative closed form solutions of the 3D attached flow problem include Reissner's method [78], which combined the Theodorsen and lifting line theories and was formulated in the frequency domain. Chopra [79] developed expressions for the lift,

thrust and moment of lunate tails oscillating in pitch and plunge, based on the lifting line assumption that the flow is locally 2D around cross-sections of the wing's span but that the local angle of attack is influenced by the vorticity in the wake. The work was limited to rectangular wings and frequency domain solutions for the aerodynamic loads that were obtained. Furthermore, Chopra and Kambe [80] formulated an unsteady lifting surface theory and applied it to wings with non-rectangular planforms but the aerodynamic load calculations were still calculated in the frequency domain. James [81] developed an unsteady lifting line theory for wings of large aspect ratio with smooth tip geometries (such as elliptical planforms). He used a matched asymptotic expansion approach to obtain solutions for impulsively started motion, constant acceleration and sinusoidal oscillations in pitch, plunge or flap. Nevertheless, the method failed to yield total aerodynamic loads for wings whose chord jumps abruptly to zero at the tip (such as rectangular or trapezoidal wings). Furthermore, Ahmadi and Widnall [82] argued that James's theory is only valid for low reduced frequencies and that its 3D results are incorrect. Van Holten [83] also used a matched asymptotic expansion to develop an unsteady lifting line theory for pitching wings and rotating blades but Ahmadi and Widnall [82] again claimed that the work is only valid for low reduced frequencies . Phlips, East, and Pratt [84] derived a time domain unsteady lifting line theory for flapping (but not pitching) wings.

Other frequency domain unsteady lifting line approaches were proposed by Dragos [85], Sclavounos [86] and, more recently, Drela [87]. State-space time domain models are usually quasi-steady, such as the models by Nabawy and Crowther [88], [89]. The present chapter details a robust, closed form, time-domain, 3D unsteady aerodynamic model that does not involve a transformation from the frequency domain. The approach is based on Wagner's 2D unsteady lift theory and Prantdt's lifting line theory and will be referred to as the Wagner Lifting Line (WLL) method. It was first proposed by Boutet and Dimitriadis [90] but is presented here in much more detail, including aeroelastic validation test cases. A similar approach was proposed later by Izraelevitz et al [91], although it was based on a horseshoe vortex representation of 3D wing vorticity, rather than the Fourier Series representation used by the WLL method.

4.2 Method

One of the main characteristics of lifting line theories is that the flow is two-dimensional around spanwise cross-sections but the local angle of attack is affected by the downwash induced by the wake. In the classical version of the theory, the wing and wake are modelled using a superposition of horseshoe vortices whose strength is constant in time. In this way, the wake is constant and semi-infinite and its strength varies in the spanwise but not in the chordwise direction.

In Wagner's and Theodorsen's 2D unsteady aerodynamic theories, the wake is still straight and semi-infinite but its strength varies in the chordwise direction since it is calculated from the unsteady Kutta condition. The wake is assumed to propagate with the free stream velocity, U, so that chordwise displacement and time are directly related by the equation $x = Ut$. A change in vorticity at the trailing edge that occurs at time t_0 will be reflected in the wake at a downstream distance $U(t - t_0)$ at time t.

Lifting line and Wagner theories are not directly compatible because in the former the chordwise strength of the trailing vortices is constant while in the latter it varies. In the present work, Wagner theory is applied to spwanwise cross-sections so that the

strength of the wake varies in both the spanwise and chordwise direction. A quasi-steady version of lifting line theory is used in order to approximate the downwash velocity caused by the wake and to add it to the other sources of downwash used in Wagner theory.

There are three sources of downwash on finite wings in unsteady flow:

- Geometric downwash due to camber and twist.
- Downwash due to the motion of the wing (including the free stream and angle of attack).
- Downwash due to the three-dimensionality of the flow (wing tip vortex effect).

The 3D downwash will be calculated using Prandtl's lifting line theory, as detailed in Kuethe and Chow [92]. The other two downwash contributions will be modelled from Wagner's unsteady aerodynamic theory, as presented by Fung [70].

4.2.1 Lifting line theory

A truncated Fourier series is used to represent an arbitrary time-varying circulation distribution along the span of a flat plate wing

$$\Gamma(t,y) = \frac{1}{2}\, a_0\, c_0\, U \sum_{n=1}^{m} a_n(t) \sin(n\theta) \tag{4.1}$$

where a_0 is the lift curve slope at the wing's axis of symmetry, c_0 is the chord length at the wing's axis of symmetry, U is the free stream airspeed, $a_n(t)$ are the time varying Fourier coefficients, m is the number of terms kept in the series, θ comes from the substitution $y = (s/2)\cos(\theta)$, y represents the location along the span and s represents the span of the wing. In the classical lifting line theory, the wing is split into m spanwise strips and the order of the Fourier series is also m so that the number of unknowns (Fourier coefficients a_n) is equal to the number of equations (spanwise strips).

Using Prandtl's lifting line theory it is possible to compute the downwash w_y caused by the 3D circulation distribution at a location y along the wing span

$$\begin{aligned} w_y &= -\frac{1}{4\pi}\int_{-s/2}^{s/2} \frac{d\Gamma/dy_0}{y - y_0}\, dy_0 \\ &= -\frac{a_0 c_0 U}{4\pi s} \sum_{n=1}^{m} n a_n(t) \int_0^{\pi} \frac{\cos(n\theta_0)}{\cos(\theta_0) - \cos(\theta)}\, d\theta_0 \end{aligned} \tag{4.2}$$

Glauert [93] showed a way to solve the integral so that the downwash w_y can be computed as a function of the Fourier coefficients and the location $y(\theta)$ along the span:

$$w_y(t) = -\frac{a_0 c_0 U}{4s} \sum_{n=1}^{m} n a_n(t) \frac{\sin(n\theta)}{\sin\theta} \tag{4.3}$$

Note that this is a quasi-steady version of lifting line theory, since any instantaneous changes in vorticity over the wing affect the entire wake simultaneously.

4.2.2 Unsteady Kutta-Jukowsky

It is possible to express the unsteady sectional lift coefficient as a function of $a_n(t)$ and location along the span y, using the unsteady Kutta-Jukowsky theorem and considering a lumped spanwise vortex element, as explained by Katz and Plotkin [74] on page 439. The circulatory sectional lift coefficient becomes

$$c_l^c(t,y) = \frac{2\Gamma}{Uc(y)} + \frac{2\dot{\Gamma}}{U^2} \tag{4.4}$$

where Γ is the vortex strength and $c(y)$ is the chord at span section y. The unsteady term $\dot{\Gamma}$ comes from the unsteady Bernouilli equation as shown by Katz and Plotkin [74]. The vortex strength can be replaced by its Fourier series representation from equation 4.1, to obtain

$$c_l^c(t,y) = a_0 \sum_{n=1}^{m} \left(\frac{c_0}{c} a_n + \frac{c_0}{U} \dot{a}_n \right) \sin(n\theta) \tag{4.5}$$

Furthermore, the circulatory lift coefficient for the entire wing can be computed from

$$C_l^c(t) = \int_{-s/2}^{s/2} \frac{\frac{1}{2}\rho U^2 \, c(y) \, c_l^c(t,y) \mathrm{d}y}{\frac{1}{2}\rho U^2 \, S} \tag{4.6}$$

where S is the wing's surface area.

The lift will cause a pitching moment around the pitch axis of each wing section, i.e. the axis around which the wing section can pitch. One can compute the circulatory moment distribution from the lift distribution, assuming that the sectional lift acts on the quarter chord. Refer to figure 4.1, which shows a wing section with chord c and half-chord b at pitch angle α to a free stream U. The position of the pitch axis, x_e, is defined with respect to the half-chord point. The circulatory sectional moment equation is simply

$$c_m^c(t,y) = \frac{c(y)/4 + x_e(y)}{c(y)} c_l^c(t,y) \tag{4.7}$$

where x_e and c are allowed to vary in the spanwise direction y. Note that the pitch axis is measured from the mid-chord point and is defined positive if it lies downstream of that point as defined by Theodorsen [68]. The total circulatory moment coefficient is

$$C_m^c(t) = \int_{-s/2}^{s/2} \frac{\frac{1}{2}\rho U^2 \, c(y)^2 \, c_m^c(t,y) \mathrm{d}y}{\frac{1}{2}\rho U^2 \, S\bar{c}} \tag{4.8}$$

where $\bar{c} = S/s$ is the mean chord.

4.2.3 Wagner's sectional circulatory lift

The computation of the unsteady circulatory aerodynamic loads is based on the circulatory sectional lift $c_l^c(t,y)$ response of an airfoil undergoing a step change in downwash $\Delta w(y) << U$ at span location y. The resulting step change in lift coefficient can be expressed in terms of the Wagner function, $\Phi(t)$, as follows

$$c_l^c(t,y) = a_0(y)\Phi(t)\frac{\Delta w(y)}{U} \tag{4.9}$$

where $a_0(y)$ is the lift curve slope of the local airfoil section, which is approximated by 2π for thin airfoils, and $\Phi(t)$ is Jones' [94] approximation of the Wagner function

$$\Phi(t) = 1 - \Psi_1 e^{-\frac{\epsilon_1 U}{b}t} - \Psi_2 e^{-\frac{\epsilon_2 U}{b}t}$$

with $\Psi_1 = 0.165$, $\Psi_2 = 0.335$, $\epsilon_1 = 0.0455$ and $\epsilon_2 = 0.3$.

Duhamel's principle can be applied to equation 4.9 in order to express a continuous lift response as the time integral of infinitesimal step responses

$$c_l^c(t,y) = a_0(y)\left(\frac{w(0,y)}{U}\Phi(t) + \int_0^t \frac{1}{U}\frac{\partial w(\tau,y)}{\partial \tau}\Phi(t-\tau)\,d\tau\right) \tag{4.10}$$

The troublesome $\frac{\partial w(\tau,y)}{\partial \tau}$ term inside the integral can be removed by applying integration by parts, such that

$$c_l^c(t,y) = a_0(y)\left(\frac{w(t,y)}{U}\Phi(0) - \int_0^t \frac{1}{U}\frac{\partial \Phi(t-\tau)}{\partial \tau}w(\tau,y)\,\mathrm{d}\tau\right) \tag{4.11}$$

The downwash $w(t,y)$ must now be computed; it will depend on the kinematics of the wing. In this work, the wing is assumed to be rigid with pitch and plunge degrees of freedom but flexible wings with bending and torsion modes can also be considered. Figure 4.1 defines the local plunge and pitch degrees of freedom, $h(t,y)$ and $\alpha(t,y)$ respectively. A local downwash w_y is added in order to represent the 3D downwash effects, so that $w(t,y)$ becomes

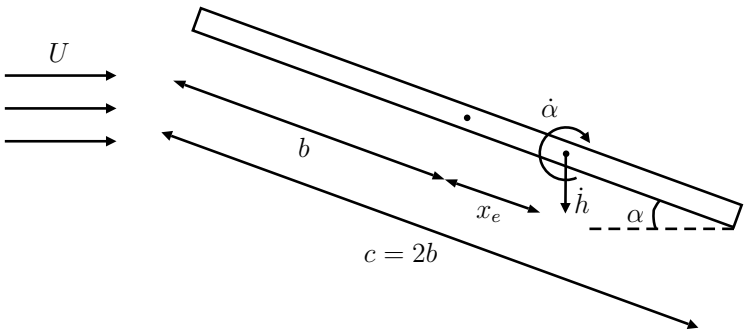

FIGURE 4.1: Rigid thin plate airfoil scheme

$$\begin{aligned} w(t,y) &= U\alpha(t,y) + \dot{h}(t,y) + \dot{\alpha}(t,y)d + w_y(t) \\ d &= \left(\frac{1}{2} - a\right)b \\ a &= \frac{x_e}{b} \end{aligned} \tag{4.12}$$

where d is the non-dimensional distance between the mid-chord and the pitch axis as defined by Theodorsen [68]. After combining equations 4.11 and 4.12,

$$\begin{aligned}\frac{c_l^c(t,y)}{a_0(y)} &= \left(\alpha + \frac{\dot{h}}{U} + \frac{\dot{\alpha}d}{U} + \frac{w_y}{U}\right)\Phi(0) \\ &+ \int_0^t \Psi_1\epsilon_1\frac{U}{b}e^{\frac{-\epsilon_1 U}{b}(t-\tau)}\left(\alpha(\tau) + \frac{\dot{h}(\tau)}{U} + \frac{\dot{\alpha}(\tau)d}{U} + \frac{w_y(\tau)}{U}\right)d\tau \\ &+ \int_0^t \Psi_2\epsilon_2\frac{U}{b}e^{\frac{-\epsilon_2 U}{b}(t-\tau)}\left(\alpha(\tau) + \frac{\dot{h}(\tau)}{U} + \frac{\dot{\alpha}(\tau)d}{U} + \frac{w_y(\tau)}{U}\right)d\tau\end{aligned} \tag{4.13}$$

The following changes of variables are performed in order to eliminate the integrals from equation 4.13, where the variables $z_k(t)$ are called aerodynamics states.

$$\begin{aligned} z_1(t,y) &= \int_0^t e^{\frac{-\epsilon_1 U}{b}(t-\tau)}h(\tau,y)\,d\tau & z_4(t,y) &= \int_0^t e^{\frac{-\epsilon_2 U}{b}(t-\tau)}\alpha(\tau,y)\,d\tau \\ z_2(t,y) &= \int_0^t e^{\frac{-\epsilon_2 U}{b}(t-\tau)}h(\tau,y)\,d\tau & z_5(t,y) &= \int_0^t e^{\frac{-\epsilon_1 U}{b}(t-\tau)}\frac{w_y(\tau)}{U}\,d\tau \\ z_3(t,y) &= \int_0^t e^{\frac{-\epsilon_1 U}{b}(t-\tau)}\alpha(\tau,y)\,d\tau & z_6(t,y) &= \int_0^t e^{\frac{-\epsilon_2 U}{b}(t-\tau)}\frac{w_y(\tau)}{U}\,d\tau \end{aligned} \tag{4.14}$$

Working through the integrals, we obtain

$$\begin{aligned}\frac{c_l^c(t,y)}{a_0(y)} &= \left(\alpha + \frac{\dot{h}}{U} + \frac{\dot{\alpha}d}{U} + \frac{w_y}{U}\right)\Phi(0) - \dot{\Phi}(t)\left(\frac{h(0)}{U} + \frac{\alpha(0)d}{U}\right) \\ &+ \dot{\Phi}(0)\left(\frac{h}{U} + \frac{\alpha d}{U}\right) - \Psi_1\epsilon_1^2\frac{U}{b^2}z_1 - \Psi_2\epsilon_2^2\frac{U}{b^2}z_2 \\ &+ \Psi_1\epsilon_1\frac{U}{b}\left(1 - \frac{\epsilon_1 d}{b}\right)z_3 + \Psi_2\epsilon_2\frac{U}{b}\left(1 - \frac{\epsilon_2 d}{b}\right)z_4 + \Psi_1\epsilon_1\frac{U}{b}z_5 + \Psi_2\epsilon_2\frac{U}{b}z_6\end{aligned} \tag{4.15}$$

First order differential equations for the aerodynamic state variables can be derived using Leibnitz's integral rule. As an example, the equation for $z_1(t,y)$ is

$$\begin{aligned}\dot{z_1}(t,y) &= e^{\frac{-\epsilon_1 U(t-t)}{b}}h(t,y)\frac{\partial t}{\partial t} - e^{\frac{-\epsilon_1 U\tau}{b}}h(0,y)\frac{\partial 0}{\partial t} - \frac{\epsilon_1 U}{b}\int_0^t e^{\frac{-\epsilon_1 U}{b}(t-\tau)}h(\tau,y)\,d\tau \\ &= h - \frac{\epsilon_1 U}{b}z_1(t,y)\end{aligned} \tag{4.16}$$

The equations for all the aerodynamic states are given by

$$\begin{aligned} \dot{z_1}(t,y) &= h - \frac{\epsilon_1 U}{b}z_1(t,y) & \dot{z_4}(t,y) &= \alpha - \frac{\epsilon_2 U}{b}z_4(t,y) \\ \dot{z_2}(t,y) &= h - \frac{\epsilon_2 U}{b}z_2(t,y) & \dot{z_5}(t,y) &= \frac{w_y}{U} - \frac{\epsilon_1 U}{b}z_5(t,y) \\ \dot{z_3}(t,y) &= \alpha - \frac{\epsilon_1 U}{b}z_3(t,y) & \dot{z_6}(t,y) &= \frac{w_y}{U} - \frac{\epsilon_2 U}{b}z_6(t,y) \end{aligned} \tag{4.17}$$

Finally, the continuous unsteady circulatory lift coefficient can be written as follows

$$c_l^c(t,y) = \mathbf{C}\dot{\mathbf{q}} + \mathbf{D}\mathbf{q} + \mathbf{E}\mathbf{z} + r\dot{\Phi}(t) + a_0(y)\Phi(0)\frac{w_y}{U} \tag{4.18}$$

$$\dot{\mathbf{z}} = \mathbf{W}\mathbf{z} + \mathbf{F}\mathbf{q} + \mathbf{G}\frac{w_y}{U} \tag{4.19}$$

where

$$\begin{aligned}
\mathbf{q} &= \begin{bmatrix} h(t,y) & \alpha(t,y) \end{bmatrix}^T \\
\mathbf{z} &= \begin{bmatrix} z_1(t,y) & z_2(t,y) & z_3(t,y) & z_4(t,y) & z_5(t,y) & z_6(t,y) \end{bmatrix}^T \\
\mathbf{D} &= \frac{a_0(y)}{U}\begin{bmatrix} \dot{\Phi}(0) & U\Phi(0) + d\dot{\Phi}(0) \end{bmatrix} \\
\mathbf{E} &= \frac{a_0(y)U}{b}\begin{bmatrix} -\frac{\Psi_1\epsilon_1^2}{b} & -\frac{\Psi_2\epsilon_2^2}{b} & \Psi_1\epsilon_1\left(1-\epsilon_1\frac{d}{b}\right) & \Psi_2\epsilon_2\left(1-\epsilon_2\frac{d}{b}\right) & \Psi_1\epsilon_1 & \Psi_2\epsilon_2 \end{bmatrix} \\
\mathbf{G} &= \begin{bmatrix} 0 & 0 & 0 & 0 & 1 & 1 \end{bmatrix}^T \\
\mathbf{C} &= \frac{a_0(y)}{U}\Phi(0)\begin{bmatrix} 1 & d \end{bmatrix} \\
r &= -\frac{a_0(y)}{U}\left(h(0,y) + d\alpha(0,y)\right) \\
\mathbf{W} &= -\frac{U}{b}\mathrm{diag}\left(\epsilon_1, \epsilon_2, \epsilon_1, \epsilon_2, \epsilon_1, \epsilon_2\right) \\
\mathbf{F} &= \begin{bmatrix} 1 & 1 & 0 & 0 & 0 & 0 \\ 0 & 0 & 1 & 1 & 0 & 0 \end{bmatrix}^T
\end{aligned}$$

4.2.4 Added mass effect

The non-circulatory sectional lift and moment coefficients, also known as the added mass effect, can be computed from the non-circulatory terms derived by Theodorsen [68]

$$c_l^i(t,y) = \frac{\pi b}{U^2}\left(\ddot{h} - a\,b\,\ddot{\alpha}\right) + \frac{\pi b}{U}\dot{\alpha} \tag{4.20}$$

$$c_m^i(t,y) = \frac{\pi b}{2U^2}\left[a\ddot{h} - \left(a^2 + \frac{1}{8}\right)\ddot{\alpha}\right] - \left(\frac{1}{2} - a\right)\frac{\pi b}{2U}\dot{\alpha} \tag{4.21}$$

The computation of the total non-circulatory lift C_l^i and moment C_m^i coefficient follows the same principle as equations 4.6 and 4.8 and the final result is given in equations 4.51 and 4.52 for a rectangular wing.

4.2.5 Assembling the pieces together

In order to compute the m Fourier coefficients a_n, m spanwise wing strips are considered, as shown in figure 4.2 which represents m strips along the wing span, their respective local aerodynamics variables $\mathbf{z_i}$, 3D downwash effects $w_{y,i}$ and chord section c_i. For an arbitrary strip i, equations 4.1 and 4.18-4.19 can be combined to obtain

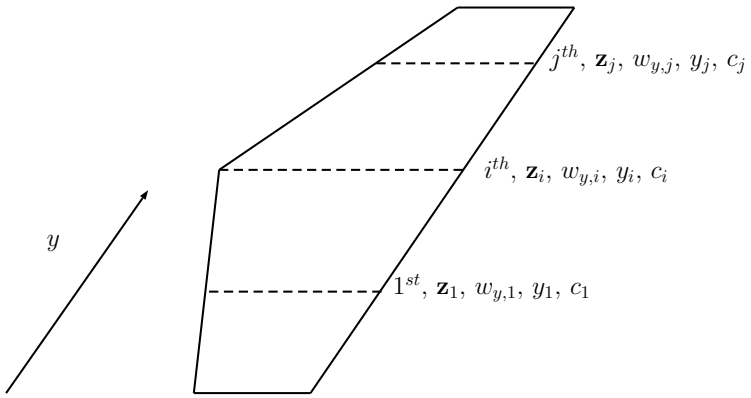

FIGURE 4.2: Representation of m strips along the wing span and their respective local variables

the following system

$$\begin{aligned} \overbrace{a_0(y_i)\sum_{n=1}^{m}\left(\frac{c_0}{c_i}a_n+\frac{c_0}{U}\dot{a}_n\right)\sin(n\theta_i)}^{c_l^c(t,y_i)} &= \mathbf{C_i}\dot{\mathbf{q}}+\mathbf{D_i}\mathbf{q}+\mathbf{E_i}\mathbf{z}_i+a_0(y_i)\Phi(0)\frac{w_{y_i}}{U} \\ \dot{\mathbf{z}}_i &= \mathbf{W_i}\mathbf{z}_i+\mathbf{F}\mathbf{q}+\mathbf{G}\frac{w_{y_i}}{U} \end{aligned} \tag{4.22}$$

The variables $\mathbf{z}_i$ represent the local aerodynamic state variables for the ith strip. Matrices $\mathbf{C_i}$, $\mathbf{D_i}$, $\mathbf{E_i}$, $\mathbf{W_i}$ are the matrices computed in section 4.2.3 where the chord c is replaced with its local value c_i. Variable w_{y_i} represents the 3D downwash effect on the ith strip; its value is given by equation 4.3. Substituting for w_{y_i} and re-arranging, equations 4.22 become

$$a_0(y_i)\sum_{n=1}^{m}\left(\left(\frac{c_0}{c_i}+\Phi(0)\frac{a_0c_0n}{4s\sin(\theta_i)}\right)a_n+\frac{c_0}{U}\dot{a}_n\right)\sin(n\theta_i) = \mathbf{C_i}\dot{\mathbf{q}}+\mathbf{D_i}\mathbf{q}+\mathbf{E_i}\mathbf{z}_i$$

$$\dot{\mathbf{z}}_i = \mathbf{W_i}\mathbf{z}_i+\mathbf{F}\mathbf{q}-\mathbf{G}\frac{a_0c_0}{4s}\sum_{n=1}^{m}na_n(t)\frac{\sin(n\theta_i)}{\sin\theta_i} \tag{4.23}$$

Applying equations 4.23 to all m strips, a set of $7m$ ordinary linear differential equations for $7m$ unknowns (m for the Fourier coefficients a_n and $6m$ for the aerodynamic states $\mathbf{z}_1,\dots\mathbf{z}_m$) is obtained. Once this system of ODEs is solved and the coefficients $a_n(t)$ are evaluated, the lift distribution acting on the wing can be computed from relation 4.5, the total lift from 4.6 and the total pitching moment from 4.8.

The computation of the aerodynamic loads for a rectangular wing is fully detailed in the appendix with equations 4.26 to 4.54.

4.2.6 Asymptotic behavior for a rectangular wing ($c = c_0$)

By imposing stationarity, all derivatives in time vanish and the system of equations 4.23 should reduce to the classical lifting line theory. After imposing stationarity

on equations 4.17, the aerodynamic states variables become

$$\begin{aligned} z_1(y) &= \frac{b}{\epsilon_1 U} h(y) & z_4(y) &= \frac{b}{\epsilon_2 U} \alpha(y) \\ z_2(y) &= \frac{b}{\epsilon_2 U} h(y) & z_5(y) &= \frac{b}{\epsilon_1 U^2} w_y \\ z_3(y) &= \frac{b}{\epsilon_1 U} \alpha(y) & z_6(y) &= \frac{b}{\epsilon_2 U^2} w_y \end{aligned} \tag{4.24}$$

Injecting these expressions in equations 4.23 and applying the necessary simplifications, the system becomes

$$a_0(y) \sum_{n=1}^{m} \left(1 + \Phi(0) \frac{a_0(y) nc}{4s \sin(\theta_i)} \right) a_n \sin(n\theta_i) = a_0(y)\alpha(y) + a_0(y)\Phi(0)\frac{w_y}{U}$$

or

$$\sum_{n=1}^{m} \left(1 + \frac{a_0(y) nc}{4s \sin(\theta_i)} \right) a_n \sin(n\theta_i) = \alpha(y)$$

which is the equation derived by Kuethe and Chow [92] for a rectangular wing, using Prandtl's lifting line theory for a constant pitch angle $\alpha(y) = \alpha$.

If the span of the wing is infinite, $s = \infty$, all 3D effects vanish and system 4.23 should reduce to the 2D Wagner solution. Looking at equation 4.3, it is obvious that $\lim_{s\to\infty} w_y = 0$. It can then be shown from equations 4.14 that $z_5 = 0$ and $z_6 = 0$. The system of equations 4.23 is now reduced to

$$\begin{aligned} c_l^c(t) &= a_0(y) \sum_{n=1}^{m} \left(a_n + \frac{c}{U} \dot{a}_n \right) \sin(n\theta_i) = \mathbf{C}\dot{\mathbf{q}} + \mathbf{D}\mathbf{q} + \mathbf{E}\mathbf{z}_i \\ \dot{\mathbf{z}}_i &= \mathbf{W}\mathbf{z}_i + \mathbf{F}\mathbf{q} \\ \mathbf{z_i} &= \begin{bmatrix} z_{1,i} & z_{2,i} & z_{3,i} & z_{4,i} & 0 & 0 \end{bmatrix}^T \end{aligned} \tag{4.25}$$

which is the classical 2D Wagner formulation, as given by Fung [70] for all arbitrary strips i.

4.3 Wagner lifting line aeroelastic matrix computation

4.3.1 Sectional normal lift

First, equation 4.5 for the sectional normal lift coefficient can be expressed in matrix form as

$$c_l^c(t, y_i) = a_0 \sum_{n=1}^{m} \left(\frac{c_0}{c_i} a_n + \frac{c_0}{U} \dot{a}_n \right) \sin(n\theta_i) \tag{4.26}$$

$$= \mathbf{A}_{\mathbf{y_i}} \mathbf{a_n} + \mathbf{D}_{\mathbf{y_i}} \dot{\mathbf{a}}_{\mathbf{n}} \tag{4.27}$$

where $c_l^c(i)$ is the sectional lift at the ith strip, $y(i)$ is the location y of the ith strip, $\mathbf{a_n} = [a_1\ a_2\ \ldots a_m]^T$, while $\mathbf{A}_{\mathbf{y_i}}$ and $\mathbf{D}_{\mathbf{y_i}}$ are matrix coefficients. The special cases $i = 0$ and $i = m + 1$ correspond to the wingtips which are not normal strips. There

is no lift at the wingtips, so that

$$\begin{aligned} y_0 &= -s/2 \\ y_{m+1} &= s/2 \\ c_l^c(t, y_0) &= c_l^c(t, y_{m+1}) = 0 \end{aligned}$$

4.3.2 Downwash

The equation for the downwash 4.3 can be expressed in the following matrix form

$$w_{y_i}(t) = -\frac{a_0 c_0 U}{4s} \sum_{n=1}^{m} n a_n(t) \frac{\sin(n\theta_i)}{\sin\theta_i} \tag{4.28}$$

$$= \mathbf{W_{y_i} a_n} \tag{4.29}$$

where $\mathbf{W_{y_i}}$ is a matrix coefficient.

4.3.3 Wagner lifting line

Using expressions 4.27 and 4.29 the Wagner lifting line equations 4.22 at the ith strip can be rewritten in the following matrix form

$$\mathbf{A_{y_i} a_n} + \mathbf{D_{y_i} \dot{a}_n} = \mathbf{C_i \dot{q}} + \mathbf{D_i q} + \mathbf{E_i z}_i + \frac{a_0 \Phi(0)}{U} \mathbf{W_{y_i} a_n} \tag{4.30}$$

$$\dot{\mathbf{z}}_i = \mathbf{W_i z}_i + \mathbf{F q} + \frac{\mathbf{G}}{U} \mathbf{W_{y_i} a_n} \tag{4.31}$$

For simplicity, it is assumed that a_0 is not a function of the span location y. Then, expressions 4.30 and 4.31 are extended to include the equations for all the m strips.

$$\mathbf{D_{y_M} \dot{a}_n} = \mathbf{C_M \dot{q}} + \mathbf{D_M q} + \mathbf{E_M z} + (\mathbf{W_{y_M}} - \mathbf{A_{y_M}}) \mathbf{a_n} \tag{4.32}$$

$$\dot{\mathbf{z}} = \mathbf{W_M z} + \mathbf{F_M q} + \mathbf{W_{G_M} a_n} \tag{4.33}$$

where

$$\mathbf{z} = \begin{bmatrix} \mathbf{z_1} & \dots & \mathbf{z_i} & \dots & \mathbf{z_m} \end{bmatrix}^T \tag{4.34}$$

$$\mathbf{A_{y_M}} = \begin{bmatrix} \mathbf{A_{y_1}} & \dots & \mathbf{A_{y_i}} & \dots & \mathbf{A_{y_m}} \end{bmatrix}^T \tag{4.35}$$

$$\mathbf{D_{y_M}} = \begin{bmatrix} \mathbf{D_{y_1}} & \dots & \mathbf{D_{y_i}} & \dots & \mathbf{D_{y_m}} \end{bmatrix}^T \tag{4.36}$$

$$\mathbf{C_M} = \begin{bmatrix} \mathbf{C_1} & \dots & \mathbf{C_i} & \dots & \mathbf{C_m} \end{bmatrix}^T \tag{4.37}$$

$$\mathbf{D_M} = \begin{bmatrix} \mathbf{D_1} & \dots & \mathbf{D_i} & \dots & \mathbf{D_m} \end{bmatrix}^T \tag{4.38}$$

$$\mathbf{E_M} = diag\,(\mathbf{E_1}, \dots, \mathbf{E_i}, \dots, \mathbf{E_m}) \tag{4.39}$$

$$\mathbf{W_{y_M}} = \frac{a_0 \Phi(0)}{U} \begin{bmatrix} \mathbf{W_{y_1}} & \dots & \mathbf{W_{y_i}} & \dots & \mathbf{W_{y_m}} \end{bmatrix}^T \tag{4.40}$$

$$\mathbf{W_M} = diag\,(\mathbf{W_1}, \dots, \mathbf{W_i}, \dots, \mathbf{W_m}) \tag{4.41}$$

$$\mathbf{F_M} = \begin{bmatrix} \mathbf{F} & \dots & \mathbf{F} & \dots & \mathbf{F} \end{bmatrix}^T \tag{4.42}$$

$$\mathbf{W_{G_M}} = \begin{bmatrix} \frac{\mathbf{G}}{U}\mathbf{W_{y_1}} & \dots & \frac{\mathbf{G}}{U}\mathbf{W_{y_i}}, \dots, \frac{\mathbf{G}}{U}\mathbf{W_{y_m}} \end{bmatrix}^T \tag{4.43}$$

4.3.4 Trapezoidal rule

The computation of the circulatory lift for a rectangular wing can be expressed by the integral

$$L^c(t) = \frac{1}{2}\rho U^2 c \int_{-s/2}^{s/2} c_l^c(t,y)\mathrm{d}y \tag{4.44}$$

Then, using the trapezoidal rule, this integral can be approximated by the sum

$$L^c(t) = \frac{1}{2}\rho U^2 c \sum_{i=1}^{m+1} \frac{y_i - y_{i-1}}{2}\left(c_l^c(t,y_{i-1}) + c_l^c(t,y_i)\right) \tag{4.45}$$

or, in matrix form,

$$L^c(t) = \frac{1}{2}\rho U^2 c \begin{bmatrix} y_1 - y_0 & \dots & y_{m+1} - y_m \end{bmatrix} \begin{bmatrix} c_l^c(t,y_1) \\ \vdots \\ c_l^c(t,y_{i-1}) + c_l^c(t,y_i) \\ \vdots \\ c_l^c(t,y_m) \end{bmatrix} \tag{4.46}$$

$$= \frac{1}{2}\rho U^2 c \begin{bmatrix} y_1 - y_0 & \dots & y_{m+1} - y_m \end{bmatrix} \begin{bmatrix} 1 & 0 & \dots & 0 \\ 1 & 1 & \ddots & \vdots \\ 0 & \ddots & \ddots & 0 \\ \vdots & \ddots & 1 & 1 \\ 0 & \dots & 0 & 1 \end{bmatrix} \begin{bmatrix} c_l^c(t,y_1) \\ \vdots \\ c_l^c(t,y_m) \end{bmatrix} \tag{4.47}$$

$$= \mathbf{T} \begin{bmatrix} c_l^c(t,y_1) \\ c_l^c(t,y_2) \\ \vdots \\ c_l^c(t,y_m) \end{bmatrix} \tag{4.48}$$

Using expression 4.27 one can write

$$L^c(t) = \mathbf{T}\mathbf{A}_{\mathbf{y_i}}\mathbf{a_n} + \mathbf{T}\mathbf{D}_{\mathbf{y_i}}\dot{\mathbf{a}}_{\mathbf{n}} \tag{4.49}$$

As the chord and the location of the pitch axis are constant with span for a rectangular wing, the circulatory moment in pitch M^c is simply

$$M^c(t) = (c/4 + x_e)L^c(t) \tag{4.50}$$

4.3.5 Non-circulatory loads

It is assumed that the wing is rectangular, therefore the non-circulatory load coefficient are identical to the sectional lift coefficients described in section 4.2.4. They are written as

$$L^i(t) = \frac{1}{2}\rho U^2 c \left(\frac{\pi b}{U^2}\left(\ddot{h} - a\,b\,\ddot{\alpha}\right) + \frac{\pi b}{U}\dot{\alpha}\right) = \mathbf{A_l}\ddot{\mathbf{q}} + \mathbf{B_l}\dot{\mathbf{q}} \tag{4.51}$$

$$M^i(t) = \frac{1}{2}\rho U^2 c^2 s \left(\frac{\pi b}{2U^2}\left[a\ddot{h} - \left(a^2 + \frac{1}{8}\right)\ddot{\alpha}\right] - \left(\frac{1}{2} - a\right)\frac{\pi b}{2U}\dot{\alpha}\right) = \mathbf{A_m}\ddot{\mathbf{q}} + \mathbf{B_m}\dot{\mathbf{q}} \tag{4.52}$$

4.3.6 Total aerodynamic loads

The total lift applied on the wing can be written as

$$\begin{aligned} L &= L^c(t) + L^i(t) \\ &= \mathbf{TA_{y_i} a_n} + \mathbf{TD_{y_i} \dot{a}_n} + \mathbf{A_l \ddot{q}} + \mathbf{B_l \dot{q}} \end{aligned} \tag{4.53}$$

Similarly, the total pitching moment is

$$\begin{aligned} M &= M^c(t) + M^i(t) \\ &= (c/4 + x_e)\mathbf{TA_{y_i} a_n} + (c/4 + x_e)\mathbf{TD_{y_i} \dot{a}_n} + \mathbf{A_m \ddot{q}} + \mathbf{B_m \dot{q}} \end{aligned} \tag{4.54}$$

4.3.7 Structural equations

From expression 4.53 and 4.54, equations 5.5 can be written as

$$\left(\begin{bmatrix} m_w & S_w \end{bmatrix} + \mathbf{A_l}\right) \mathbf{\ddot{q}} + \mathbf{TD_{y_i} \dot{a}_n} = -\mathbf{TA_{y_i} a_n} - \mathbf{B_l \dot{q}} - \begin{bmatrix} k_h & 0 \end{bmatrix} \mathbf{q} \tag{4.55}$$

$$\left(\begin{bmatrix} S_w & I_w \end{bmatrix} + \mathbf{A_m}\right) \mathbf{\ddot{q}} + (c/4 + x_e)\mathbf{TD_{y_i} \dot{a}_n} = -(c/4 + x_e)\mathbf{TA_{y_i} a_n} - \mathbf{B_m \dot{q}} - \begin{bmatrix} 0 & k_\alpha \end{bmatrix} \mathbf{q} \tag{4.56}$$

4.3.8 Aeroelastic system matrix

Finally, expressions 4.32, 4.33, 4.55 and 4.56 can be summarized in the following algebraic linear form

$$\mathbf{H_1} \begin{bmatrix} \mathbf{\dot{a}_n} \\ \mathbf{\dot{z}} \\ \mathbf{\dot{q}} \\ \mathbf{\ddot{q}} \end{bmatrix} = \mathbf{H_2} \begin{bmatrix} \mathbf{a_n} \\ \mathbf{z} \\ \mathbf{q} \\ \mathbf{\dot{q}} \end{bmatrix} \tag{4.57}$$

Then, the global aeroelastic system matrix $\mathbf{H}$ of equation 5.6 is given by

$$\mathbf{H} = \mathbf{H_1}^{-1}\mathbf{H_2} \tag{4.58}$$

Chapter 5

3D model comparisons

In the previous chapter, the Wagner Lifting Line model was developped as a mean to compute the unsteady attached lift and moment acting on a finite wing.

In the present chapter, the WLL is applied on both a rectangular and a tapered wing undergoing unsteady motion. The results are then compared to the predictions obtained from Vortex Lattice simulation. Both forced motion and free aeroelastic responses are considered in this validation.

5.1 Test cases

The Wagner Lifting Line method is applied here to a rectangular and a tapered wing. The rectangular wing, shown on Figure 5.1, has constant chord $c = 1$ m, span s, surface $S = cs$ and aspect ratio $AR = s^2/S$. It has two degrees of freedom, a pure plunge $h(t, y) = h(t)$ and a pure pitch angle $\alpha(t, y) = \alpha(t)$ around its pitch axis. Two positions of the pitch axis are considered: one at the leading edge and one at the quarter chord.

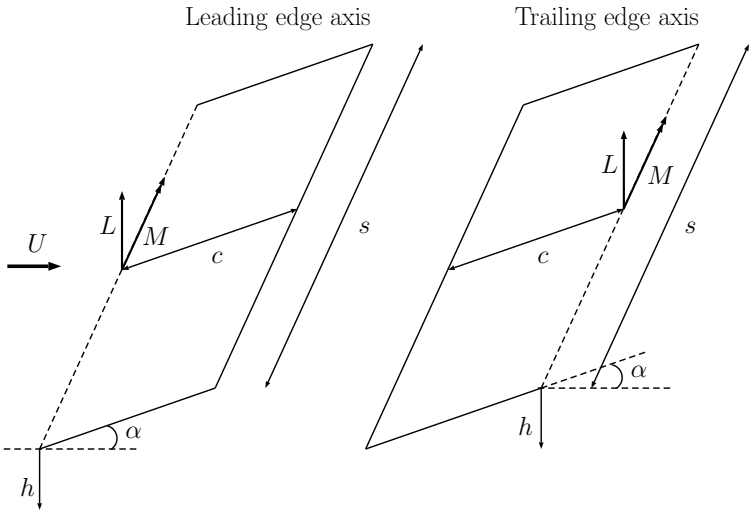

FIGURE 5.1: Rectangular wing with pitch axis at the leading edge and quarter chord.

The tapered wing, shown on Figure 5.2 has root chord $c_0 = 1\,\text{m}$, tip chord $c_t = 0.5\,\text{m}$, span s, surface $S = (c_0 + c_t)\,\frac{s}{2}$ and aspect ratio $AR = s^2/S$. It has the same degrees of freedom as the rectangular wing. The pitch axis is defined with respect to the root chord, as shown in figure 5.2. Again, leading edge and quarter chord pitch axis locations are considered.

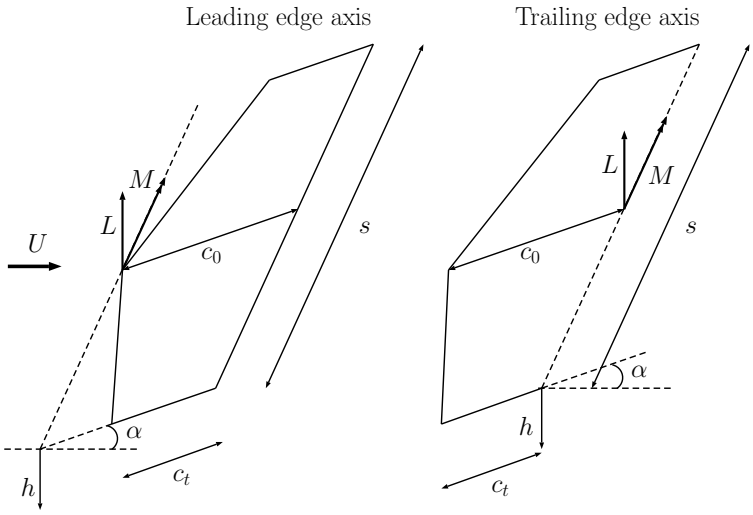

FIGURE 5.2: Tapered wing with pitch axis at the leading edge and quarter chord.

5.1.1 Types of motion

The degrees of freedom of the wings are subjected to two kinds of motion: step changes and sinusoidal oscillations. The step is expressed as the function $f = A\left(1 - e^{-10t}\right)$ where t is the time and A is the position of the degree of freedom after the step. Steps $\Delta h = 0.1\,\text{m}$ and $\Delta\alpha = 5^\circ$ are separately applied to the plunge and pitch degrees of freedom.

Sinusoidal oscillations with ten distinct frequencies are tested separately for each degree of freedom, in order to assess the WLL model's frequency response. The oscillations are expressed as $f = A\cos\left(\frac{2Uk}{c_0}t\right)$ where t is the time, A the amplitude of the oscillation, $k = [0.1,\ 0.2,\ 0.3\ldots\ 1]$ is the reduced frequency. The pitch and plunge amplitudes are respectively set to $A = 5^\circ$ and $A = 0.1\,\text{m}$.

5.1.2 Validation

The unsteady Vortex Lattice Method (VLM) is used as a reference solution to which the results obtained by the Wagner Lifting Line approach are to be compared. The particular implementation of the VLM used here is more thoroughly described by Dimitriadis, Gardiner, Tickle, *et al.* [95]. The difference between the solutions obtained from WLL and VLM is quantified using the Normalized Root-Mean-Square Deviation (NRMSD).

$$RMSD = \sqrt{\frac{\sum_{t=1}^{N}\left(y_{w,r} - y_{v,r}\right)^2}{N}} \tag{5.1}$$

$$NRMSD = 100 \times \frac{RMSD}{max(y_v) - min(y_v)}\,[\%] \tag{5.2}$$

where N is the number of time instances, $y_{v,r}$ represents the lift or moment coefficient computed by the VLM at the rth time instance and $y_{w,r}$ represents the lift or moment coefficient computed by the WLL approach at the rth time instance.

5.2 Convergence

The differential equations 4.23 are solved by means of a Runge-Kutta-Fehlberg 45 numerical time integration technique. A time convergence analysis is therefore needed in order to minimise numerical integration errors without increasing too much the computation time. A convergence analysis is also performed for the vortex lattice method.

As shown in equation 4.1, the WLL uses a truncated Fourier series with j coefficients, which correspond to the j spanwise strips shown in figure 4.2. A spatial convergence study must also be carried out in order to determine the effect of the number of strips on the aerodynamic load predictions. Note that the number of states in the system is $7j$, therefore keeping j as low as possible is important. The NRMSD is used in order to determine if convergence has been achieved, such that

$$RMSD(i) = \sqrt{\frac{\sum_{t=1}^{N}\left(y_{i,t} - y_{ref,t}\right)^2}{N}} \tag{5.3}$$

$$NRMSD(i) = e(i) = 100 \times \frac{RMSD}{max(y_{ref}) - min(y_{ref})}\,[\%] \tag{5.4}$$

where $y_{i,t}$ represents the lift coefficient response at the tth time instance for the ith value of the convergence parameter. The latter can be either the time step tolerance of the Runge-Kutta-Fehlberg scheme or the number of strips; y_{ref} represents the reference lift coefficient against which the convergence is assessed. This reference is computed for an appropriately high value of the convergence parameter.

5.2.1 Runge-Kutta convergence

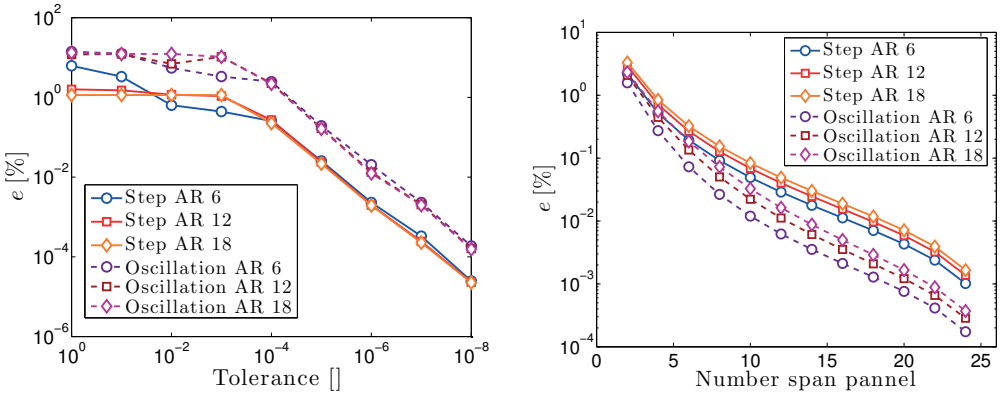

(a) Tolerance parameter

(b) Number of spanwise strips

FIGURE 5.3: WLL convergence with tolerance parameter and number of spanwise strips for a rectangular wing

The time step tolerance controls the error of the Runge-Kutta time integration scheme. Given the solution arrays $\mathbf{r}_4$ and $\mathbf{r}_5$ of the respective 4^{th} and 5^{th} order Runge-Kutta estimates for a current time t_i and time step Δt, the Runge-Kutta-Fehlberg algorithm used in this work is given by

- if $Tol < (\mathbf{r}_5 - \mathbf{r}_4)(\mathbf{r}_5 - \mathbf{r}_4)^T$, reduce the time step to $\Delta t/2$

- otherwise, go to the next time instance $t_{i+1} = t_i + \Delta t$ and reset Δt to its default value

Figure 5.3 plots the variation of the error of equation 5.4 with the tolerance Tol used in the Runge-Kutta-Fehlberg 45 algorithm with respect to a reference $Tol = 10^{-9}$. The solid line represents the convergence for a step case and the dashed line the convergence for a sinusoidal oscillation case with a reduced frequency $k = 0.3$. Assuming that $e < 10^{-2}\%$ is good accuracy, the figure shows that a tolerance value of 10^{-7} is sufficient to achieve convergence for both the step and sinusoidal motion.

Figure 5.3(b) plots the variation of the error of equation 5.4 with number of strips for different aspect ratios and kinematics with respect to a reference number of strips $j = 26$. The time step tolerance is fixed to 10^{-7}. It can be seen that, for all cases, a value of $j = 20$ is sufficient to achieve errors $e < 10^{-2}\%$. The figure also shows that the higher the AR, the greater the number of strips necessary to reach the same level of convergence. This phenomenon is due to the fact that higher aspect ratios require more strips to achieve good spatial resolution.

5.2.2 Vortex lattice convergence

The quality of the solutions obtained from the vortex lattice method is based on the number of panels used to represent the wing in the spanwise and chordwise directions. The VLM is more sensitive to the chordwise than the spanwise number of panels [96], so a convergence for the number of chordwise panels is performed.

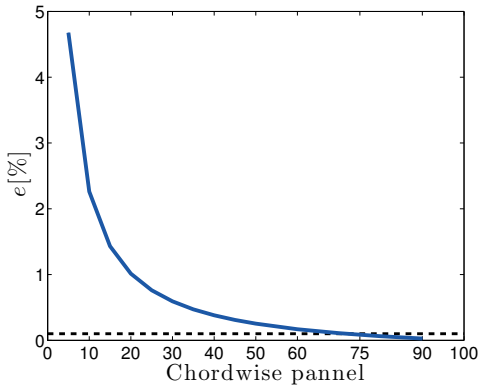

FIGURE 5.4: VLM convergence with number of chordwise panels.

Figure 5.4 plots the variation of the error of equation 5.4 with number of chordwise panels for a rectangular wing ($AR = 6$) oscillating around its leading edge with a reduced frequency $k = 0.3$. The reference chordwise panels is $m = 100$. The number of spanwise panels is set to 15. It can be seen that $m = 75$ is sufficient to achieve errors $e < 10^{-1}\%$ for the rectangular wing case with a leading edge pitch axis.

All other test cases used in this work converge for $m = 75$, as long as the pitch axis does not lie at $c_0/4$. A larger number of chordwise panels $m = 100$ is necessary for convergence when the pitch axis lise on the quarter chord because the moment loads need to converge to values very close to zero for the oscillating case with low reduced frequency. Convergence is therefore harder to achieve.

5.3 Lift and moment results for rectangular wing

In this section the WLL method is applied to the rectangular wing under different kinematic conditions. The lift and moment estimates are compared to predictions obtained by the VLM technique and by strip theory. In all cases, the VLM estimates were obtained from time-converged and spatially converged simulations.

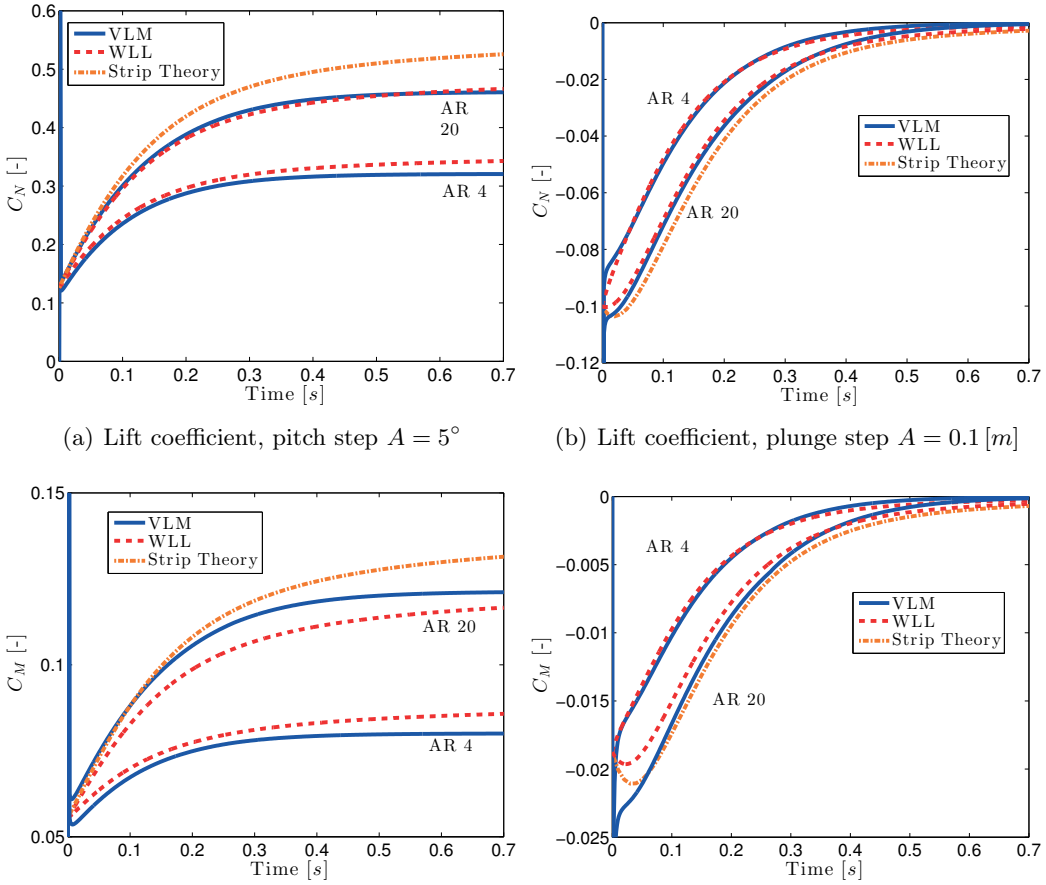

(a) Lift coefficient, pitch step $A = 5°$

(b) Lift coefficient, plunge step $A = 0.1\,[m]$

(c) Moment coefficient, pitch step $A = 5°$

(d) Moment coefficient, plunge step $A = 0.1\,[m]$

FIGURE 5.5: Comparison between VLM, WLL and strip theory for a rectangular wing undergoing a step motion

For the first comparison, the pitch axis is located at the leading edge and the wing undergoes a step change in pitch or plunge, as explained in section 5.1.1. The resulting lift and moment responses are shown in figure 5.5; the WLL estimates are in good agreement with the VLM results for both pitch and plunge motions. In contrast, the strip theory result is significantly overestimated in the pitch step case and underestimated in the plunge step case. Note that the agreement in pitching moment for the step pitch case is not as good as in the other results. Furthermore, small differences between the VLM and WLL predictions persist at steady-state conditions; this is due to the fact that the steady VLM and lifting line theory model the bound vorticity in a different manner. Repeating the simulations after relocating the pitch axis to the quarter chord resulted in WLL predictions that were also in good agreement with the VLM estimates.

For the second comparison, the WLL, VLM and strip theory techniques are applied to a rectangular wing with aspect ratio 6 undergoing sinusoidal oscillations in pitch

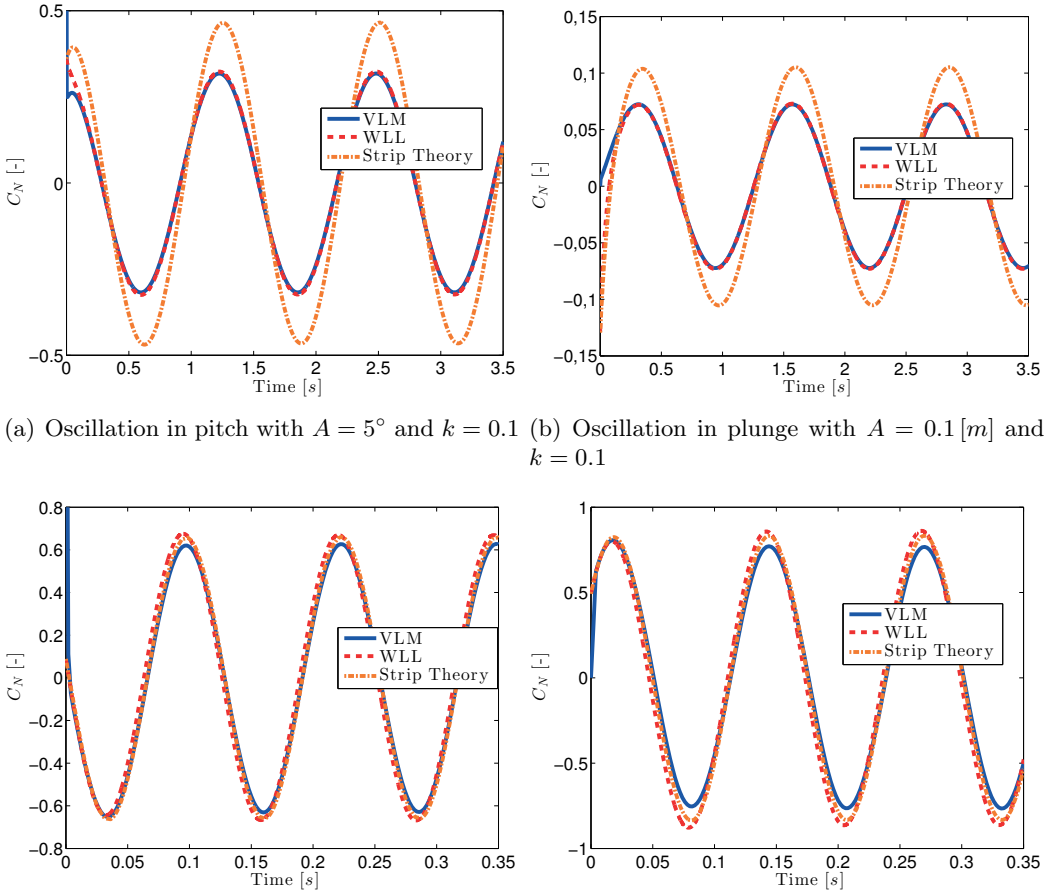

(a) Oscillation in pitch with $A = 5°$ and $k = 0.1$ (b) Oscillation in plunge with $A = 0.1\,[m]$ and $k = 0.1$

(c) Oscillation in pitch with $A = 5°$ and $k = 0.3$ (d) Oscillation in plunge with $A = 0.1\,[m]$ and $k = 0.3$

FIGURE 5.6: Lift comparison between VLM, WLL and strip theory for a rectangular wing undergoing an oscillation motion.

or plunge, as detailed in section 5.1.1. Several reduced frequency values were tested but only the results for $k = 0.1$ and $k = 0.3$ are presented here. The lift results are plotted in figure 5.6 and the moment results in figure 5.7. There is very good agreement between the WLL and VLM predictions for all frequencies, while the strip theory estimates are quite inaccurate at both values of k.

Figure 5.8(a) plots the NRMSD values calculated from equation 5.2, for all the tested values of k. The difference between the WLL and VLM predictions increases with reduced frequency but stays lower than 3% for all kinematics and aerodynamic loads. This level of difference is considered good for such high frequencies. Repeating the simulations after moving the pitch axis to the quarter chord, as shown in figure 5.8(b), results in equally good agreement between the WLL and VLM aerodynamic load predictions.

5.4 Lift and moment results for tapered wing

In this section, step and sinusoidal numerical tests are applied to the tapered wing with aspect ratio 6 described in section 5.1. Initially the pitch axis is located at the leading edge of the root chord and the wing undergoes step changes in pitch or

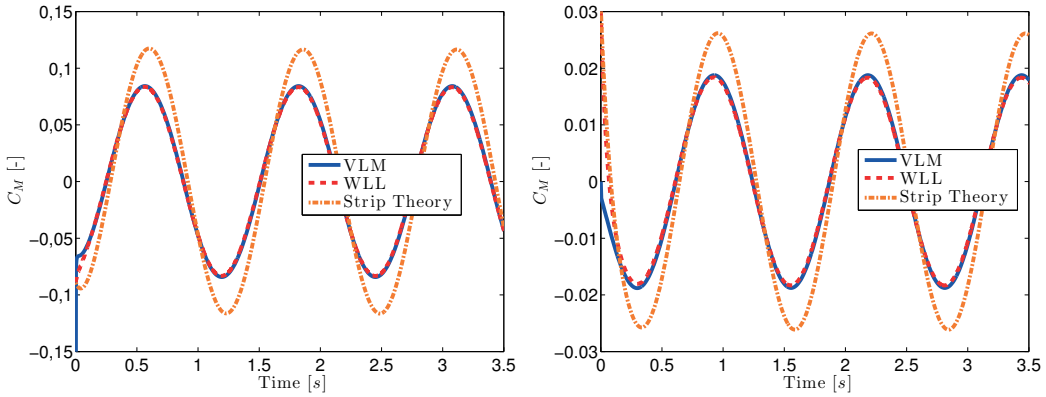

(a) Oscillation in pitch with $A = 5°$ and $k = 0.1$ (b) Oscillation in plunge with $A = 0.1\,[m]$ and $k = 0.1$

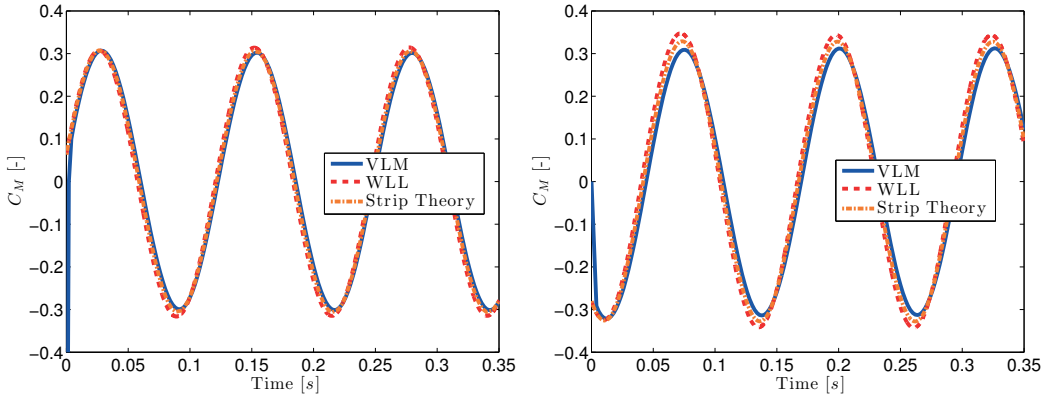

(c) Oscillation in pitch with $A = 5°$ and $k = 0.3$ (d) Oscillation in plunge with $A = 0.1\,[m]$ and $k = 0.3$

FIGURE 5.7: Moment comparison between VLM, WLL and strip theory for a rectangular wing undergoing an oscillation motion.

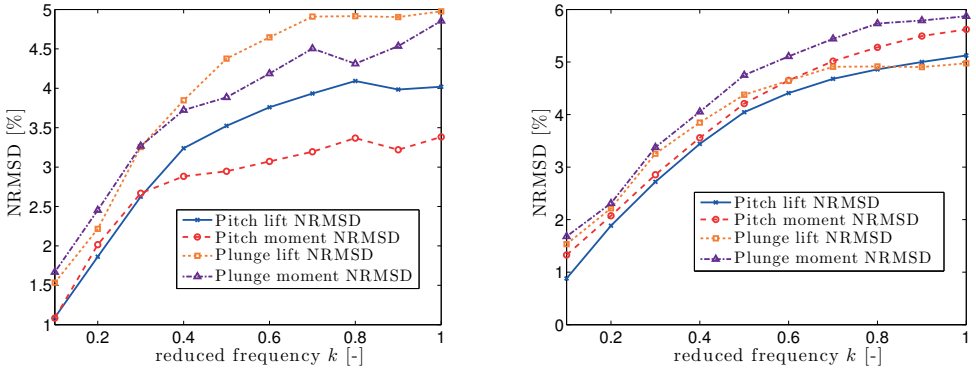

(a) Leading edge (b) Quarter chord

FIGURE 5.8: NRMSD between VLM and WLL aerodynamics responses for a rectangular wing $AR = 6$ undergoing oscillations motion.

in plunge, as detailed in section 5.1.1. The resulting lift and moment responses are shown in figure 5.9. In all cases, the WLL and VLM predictions are in very good agreement, while the strip theory results are highly overestimated in the pitch step

case. Moving the pitch axis to the quarter chord results in equally good agreement between the WLM and VLM aerodynamic load responses.

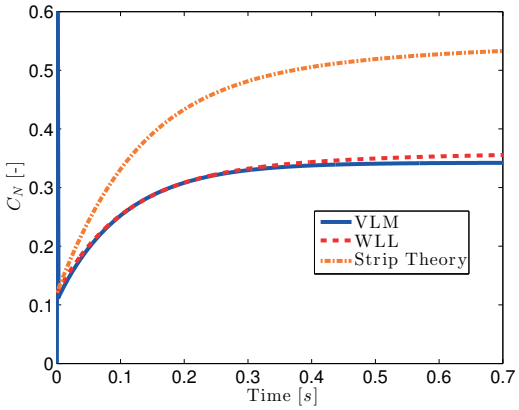

(a) Lift coefficient, pitch step $A = 5°$

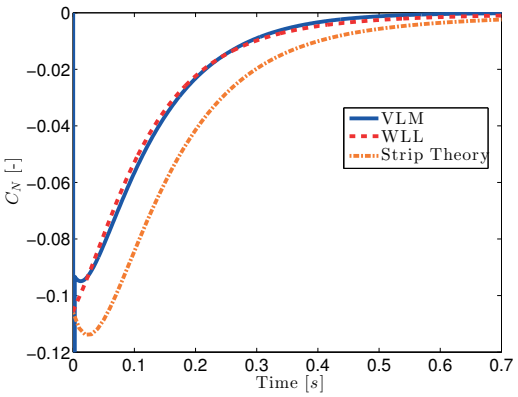

(b) Lift coefficient, plunge step $A = 0.1\,[m]$

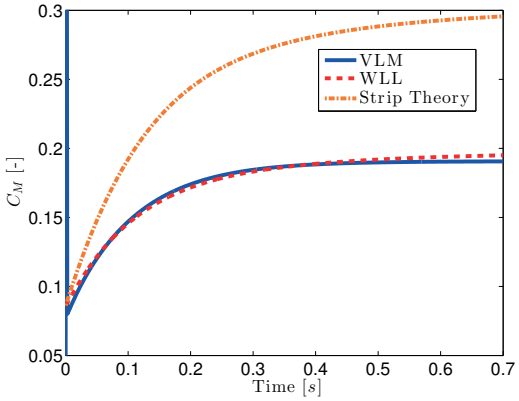

(c) Moment coefficient, pitch step $A = 5°$

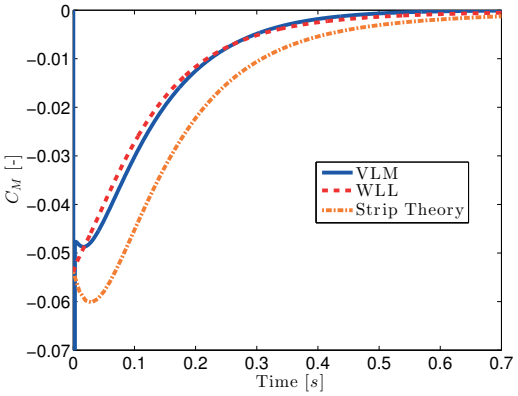

(d) Moment coefficient, plunge step $A = 0.1\,[m]$

FIGURE 5.9: Comparison between VLM, WLL and strip theory for a tapered wing, $AR = 6$, undergoing a step motion

Finally, the WLL and VLM are compared for the case of pitch or plunge sinusoidal oscillations at different reduced frequencies for the tapered wing. The pitch axis is located at the leading edge of the root chord. Figure 5.10(a) plots the variation of the NRMSD values between the two sets of predictions, for increasing k values. It can be seen that in all cases the maximum NRMSD stays below 5%. It is concluded that the WLL approach can predict accurately the aerodynamic load responses for oscillating tapered wings. Moving the pitch axis to the quarter chord results in equally good predictions, as seen in figure 5.10(b).

5.5 Computational cost

The computation times of the WLL and VLM approaches are compared for a step and three sinusoidal oscillations in pitch, with reduced frequencies $k = [0.1, 0.5, 1]$ and a total simulation time $T_f = 1.3$ s. The following parameters have been used for each method :

VLM: There are 15 spanwise and 20 chordwise panels and the time step is $\Delta t = 10^{-3}$. The wake shape is prescribed in order to reduce computational cost.

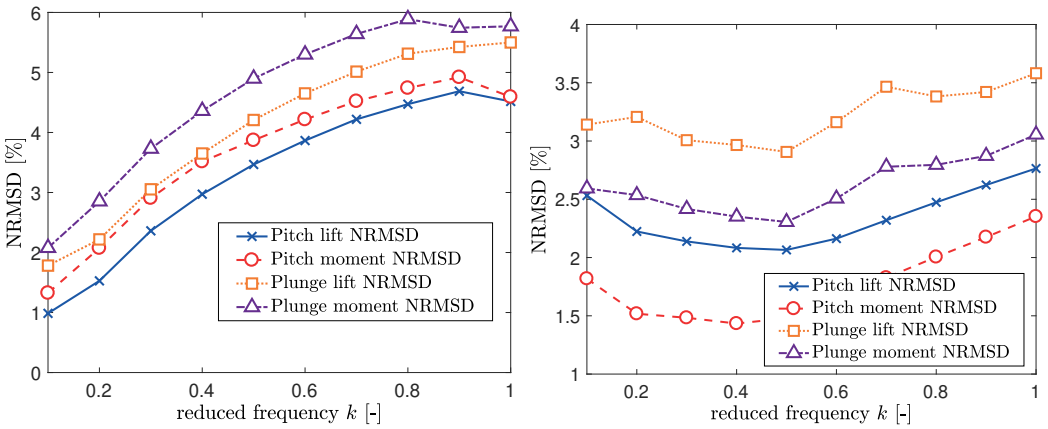

(a) Root leading edge (b) Root quarter chord

FIGURE 5.10: NRMSD between VLM and WLL aerodynamic responses for a tapered wing $AR = 6$ undergoing oscillations motion

WLL: The computation parameters used are 15 strips, a Tolerance $Tol = 10^{-8}$ and an initial Time step $\Delta t = 10^{-3}$ for the Runge-Kutta-Fehlberg 45 algorithm.

All the computations were run on a compuer with a quadcore Intel i7 processor running at 2.5 Ghz, running iOS version 10.9.5.

TABLE 5.1: Computation time comparison between VLM and WLL

Model	step	oscillation $k = 0.1$	oscillation $k = 0.5$	oscillation $k = 1$
VLM	503 $[s]$	504 $[s]$	495 $[s]$	497 $[s]$
WLL	15 $[s]$	36 $[s]$	57 $[s]$	32 $[s]$

Table 5.1 shows that WLL calculation times are much lower than VLM numerical simulations to simulate 1.3 $[s]$ of pitch step or sinusoidal oscillations with reduced frequency $k = [0.1, 0.5, 1]$. The benefit of an adaptative time step for WLL can also be seen as the computation time is lower for cases with low or high reduced frequencies. It should be stressed that the implementation of the two methods is completely different; the WLL is implemented purely in Matlab while the VLM is implemented as a combination of Matlab and C code (mex functions). If the WLL was also implemented using compiled code it would be even faster.

5.6 Aeroelastic test case

In order to further validate the Wagner Lifting Line approach, an aeroelastic test case is presented for a rigid rectangular wing with pitch and plunge degrees of freedom. The flutter speed will be computed as a function of the position of the pitching axis and the wing's aspect ratio using both the Wagner Lifting Line and the Vortex Lattice method.

5.6.1 Aeroelastic equations of motion

The structure simply consists of a rigid wing with two degrees of freedom in pitch and plunge. The structural equations of motion are given by

$$\begin{bmatrix} m_w & S_w \\ S_w & I_w \end{bmatrix} \ddot{\mathbf{q}} + \begin{bmatrix} k_h & 0 \\ 0 & k_\alpha \end{bmatrix} \mathbf{q} = \begin{bmatrix} -L(t) \\ M(t) \end{bmatrix} \tag{5.5}$$

where $\mathbf{q} = [h \ \alpha]^T$, h is the plunge displacement, α the pitch displacement, m_w the mass, S_w the static imbalance around the pitching axis, I_w the moment of inertia around the pitching axis, k_h and k_α are the stiffnesses of the springs providing restoring loads in the plunge and pitch degrees of freedom respectively and $L(t)$ and $M(t)$ are the lift and moment around the pitching axis computed using the VLM or WLL approaches.

The wing is chosen as an aluminum rectangular flat plate with chord $c_0 = 1\,[m]$, thickness $h = 0.005\,[m]$ and span s; the distance between the pitch axis and the mid-chord is x_e. The mass matrix components can then be computed as

$$\begin{aligned} m_w &= \rho_{al} s h c_0 \\ I_w &= \frac{m_w c_0^2}{12} + m_w c_0^2 x_e^2 \\ S_w &= -m_w x_e \end{aligned}$$

where $\rho_{al} = 2300\,[kg/m^3]$ is the density of aluminium. The spring stiffnesses for the two degrees of freedom are chosen such that the uncoupled, wind-off natural frequencies of the system are $f_h = 1\,[hz]$ and $f_\alpha = 5\,[hz]$. The stiffnesses are then given by

$$\begin{aligned} k_h &= m_w \left(2\pi f_h\right)^2 \\ k_\alpha &= I_w \left(2\pi f_\alpha\right)^2 \end{aligned}$$

The normal force $L(t)$ and moment around the pitching axis $M(t)$ are computed from equations 4.6 and 4.8, together with the added mass effects described in expressions 4.20 and 4.21. The integrals are approximated using the trapezoidal rule.

Finally, the complete linear aeroelastic system composed of equations 5.5 and 4.22 can be written in first order form as

$$\dot{\mathbf{x}} = \mathbf{H}(U, x_e)\mathbf{x} \tag{5.6}$$

The aeroelastic system matrix $\mathbf{H}$ is derived in appendix 4.3, while $\mathbf{x}$ represents the system states and is defined as

$$\mathbf{x} = \begin{bmatrix} a_1 & \dots & a_m & \mathbf{z}_1 & \dots & \mathbf{z}_m & \mathbf{q} & \dot{\mathbf{q}} \end{bmatrix}^T \tag{5.7}$$

where a_i is the ith Fourier coefficient, $\mathbf{z}_i$ are the local aerodynamic state variables for the ith strip

$$\mathbf{z}_i = \begin{bmatrix} z_{i,1} & z_{i,2} & z_{i,3} & z_{i,4} & z_{i,5} & z_{i,6} \end{bmatrix}$$

$\mathbf{q} = [h \ \alpha]$ and m is the number of strips. Consequently, the total number of states is $7m{+}4$.

Finally, the WLL flutter solution is obtained by computing the eigenvalues of matrix $\mathbf{H}(U, x_e)$ as a function of the airspeed U. An indirect search procedure is employed to pinpoint the airspeed at which one pair of complex conjugate eigenvalues

become purely imaginary, which is the definition of the flutter speed. The number of strips used to estimate matrice $\mathbf{H}(U, x_e)$ is $m = 20$ and the flutter solution is obtained for several values of the position of the pitch axis x_e.

The VLM flutter solution is obtained using the modal frequency domain version of the method, as detailed in [77]. Rigid body modes are chosen, one for the plunge and one for the pitch. The mode shapes are given by

$$\begin{aligned} w_h(x,y) &= 1 \\ w_\alpha(x,y) &= x \end{aligned}$$

where $w_h(x,y)$ is the plunge mode shape and $w_\alpha(x,y)$ the pitch mode shape. The elements of the mass matrix are then obtained from

$$\begin{aligned} m_w &= \rho_{al} h \int_0^c \int_0^y w_h^2(x,y)\mathrm{d}x\mathrm{d}y \\ I_w &= \rho_{al} h \int_0^c \int_0^y w_\alpha^2(x,y)\mathrm{d}x\mathrm{d}y \\ S_w &= \rho_{al} h \int_0^c \int_0^y w_h(x,y) w_\alpha(x,y)\mathrm{d}x\mathrm{d}y \end{aligned}$$

The resulting flutter problem is of the form

$$\left(\left(\frac{kU}{b} \right)^2 \mathbf{A}\ddot{\mathbf{q}} + \mathbf{E}\mathbf{q} - \rho U^2 \mathbf{Q}(k) \right) \mathbf{q}(k) = 0 \tag{5.8}$$

where $\mathbf{A}_s$ is the structrural mass matrix, $\mathbf{E}_s$ is the structural stiffness matrix and $\mathbf{Q}(k)$ is the frequency-depended generalised aerodynamic force matrix generated by the VLM approach. The flutter problem is solved using the $p-k$ method.

5.6.2 Results

The resulting flutter speed and frequency values are plotted against the position of the pitch axis in Figure 5.11 for two aspect ratios : $AR = 4$ and $AR = 10$. Figure 5.11(a) plots the flutter airspeeds and shows that the VLM and WLL predictions are in good agreement with each other for both aspect ratios. Figure 5.11(b) plots the flutter frequency predictions; the agreement is still very good as the highest frequency discrepancy is of the order of 5%. It can be concluded that the Wagner lifting line method can predict accurately the flutter of a wing with a finite span.

5.7 Conclusions

The WLL method results in a closed form, state-space representation of the unsteady aerodynamic loads acting on finite rectangular and tapered wings of different aspect ratios, under attached incompressible flow conditions. The technique combines Wagner's 2D unsteady lift theory, Prandtl's lifting line theory, the unsteady Kutta-Joukowsky theorem and the added mass terms from Theodorsen's analysis. Sample simulations on wings with and without taper have shown very good agreement between the WLL predictions and VLM simulation results. The method can also be readily applied to wings with twist and camber. Sweep is more problematic, since lifting line theory has to be modified in order to work in the presence of sweep. This modification will be addressed in future work.

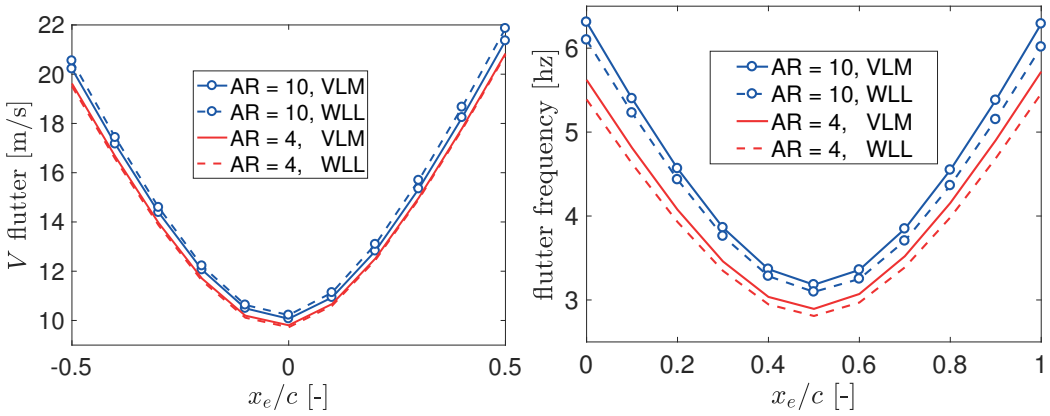

(a) Flutter speed

(b) Flutter frequency

FIGURE 5.11: Comparison of flutter with aeroelastic axis for 3D wing, computed with vortex lattices (dashed line) and Wagner lifting line (solid)

The VLM approach is still more general than the WLL technique, as it can easily represent sweep. The advantage of WLL is the fact that the resulting aerodynamic loads are written in state space form, as functions of the structural and aerodynamic states. They can therefore be easily included in aeroelastic and flight dynamic calculations. In contrast, the VLM or DLM techniques result in time-marching simulations or, if using a modal frequency domain technique, in equation 5.8, which is a hybrid time-frequency domain equation that must be transformed to the time domain in order to carry out aeroservoelastic calculations. In the present examples the wings were rigid with discrete degrees of freedom but flexible wings with generalised modes can also be treated. Finally, the WLL calculations are significantly faster than time-domain VLM numerical simulations.

Chapter 6

Conclusion

6.1 Summary of contribution

The main achievements of this thesis are the following:

- The adaptation of the Leishman-Beddoes model to low Reynolds numbers. This was done by implementing Wagner theory as the incompressible attached flow solver, adapting the Sheng et al dynamic stall onset criterion, and estimating the values of the steady and unsteady model parameters from experimental results.
- The creation of a full experimental data set for a flat plate, a NACA0012 wing, and a NACA0018 wing, all three undergoing different levels of dynamic stall. These experimental results were used to calibrate and validate the modified Leishman-Beddoes model developed during the course of the current work.
- The formulation of a the Wagner Liftin Line model, a 3D unsteady attached flow lift and moment computation model. It was made by combining the unsteady 2D loads predicted by Wagner thoery with Prandtl's lifting line approach, thanks to unsteady Kutta-Joukowsky theorem. The model was validated through comparisons to the predictions of a vortex lattice solver for impulsive and oscillatory motions.

For all three wings tested experimentally, the modified Leishman-Beddoes model gave better aerodynamic load predictions than the original formulation for low to medium values of the reduced pitch rate. For the highest values of the reduced pitch rate neither model resulted in fully satisfactory load predictions. Nevertheless, the present work demonstrated that the variation of the dynamic stall angles at low reduced pitch rates is represented better by a continuous quadratic function than the discontinuous piecewise linear function proposed by Sheng et al, at least for the range of Reynolds numbers investigated in this work. This is one of the major contributions of the present thesis to the understanding of dynamic stall at low Reynolds numbers. From a mathematical point of view, the use of cubic splines to represent the steady lift curve that is proposed in this thesis results in better curve fits of both the lift and the position of the separation point than the exponential functions used in the original Leishman-Beddoes model.

The Wagner Lifting Line model is an unsteady lifting line approach that models the trailing vortices as infinitely long, ignoring the spanwise vortex segments shed into the wake. This modelling methodology is different from the standard unsteady lifting line techniques that calculate the downwash induced by vortex rings instead of trailing vortices only (see for example Jones [61]). This simplification was chosen consciously in order to allow easy application of the technique to non-elliptical wing planforms. The resulting aerodynamic load predictions are in very good agreement with the higher-fidelity VLM results despite this simplification. The reason for this

is that Wagner's 2D theory already contains the effect of the spanwise shed vortex segments in its wake model. Jones [94] had to subtract the 2D shed vorticity from the downwash calculation, precisely because he included the spanwise trailing vortex in his model. Aeroelastic calculations based on the WLL yielded very good flutter predictions, a fact that strengthens the case for ignoring the trailing wake segments in unsteady lifting line calculations.

6.2 Suggestion for further work

The present work resulted in a modified Leishman-Beddoes model, in order to compute the loads acting on an airfoil undergoing dynamic stall and the Wagner lifting Line model to represent the unsteady 3D aerodynamic loads on a finite wing with attached flow. The next step would be to explore ways to build a 3D dynamic stall model. The main idea is to use to take inspiration from the 2D LB model and add the detached flow effects on top of the 3D attached loads computed with the Wagner Lifting Line method. This is no trivial task since it would require to determine whether dynamic stall occurs at each spanwise position separately and to follow the spanwise variation of the positions of both the trailing edge separation and the leading edge vortex.

The development of such a 3D dynamic stall model would imperatively require experimental data for calibration and validation. Unsteady pressure data should be measured at several chordwise and spanwise positions, a requirement that has limited the number and quality of such experiments available in the literature. Nevertheless, apart from calibrating and validating models, such data could be used to obtain new insights into the phenomenon of dynamic stall on finite wings. Finally, the same experimental setup could be tested for small oscillation amplitudes in order to validate experimentally the attached flow aerodynamic load predictions obtained from the WLL and VLM approaches.

Another avenue for further research concerns the modified Leishman-Beddoes model the values of the B1 and B2 coefficients in equations 2.84 and 2.85 are assumed to be constant with pitch rate. It is believed that developing a pitch-rate dependence model for these coefficients would significantly improve the performance of the model at high pitch rates. Furthermore, the possibility of including the laminar separation bubble occurring in steady flow at low angles of attack in the model should be explored.

Appendix A

Publication from this thesis

- Boutet, J., & Dimitriadis, G. (2018). Unsteady Lifting Line Theory Using the Wagner Function for the Aerodynamic and Aeroelastic Modeling of 3D Wings. Aerospace, 5(3), 92.
- Boutet, J., Dimitriadis, G., & Amandolese, X. (2020). A modified Leishman-Beddoes model for airfoil sections undergoing dynamic stall at low Reynolds numbers. Journal of Fluids and Structures, 93, 102852.
- Boutet, J., Dimitriadis, G., & Amandolese, X. (2017, June). Dynamic stall onset variation with reduced frequency for three stall mechanisms. In Proceedings of the International Forum on Aeroelasticity and Structural Dynamics, IFASD 2017.
- Boutet, J., & Dimitriadis, G. (2017). Unsteady lifting line theory using the Wagner function. In Proceedings of the 55th AIAA Aerospace Sciences Meeting (pp. AIAA-2017). AIAA.

Appendix B

Full models comparison

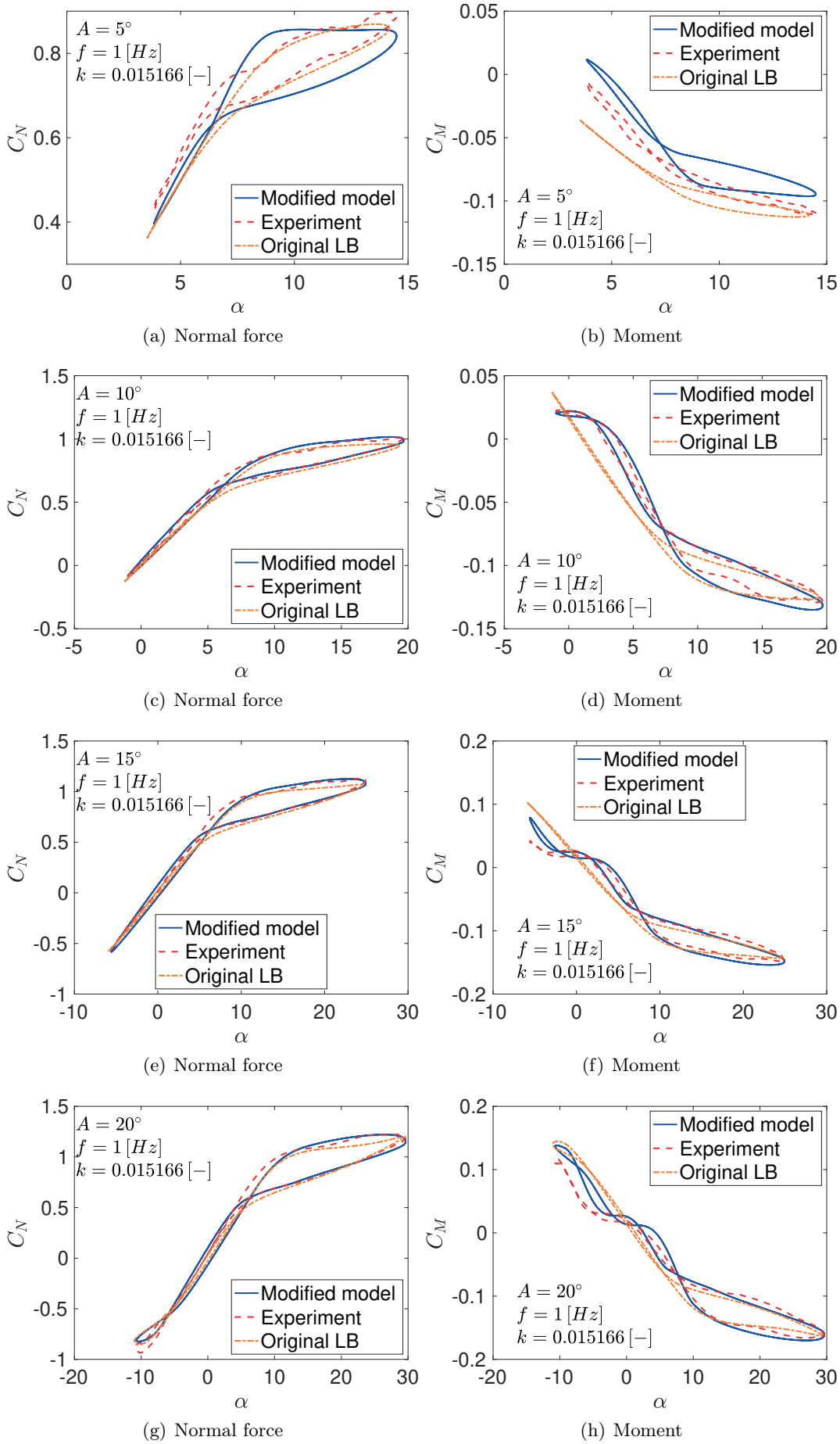

(a) Normal force (b) Moment

(c) Normal force (d) Moment

(e) Normal force (f) Moment

(g) Normal force (h) Moment

FIGURE B.1: Comparison between the modified LB model and experimental results for the flat plate with $f = 1$ Hz.

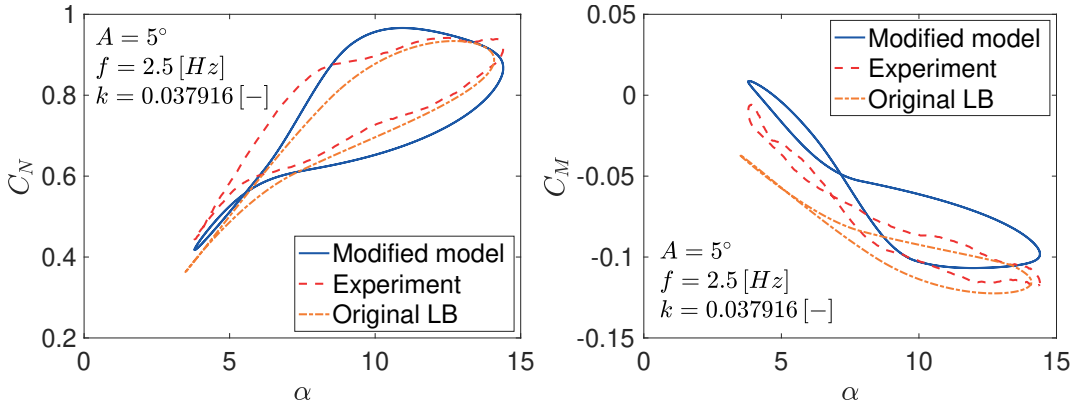

(a) Normal force (b) Moment

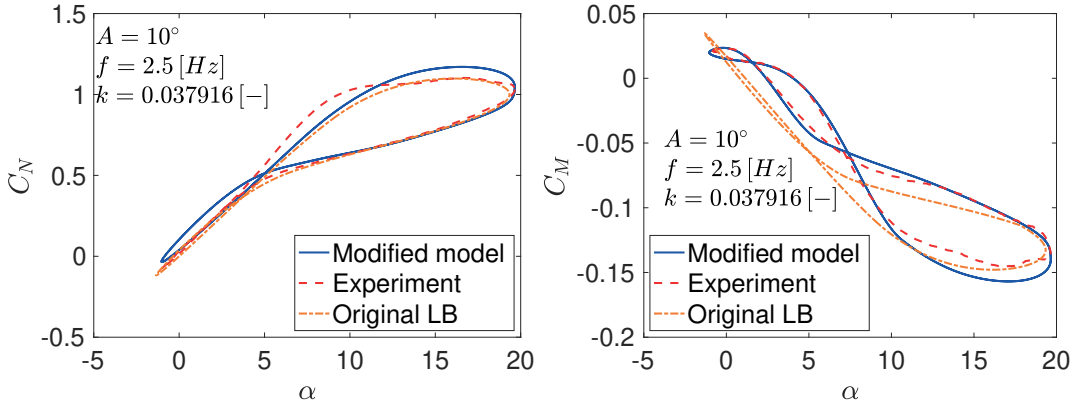

(c) Normal force (d) Moment

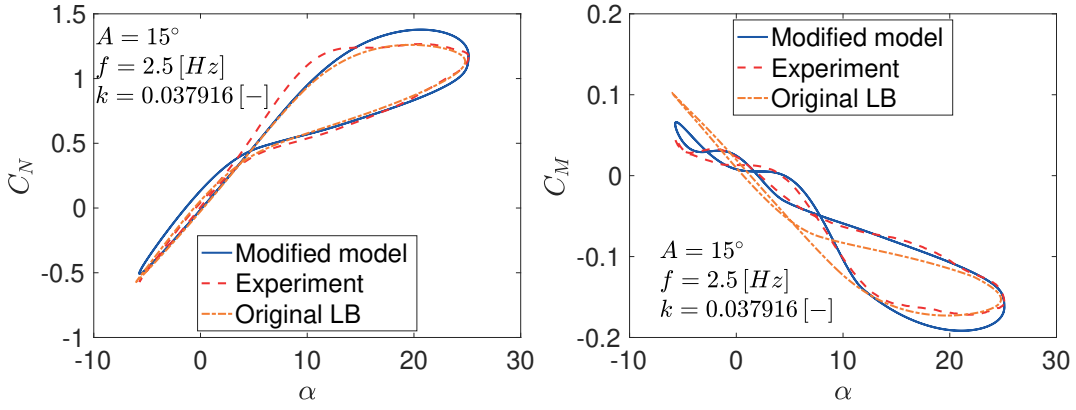

(e) Normal force (f) Moment

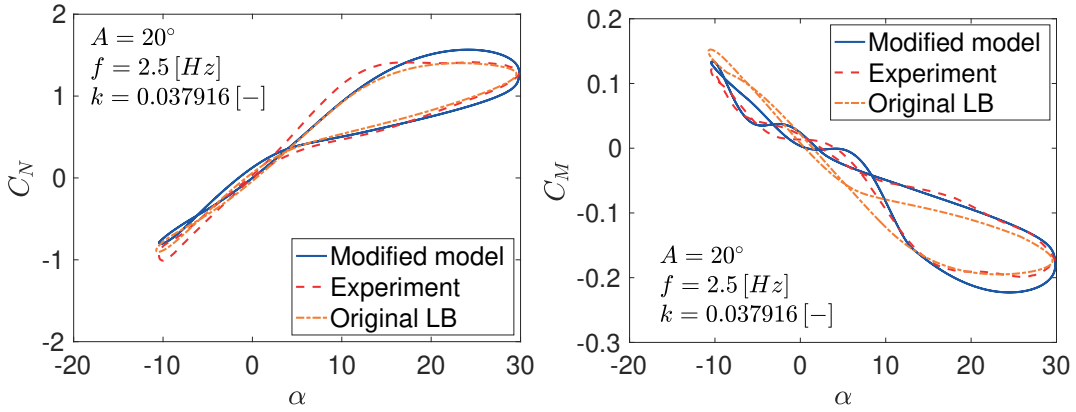

(g) Normal force (h) Moment

FIGURE B.2: Comparison between the modified LB model and experimental results for the flat plate with $f = 2.5$ Hz.

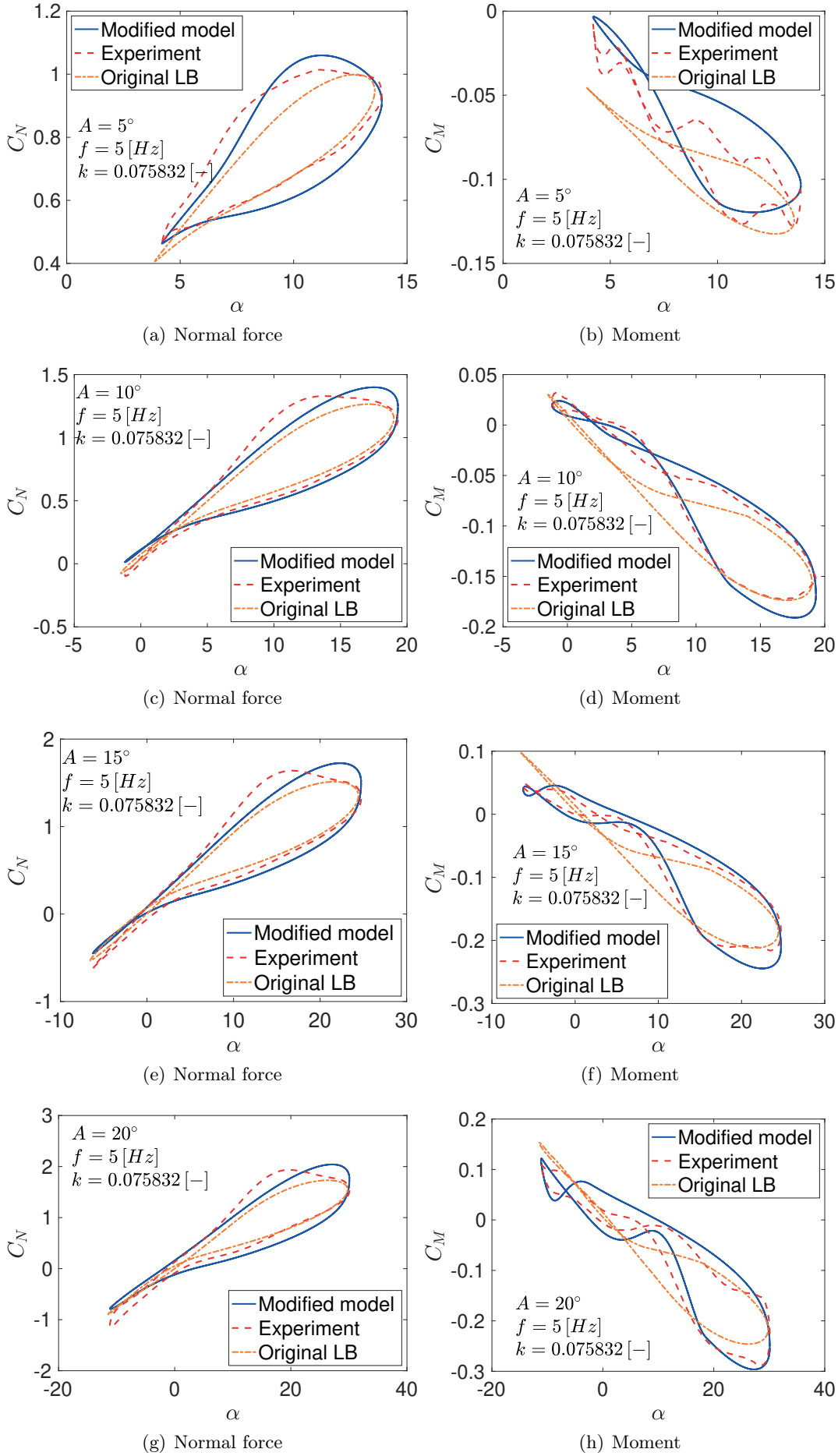

(a) Normal force (b) Moment

(c) Normal force (d) Moment

(e) Normal force (f) Moment

(g) Normal force (h) Moment

FIGURE B.3: Comparison between the modified LB model and experimental results for the flat plate with $f = 5$ Hz.

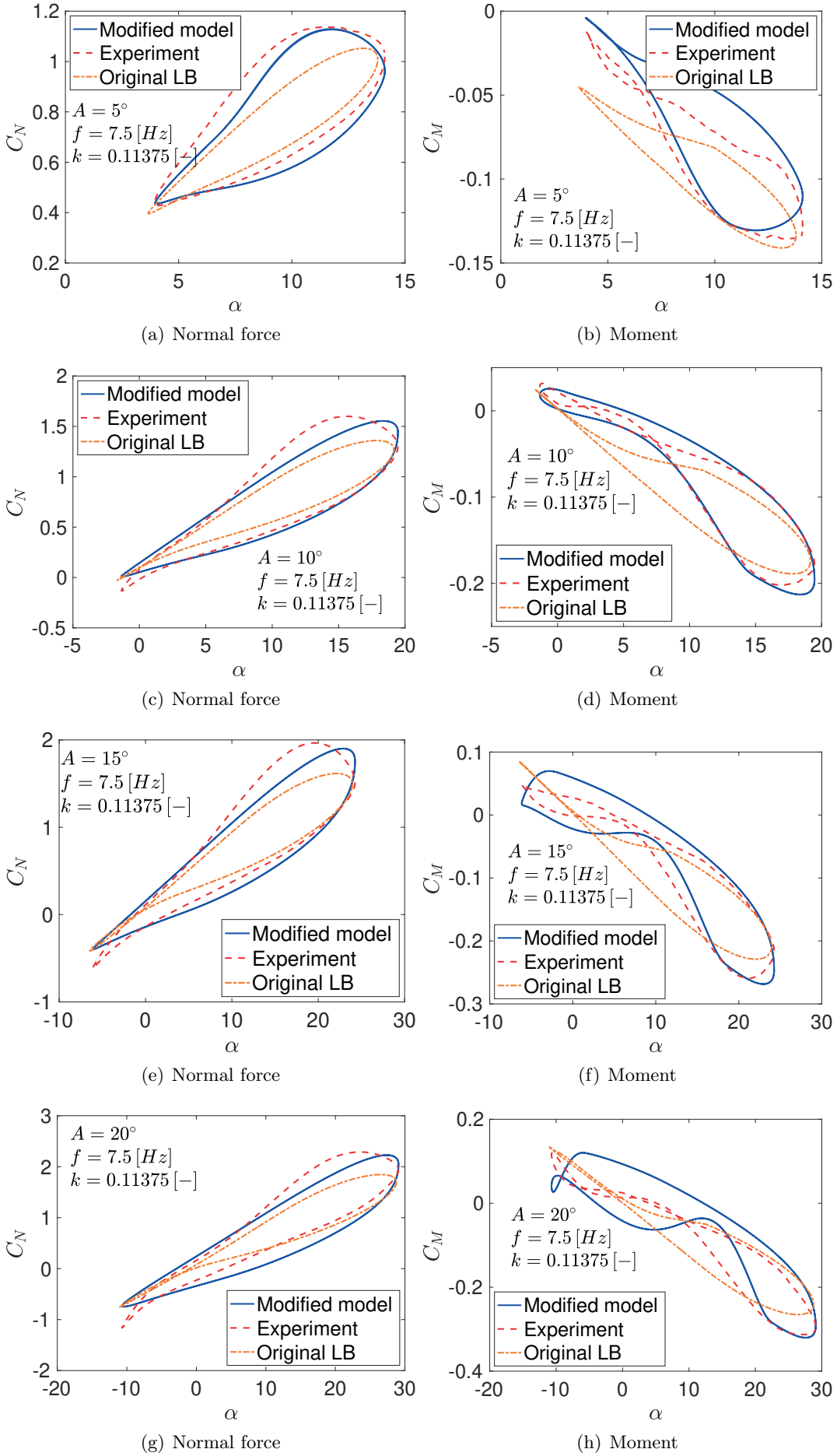

(a) Normal force (b) Moment

(c) Normal force (d) Moment

(e) Normal force (f) Moment

(g) Normal force (h) Moment

FIGURE B.4: Comparison between the modified LB model and experimental results for the flat plate with $f = 7.5$ Hz.

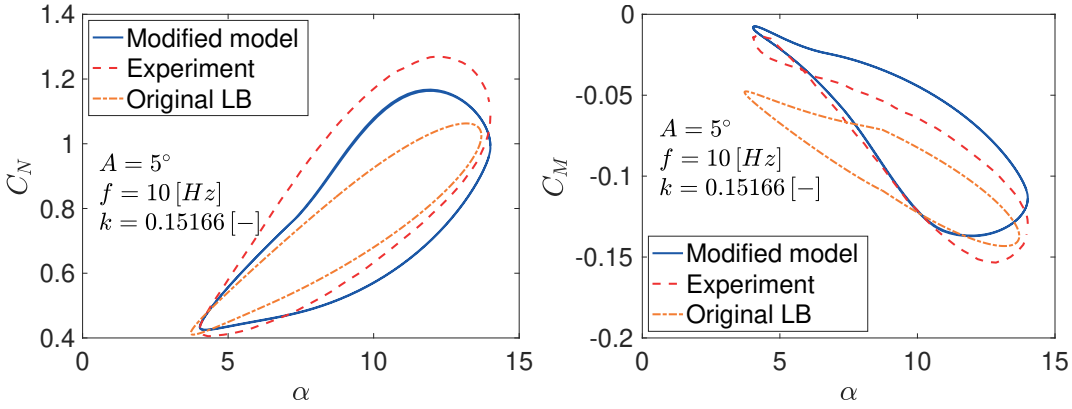

(a) Normal force

(b) Moment

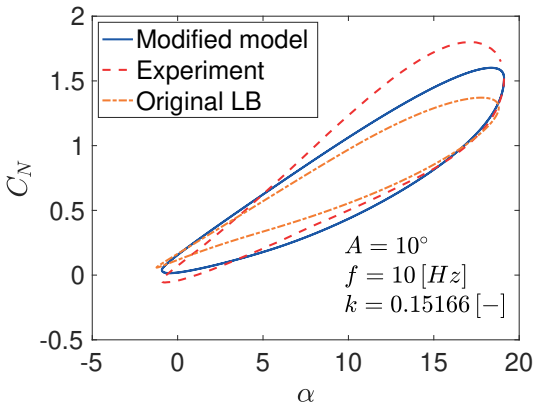

(c) Normal force

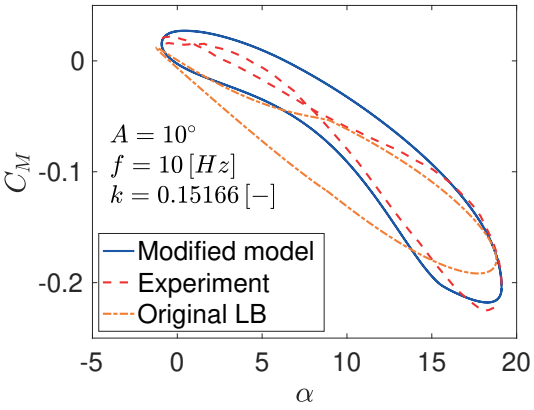

(d) Moment

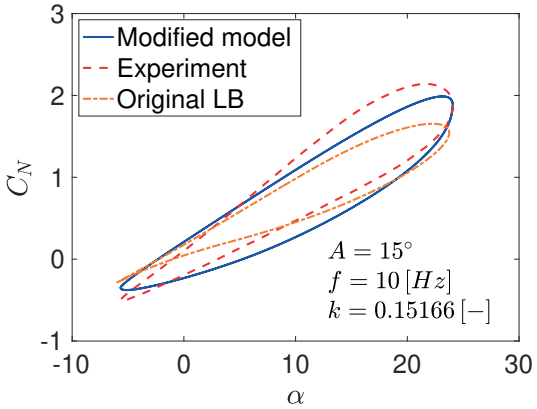

(e) Normal force

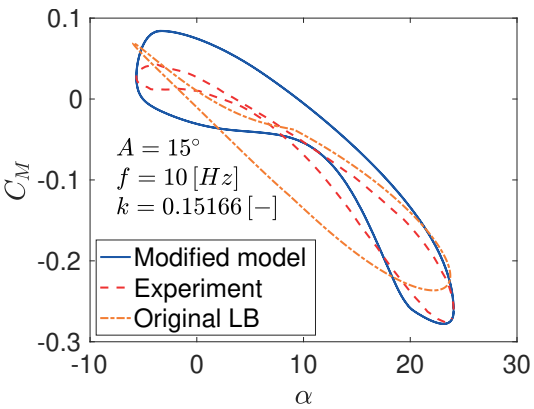

(f) Moment

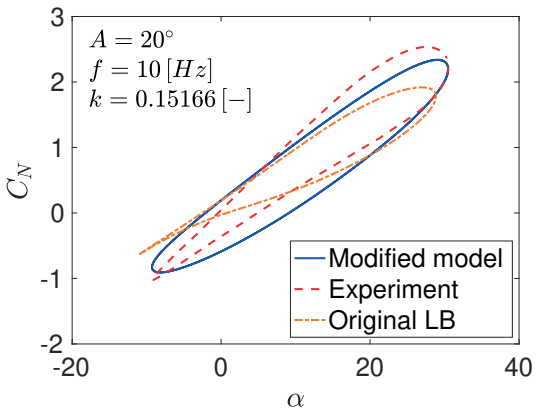

(g) Normal force

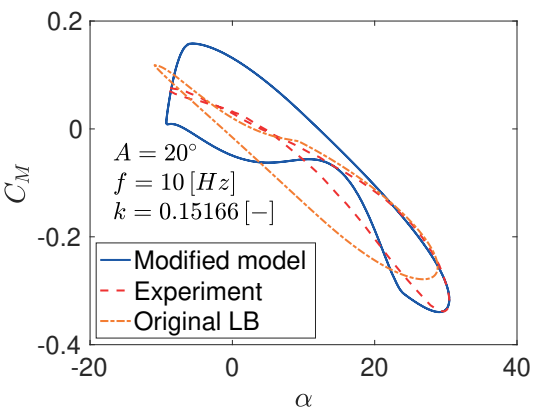

(h) Moment

FIGURE B.5: Comparison between the modified LB model and experimental results for the flat plate with $f = 10$ Hz.

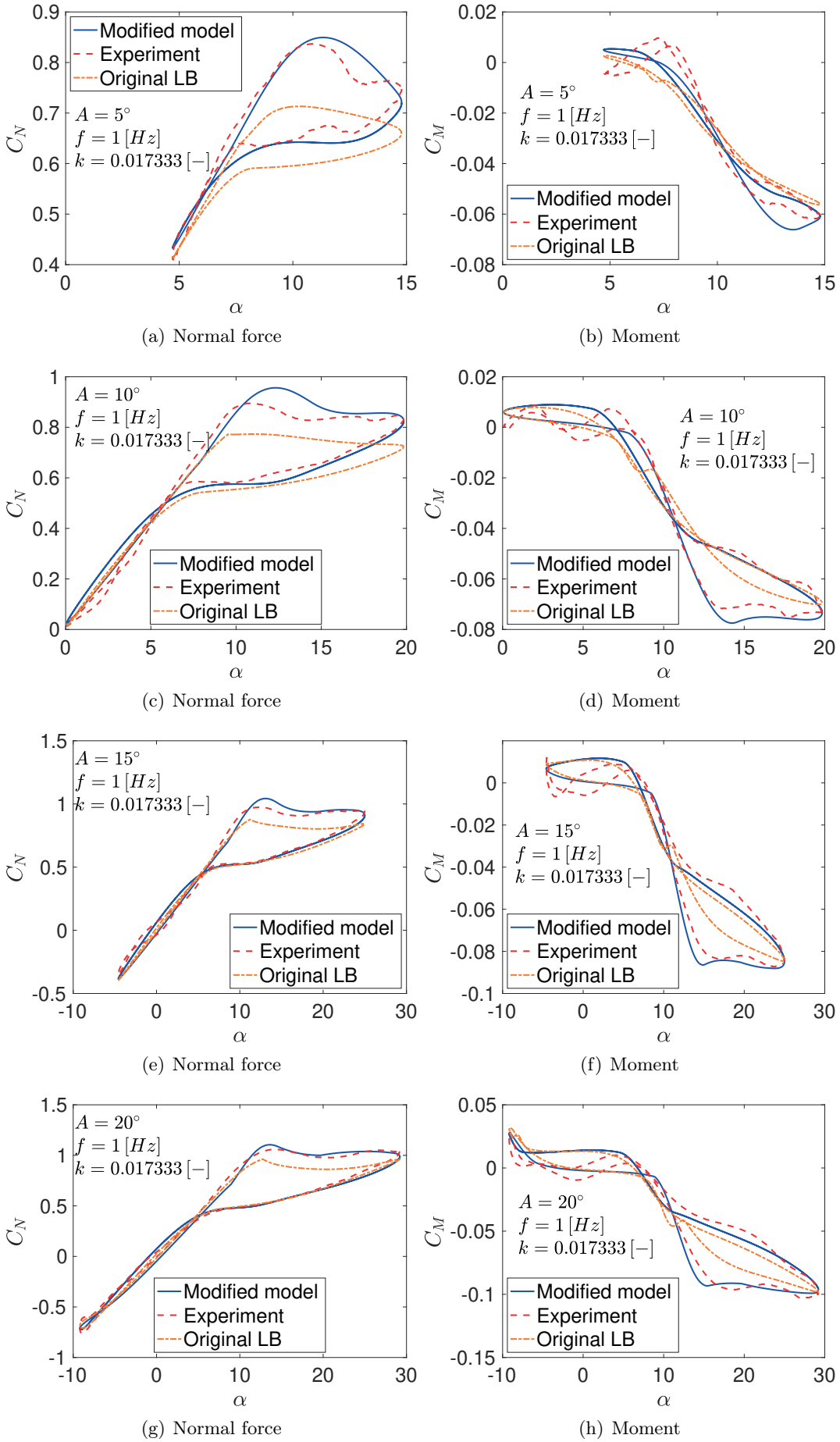

(a) Normal force (b) Moment

(c) Normal force (d) Moment

(e) Normal force (f) Moment

(g) Normal force (h) Moment

FIGURE B.6: Comparison between the modified LB model and experimental results for the NACA0012 with $f = 1$ Hz.

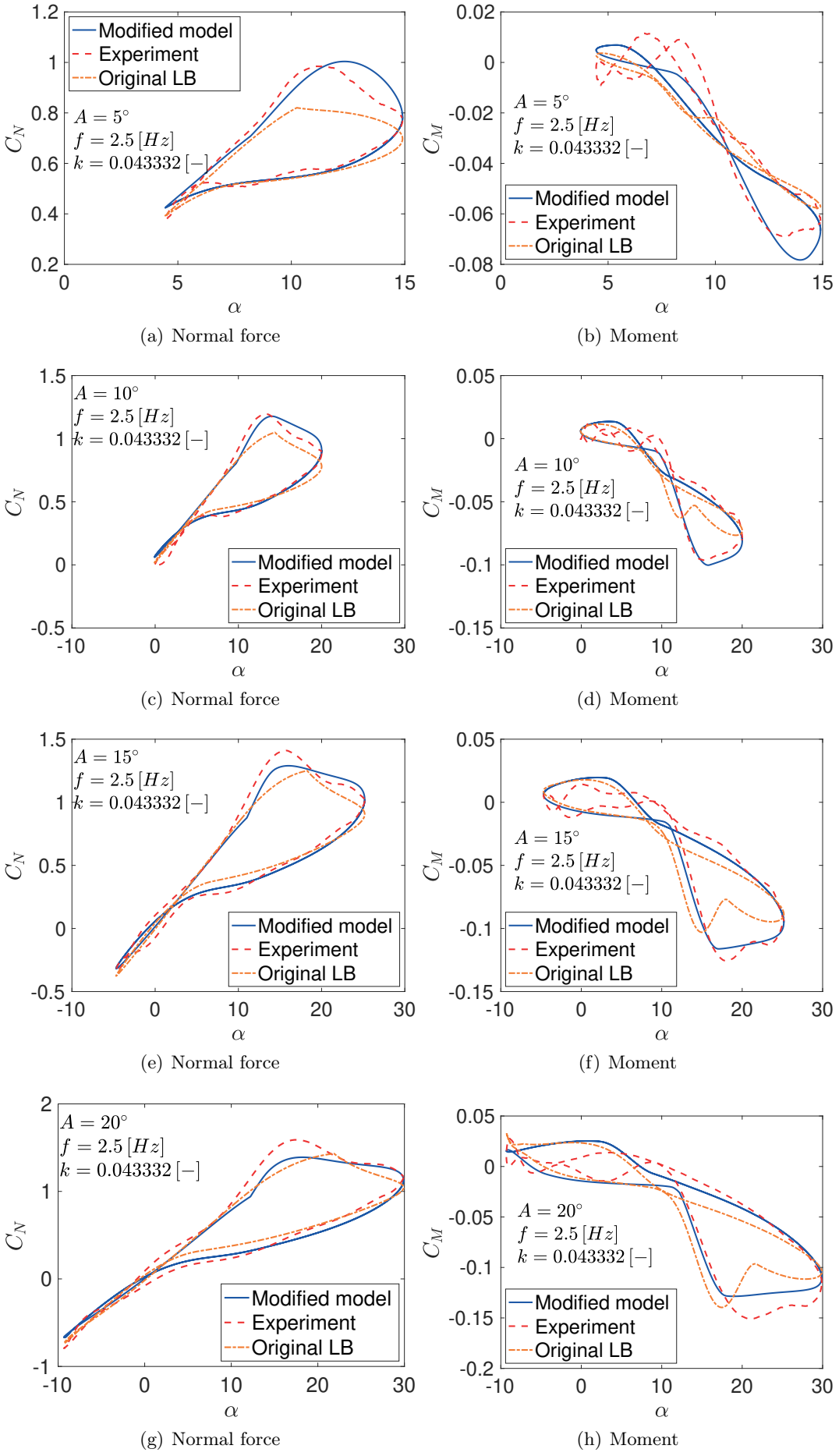

(a) Normal force (b) Moment

(c) Normal force (d) Moment

(e) Normal force (f) Moment

(g) Normal force (h) Moment

FIGURE B.7: Comparison between the modified LB model and experimental results for the NACA0012 with $f = 2.5$ Hz.

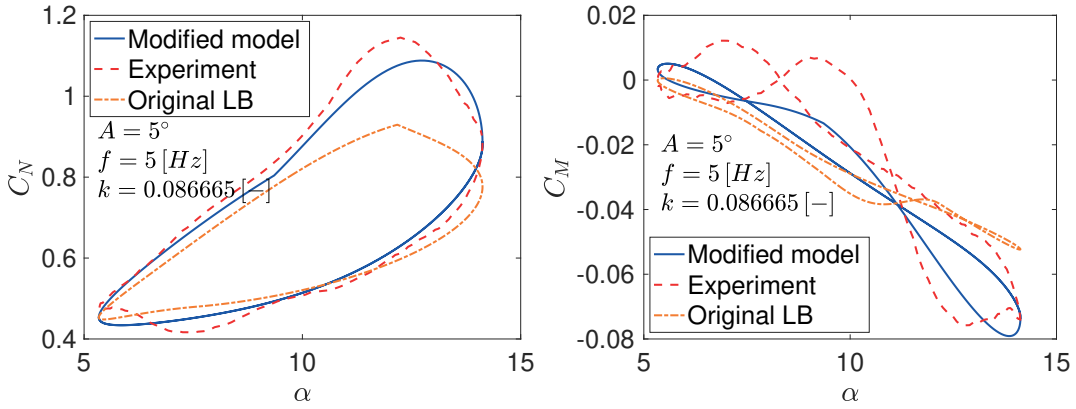

(a) Normal force

(b) Moment

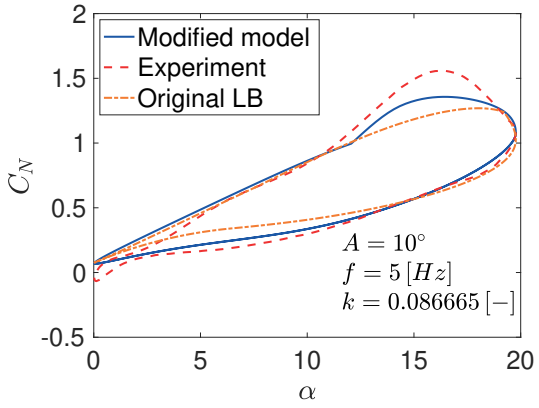

(c) Normal force

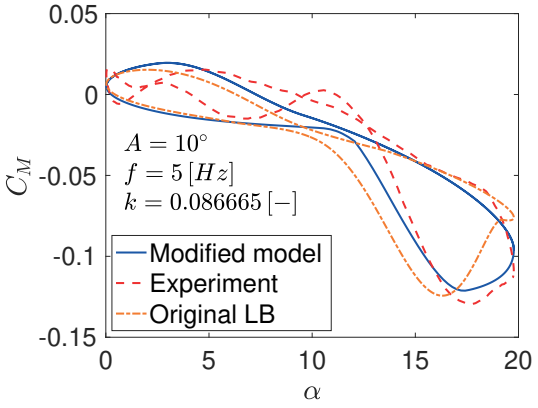

(d) Moment

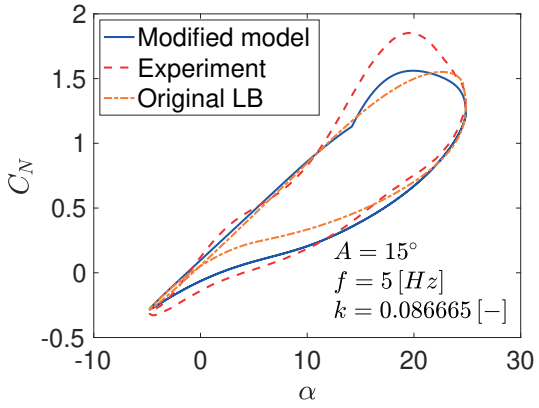

(e) Normal force

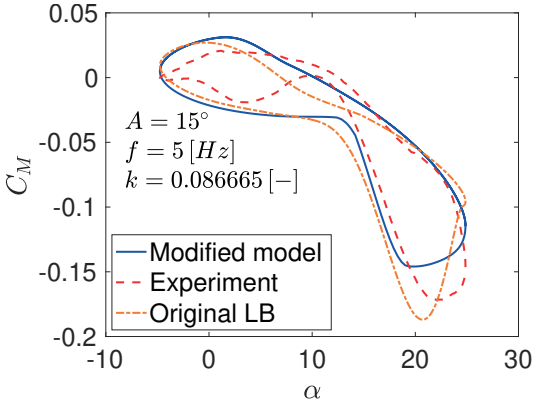

(f) Moment

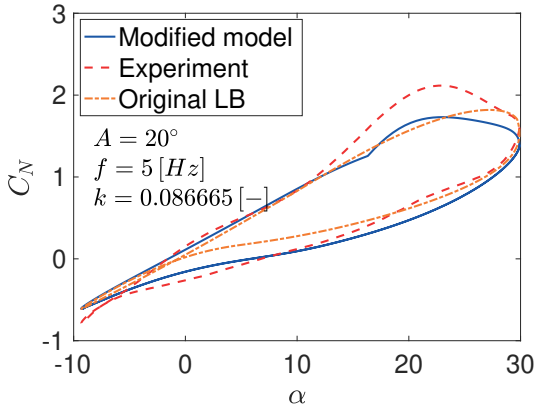

(g) Normal force

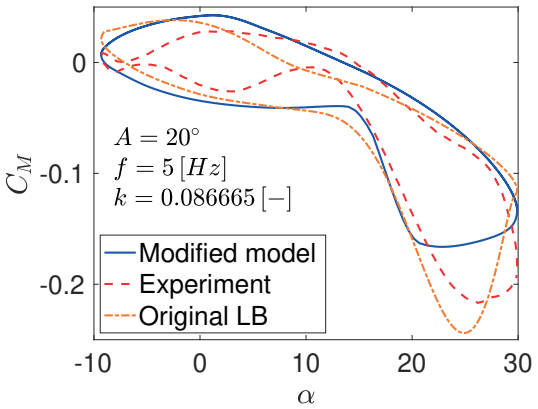

(h) Moment

FIGURE B.8: Comparison between the modified LB model and experimental results for the NACA0012 with $f = 5$ Hz.

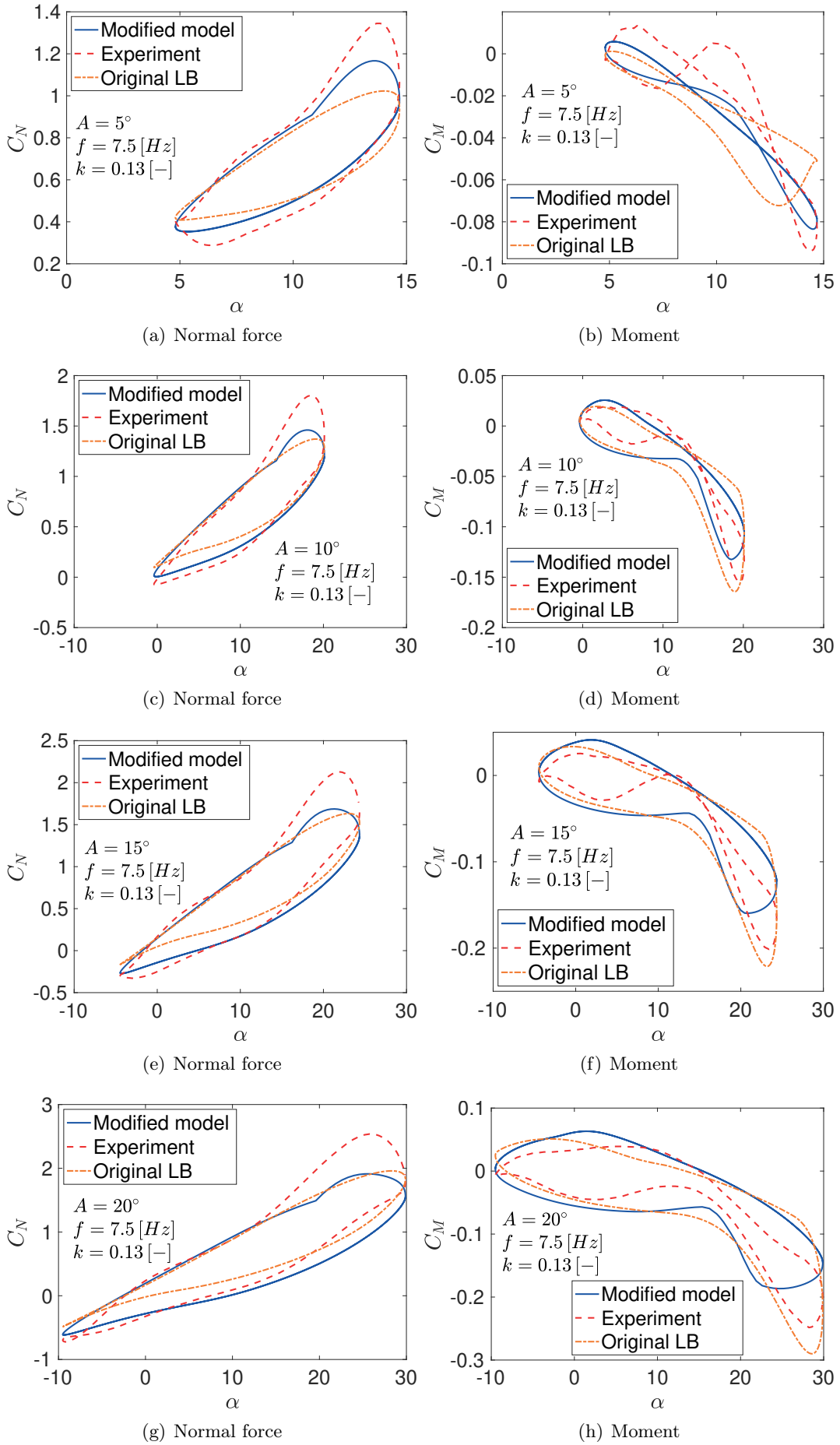

(a) Normal force (b) Moment

(c) Normal force (d) Moment

(e) Normal force (f) Moment

(g) Normal force (h) Moment

FIGURE B.9: Comparison between the modified LB model and experimental results for the NACA0012 with $f = 7.5$ Hz.

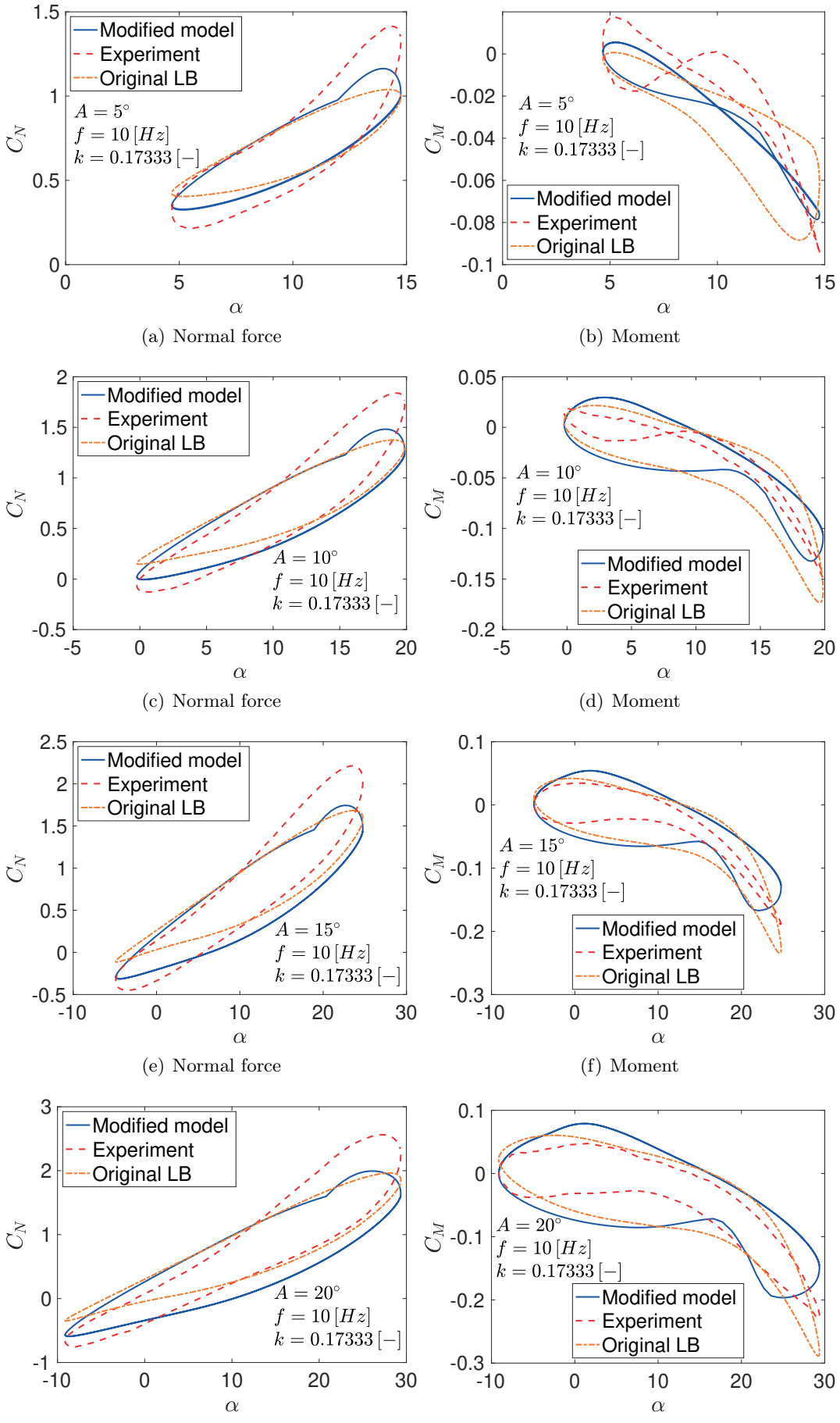

(a) Normal force (b) Moment

(c) Normal force (d) Moment

(e) Normal force (f) Moment

(g) Normal force (h) Moment

FIGURE B.10: Comparison between the modified LB model and experimental results for the NACA0012 with $f = 10$ Hz.

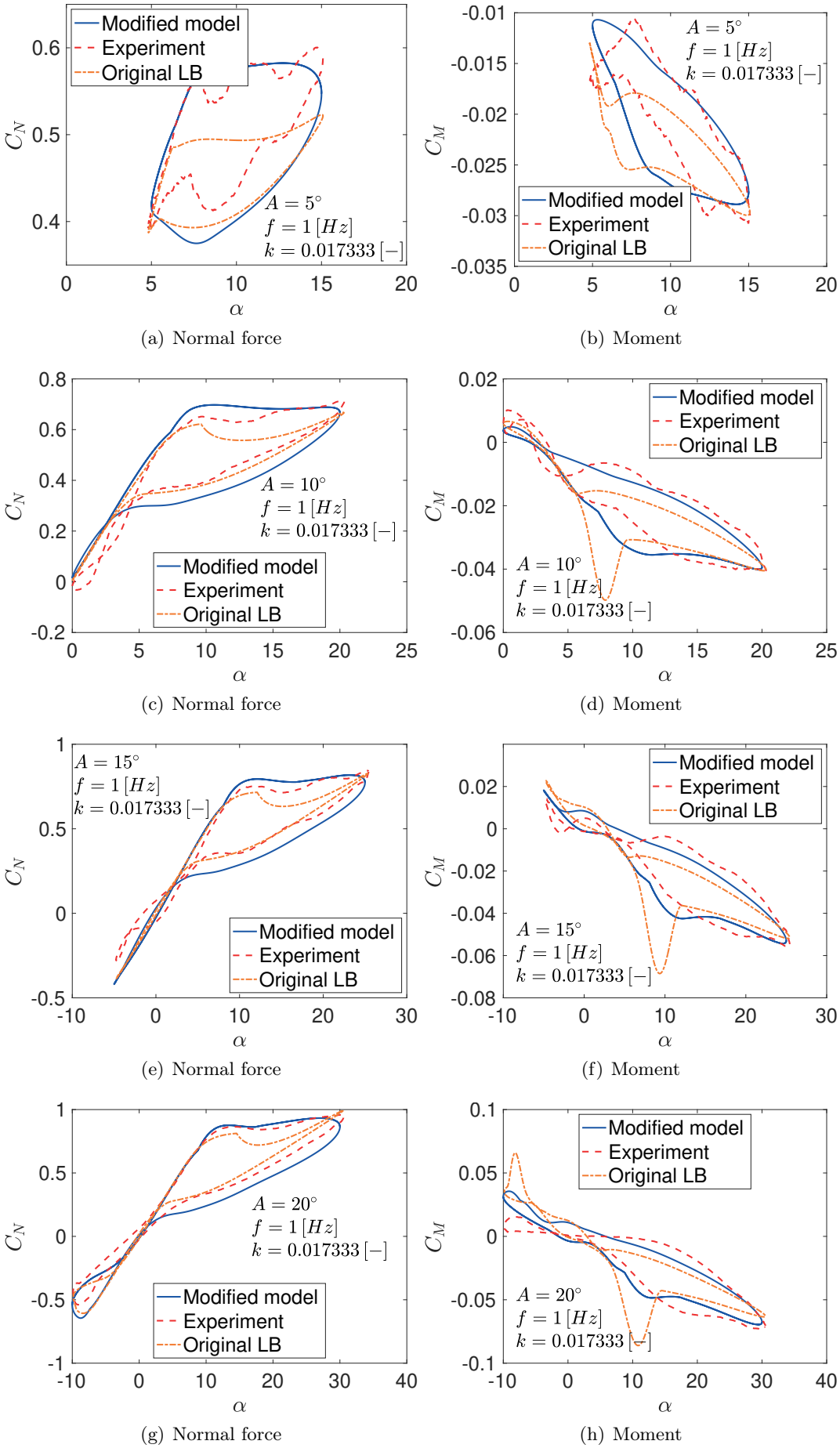

(a) Normal force (b) Moment

(c) Normal force (d) Moment

(e) Normal force (f) Moment

(g) Normal force (h) Moment

FIGURE B.11: Comparison between the modified LB model and experimental results for the NACA0018 with $f = 1$ Hz..

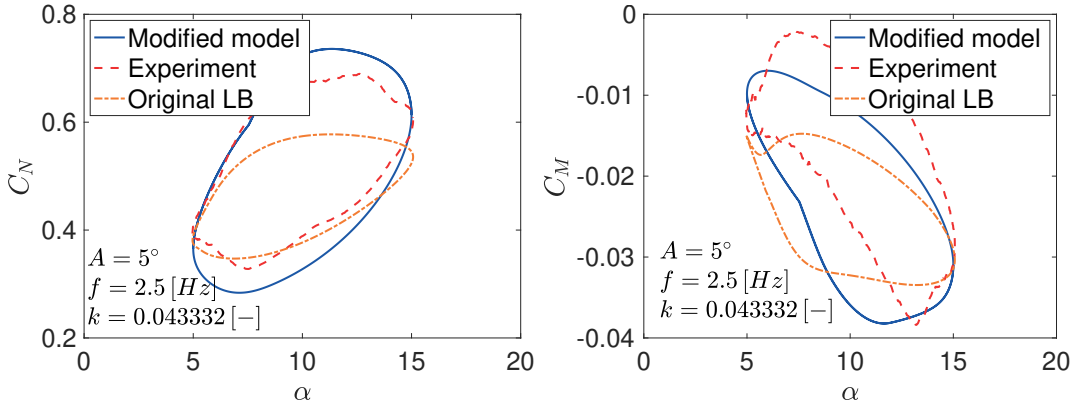

(a) Normal force

(b) Moment

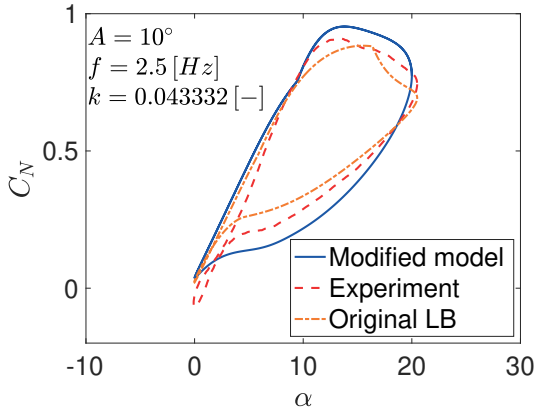

(c) Normal force

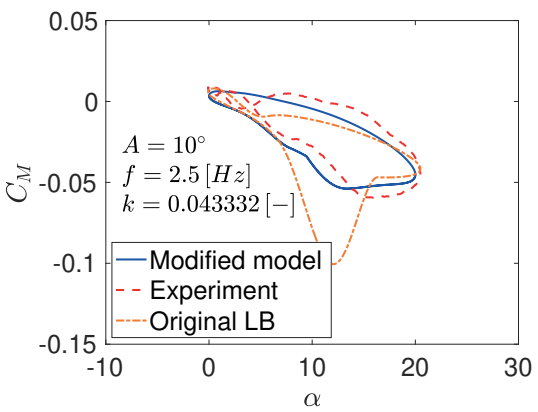

(d) Moment

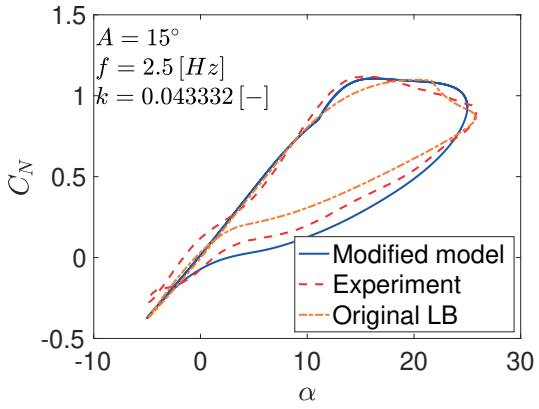

(e) Normal force

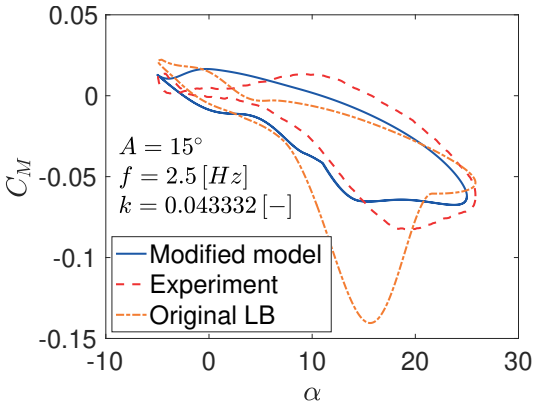

(f) Moment

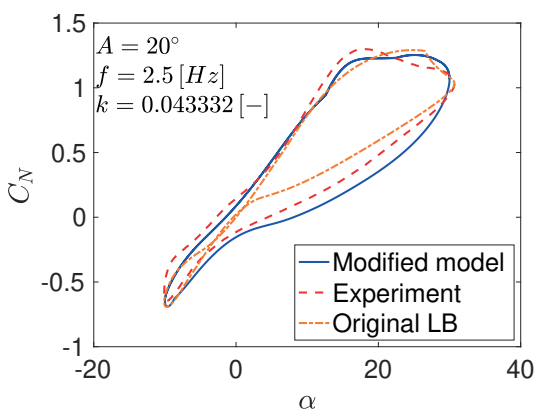

(g) Normal force

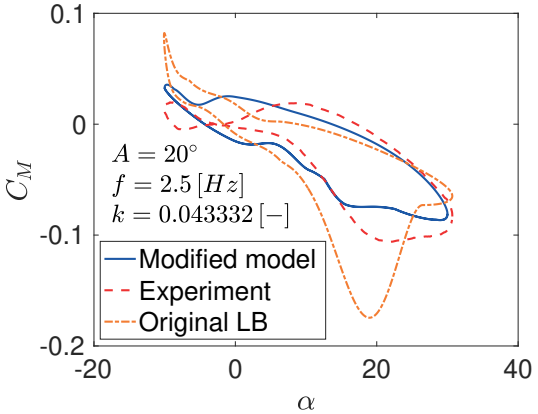

(h) Moment

FIGURE B.12: Comparison between the modified LB model and experimental results for the NACA0018 with $f = 2.5$ Hz.

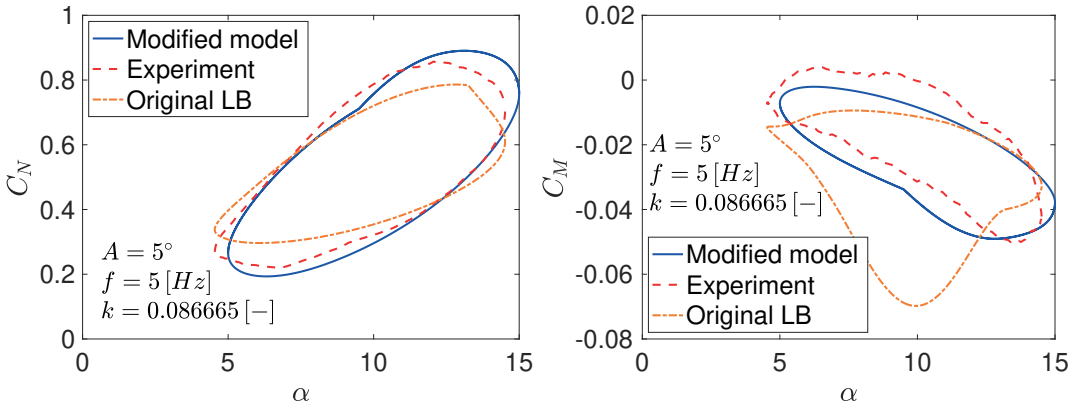

(a) Normal force

(b) Moment

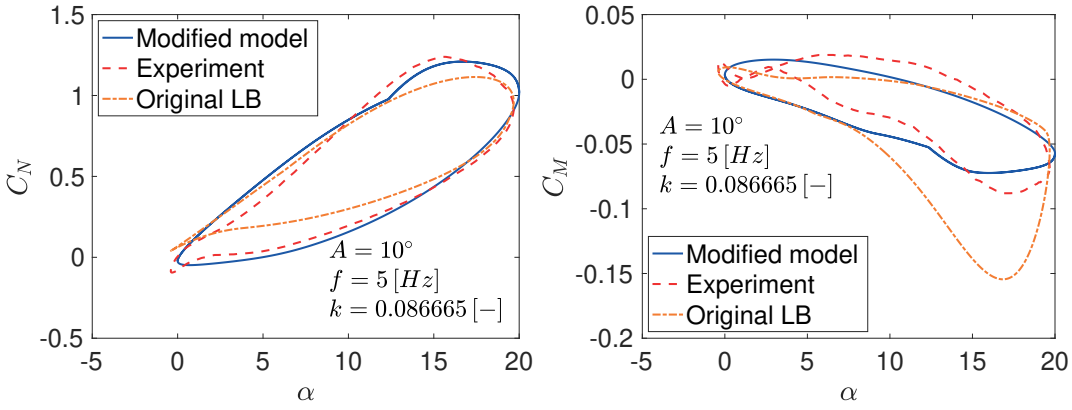

(c) Normal force

(d) Moment

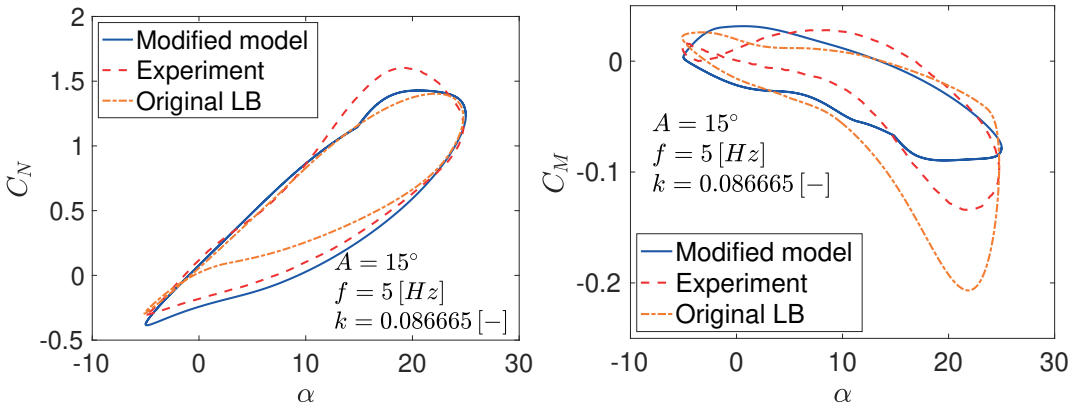

(e) Normal force

(f) Moment

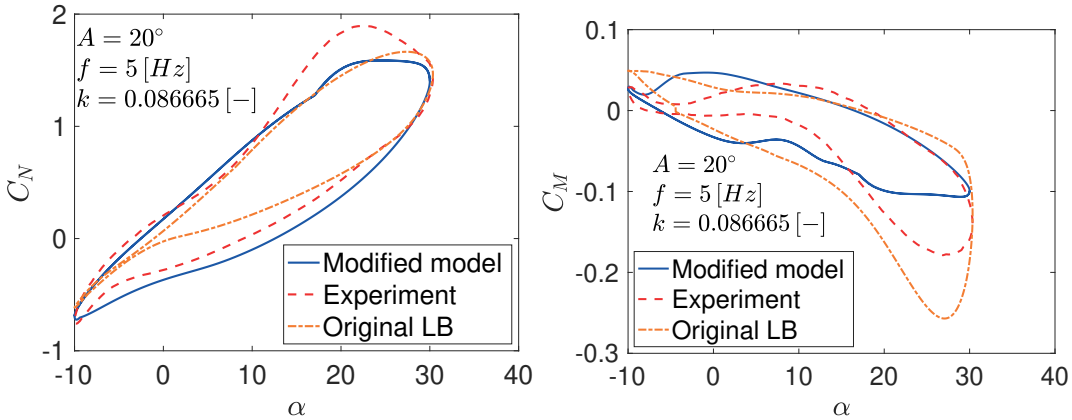

(g) Normal force

(h) Moment

FIGURE B.13: Comparison between the modified LB model and experimental results for the NACA0018 with $f = 5$ Hz.

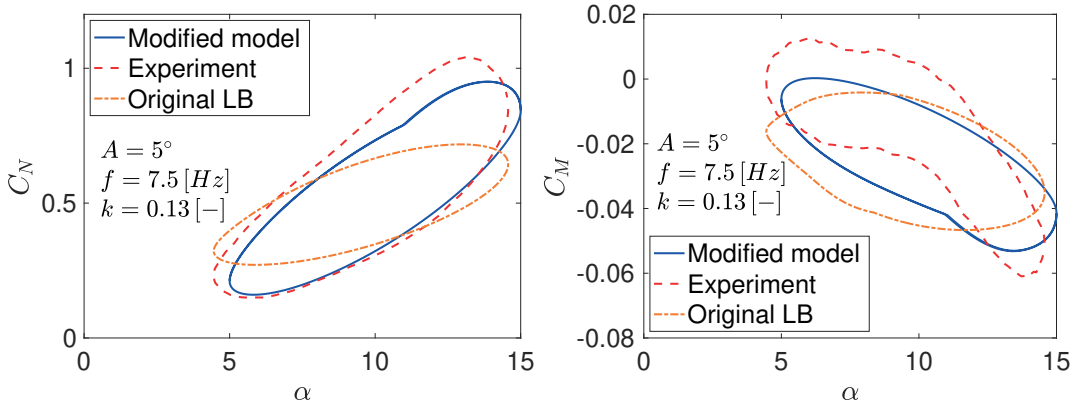

(a) Normal force

(b) Moment

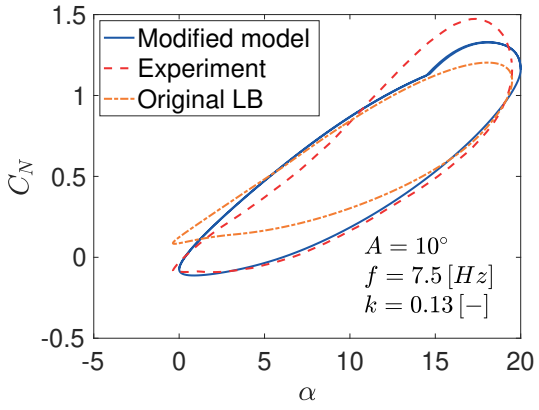

(c) Normal force

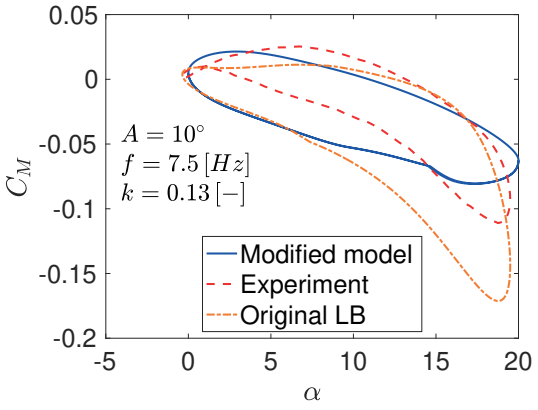

(d) Moment

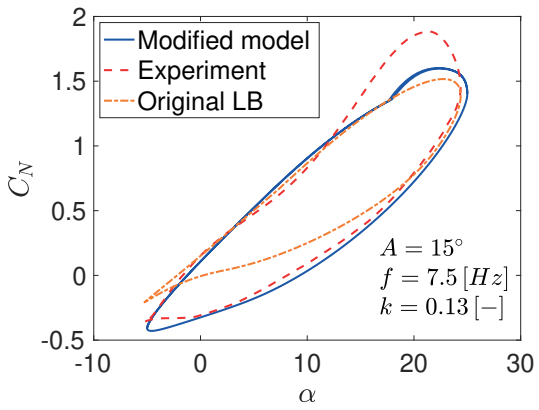

(e) Normal force

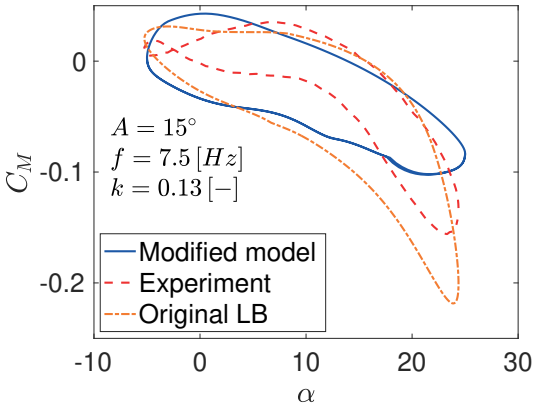

(f) Moment

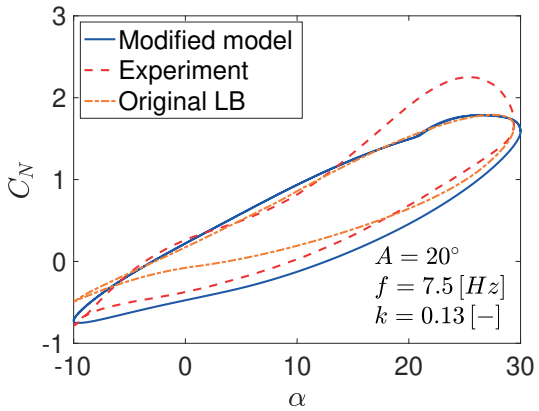

(g) Normal force

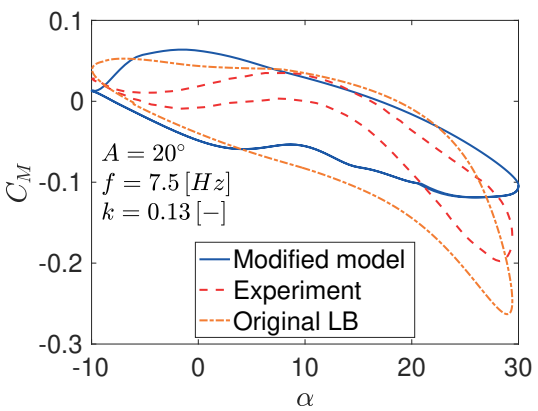

(h) Moment

FIGURE B.14: Comparison between the modified LB model and experimental results for the NACA0018 with $f = 7.5$ Hz.

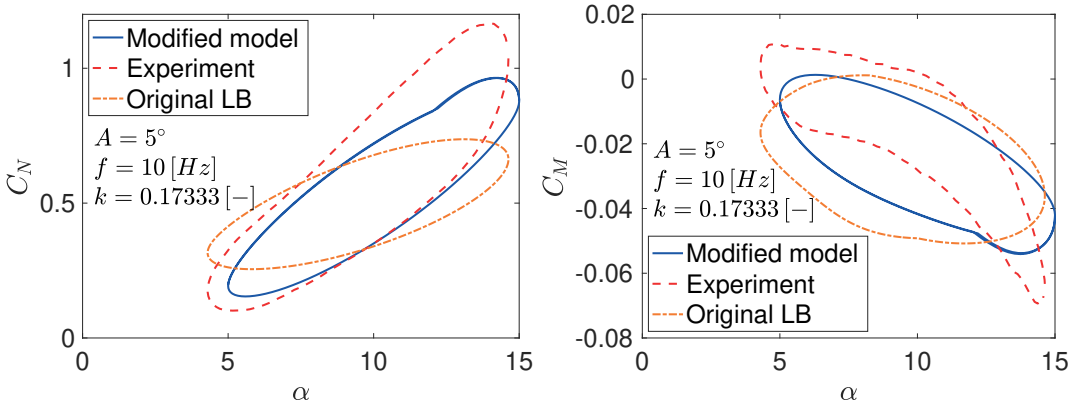

(a) Normal force

(b) Moment

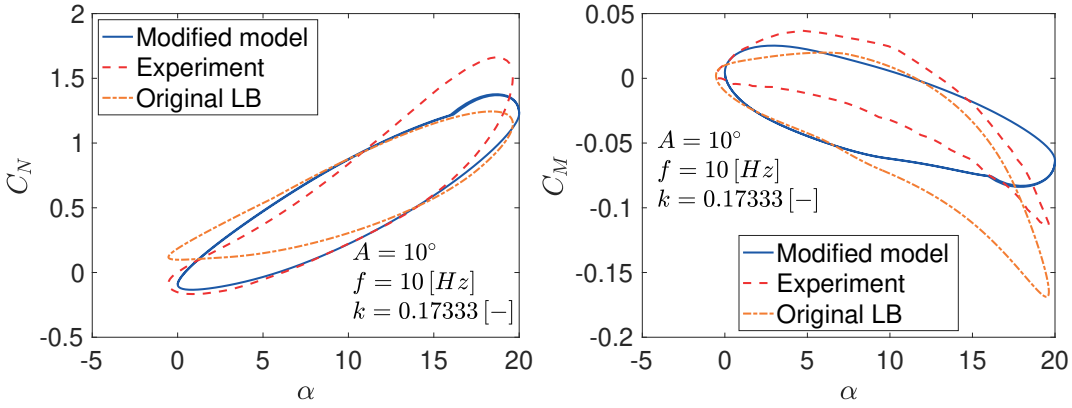

(c) Normal force

(d) Moment

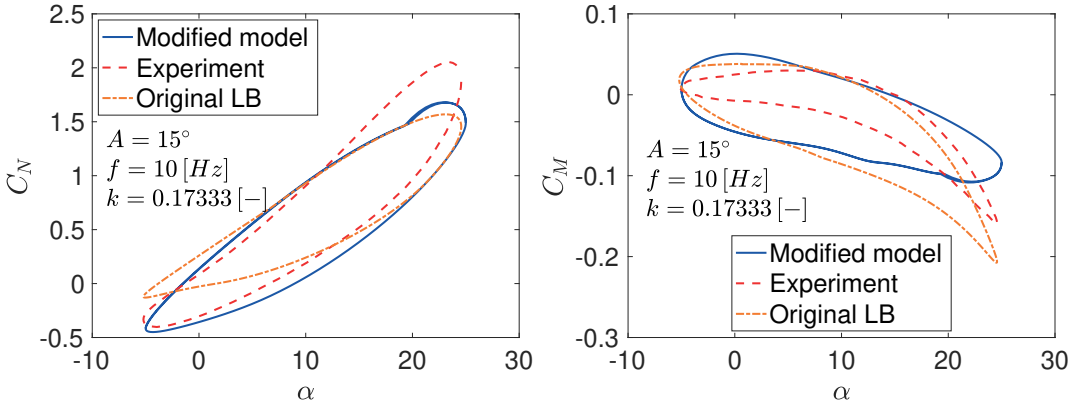

(e) Normal force

(f) Moment

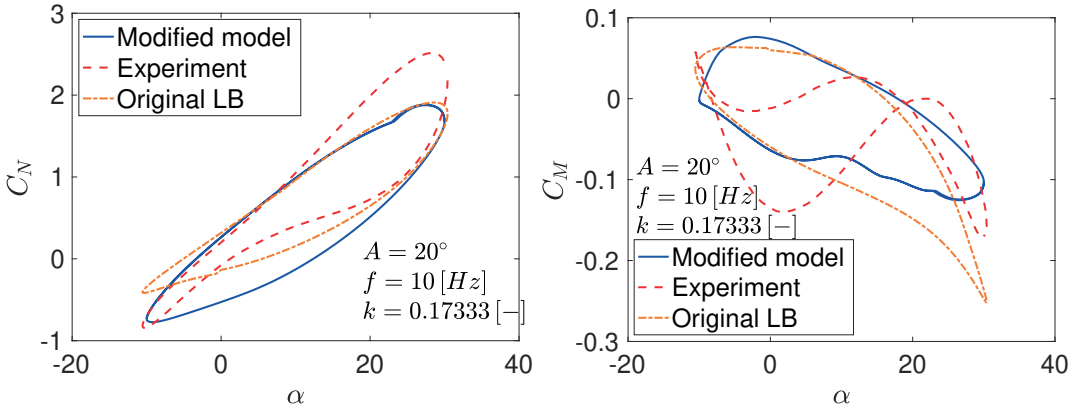

(g) Normal force

(h) Moment

FIGURE B.15: Comparison between the modified LB model and experimental results for the NACA0018 with $f = 10$ Hz.

Bibliography

[1] W. J. McCroskey, K. W. McAlister, L. W. Carr, and S. Pucci, "An experimental study of dynamic stall on advanced airfoil sections. volume 1. summary of the experiment.", NASA TM-84245, Tech. Rep., 1982.

[2] W. J. McCroskey, L. W. Carr, and K. W. McAlister, "Dynamic stall experiments on oscillating airfoils", *AIAA Journal*, vol. 14, no. 1, pp. 57–63, 1976.

[3] J. G. Leishman and T. Beddoes, "A semi-empirical model for dynamic stall", *Journal of the American Helicopter Society*, vol. 34, no. 3, pp. 3–17, 1989.

[4] R. Dat, C. T. Tran, and D. Petot, "Modèle phénoménologique de décrochage dynamique sur profil de pale d'hélicoptère", in *16e colloque d'aérodynamique appliquée*, Lille, France, Nov. 1979.

[5] K. W. McAlister, O Lambert, and D Petot, "Application of the onera model of dynamic stall", NASA-TP-2399, Tech. Rep., 1984.

[6] E. N. Jacobs, "The aerodynamic characteristics of eight very thick airfoils from tests in the variable density wind tunnel", NACA TR 391, Tech. Rep., 1932.

[7] C. Millikan and A. Klein, "The effect of turbulence: An investigation of maximum lift coefficient and turbulence in wind tunnels and in flight", *Aircraft Engineering and Aerospace Technology*, vol. 5, no. 8, pp. 169–174, 1933.

[8] G. B. McCullough and D. E. Gault, "The aerodynamic characteristics of eight very thick airfoils from tests in the variable density wind tunnel", NACA-TN-2502, Tech. Rep., 1951.

[9] D. E. Gault, "A correlation of low-speed, airfoil-section stalling characteristics with reynolds number and airfoil geometry", NACA TN-3963, Tech. Rep., 1957.

[10] B. W. McCormick, *Aerodynamics, aeronautics, and flight mechanics*. John Wiley, 1995.

[11] A. P. Broeren and M. B. Bragg, "Unsteady stalling characteristics of thin airfoils at low reynolds number.", *Progress in astronautics and aeronautics*, vol. 195, pp. 191–213, 2001.

[12] C. Bak, H. A. Madsen, P. Fuglsang, and F. Rasmussen, "Double stall", Forskningscenter Risoe-R 1043, Tech. Rep., 1998.

[13] J. Leishman, *Principles of Helicopter Aerodynamics*, ser. Cambridge Aerospace Series. Cambridge University Press, 2002, ISBN: 9780521523967.

[14] R. L. Halfman, "Experimental aerodynamic derivatives of a sinusoidally os- cillating airfoil in two-dimensional flow", NACA TN 2465, Tech. Rep., 1952.

[15] L. E. Ericsson and J. P. Reding, "Dynamic and static stall data in relation to airfoil stall at subsonic speeds", NASA CR-66787, Tech. Rep., 1969.

[16] L. E. Ericsson and J. P. Reding, "Dynamic stall simulation problems", *Journal of Aircraft*, vol. 8, no. 7, pp. 579–583, 1971.

[17] L. E. Ericsson and J. P. Reding, "Unsteady airfoil stall, review and extension", *Journal of Aircraft*, vol. 8, no. 8, pp. 609–616, 1971.

[18] N. D. Ham, "Aerodynamic loading on a two-dimensional airfoil during dynamic stall.", *AIAA Journal*, vol. 6, no. 10, pp. 1927–1934, 1968.

[19] L. W. Carr, K. W. McAlister, and W. J. McCroskey, "Analysis of the development of dynamic stall based on oscillating airfoil experiments", NASA TN-D-8382, Tech. Rep., 1977.

[20] N. D. Ham and M. I. Young, "Torsional oscillation of helicopter blades due to stall.", *Journal of Aircraft*, vol. 3, no. 3, pp. 218–224, 1966.

[21] J. M. Currier and K.-Y. Fung, "Analysis of the onset of dynamic stall", *AIAA Journal*, vol. 30, no. 10, pp. 2469–2477, 1992.

[22] R. B. Green and R. A. M. Galbraith, "Dynamic recovery to fully attached aerofoil flow from deep stall", *AIAA Journal*, vol. 33, no. 8, pp. 1433–1440, 1995.

[23] R. Ramsay, M. Hoffman, and G. Gregorek, "Effects of grit roughness and pitch oscillations on the s809 airfoil", National Renewable Energy Lab., Golden, CO (United States), Tech. Rep., 1995.

[24] A Choudhry, M Arjomandi, and R Kelso, "Estimation of dynamic stall on wind turbine blades using an analytical model", in *18th Australasian Fluid Mechanics Conference 2012, Launceston, Tasmania*, 2012.

[25] A. Choudhry, M. Arjomandi, and R. Kelso, "Horizontal axis wind turbine dynamic stall predictions based on wind speed and direction variability", *Proceedings of the Institution of Mechanical Engineers, Part A: Journal of Power and Energy*, vol. 227, no. 3, pp. 338–351, 2013.

[26] R. E. Gormont, "A mathematical model of unsteady aerodynamics and radial flow for application to helicopter rotors", Boeing Vertol Co Philadelphia Pa, Tech. Rep., 1973.

[27] F. J. Tarzanin, "Prediction of control loads due to blade stall", *Journal of the American Helicopter Society*, vol. 15, pp. 35–44, 1970.

[28] F. D. Harris, F. J. Tarzanin, and R. K. Fisher, "Rotor high speed performance, theory vs. test", *Journal of the American Helicopter Society*, vol. 17, pp. 33–46, 1972.

[29] R. L. Bielawa, S. Johnson, R. Chi, and S. Gangwani, "Aeroelastic analysis for propellers", NASA-CR-3729, Tech. Rep., 1983.

[30] S. T. Gangwani, "Prediction of dynamic stall and unsteady airloads for rotor blades", *Journal of the American Helicopter Society*, vol. 27, pp. 57–64, 1982.

[31] S. T. Gangwani, "Synthesized airfoil data method for prediction of dynamic stall and unsteady airloads", NASA-CR-3672, Tech. Rep., 1983.

[32] M. H. Hansen, M. Gaunaa, and H. A. Madsen, "A beddoes-leishman type dynamic stall model in state-space and indicial formulations", Tech. Rep., 2004.

[33] W Sheng, R. M. Galbraith, and F. Coton, "A new stall-onset criterion for low speed dynamic-stall", *Journal of Solar Energy Engineering*, vol. 128, no. 4, pp. 461–471, 2006.

[34] W Sheng, R. Galbraith, and F. Coton, "Prediction of dynamic stall onset for oscillatory low-speed airfoils", *Journal of Fluids Engineering*, vol. 130, no. 10, p. 101 204, 2008.

[35] W. Sheng, R. Galbraith, and F. Coton, "A modified dynamic stall model for low mach numbers", *Journal of Solar Energy Engineering*, vol. 130, no. 3, p. 031 013, 2008.

[36] W. Sheng, R. A. M. Galbraith, and F. N. Coton, "Applications of low-speed dynamic-stall model to the nrel airfoils", *Journal of Solar Energy Engineering*, vol. 132, no. 1, p. 011 006, 2010.

[37] G. R. Srinivassan, J. A. Ekaterinaris, and W. J. McCroskey, "Dynamic stall of an oscillating wing. part 1: Evaluation of turbulence models", *AIAA Applied Aerodynamics Conference, 11th, Monterey, CA, Aug. 9-11*, 1993.

[38] J. Ekaterinaris, G. Srinivasan, and W. McCroskey, "Present capabilities of predicting two-dimensional dynamic stall", AGARD, Tech. Rep. 552, 1995.

[39] A Spentzos, G. Barakos, K. Badcock, B. Richards, F. Coton, and R. Galbraith, "Computational fluid dynamics study of three-dimensional dynamic stall of various planform shapes", *Journal of aircraft*, vol. 44, no. 4, 2007.

[40] J. Anderson, *Fundamentals of Aerodynamics*. McGraw-Hill Education, 2010, ISBN: 9780073398105.

[41] A. Winkelmann, "An experimental study of separated flow on a finite wing", in *7th Atmospheric Flight Mechanics Conference*, 1981, p. 1882.

[42] A Winkelmann, "An experimental study of mushroom shaped stall cells", in *3rd Joint Thermophysics, Fluids, Plasma and Heat Transfer Conference*, 1982, p. 942.

[43] N. Gregory and C. O'reilly, "Low-speed aerodynamic characteristics of naca 0012 aerofoil section, including the effects of upper-surface roughness simulating hoar frost", R.M. 3726: Aeronautical Research Council, Tech. Rep., 1970.

[44] N. Gregory, V. G. Quincey, C. O'reilly, and D. J. Hall, "Progress report on observations of three-dimensional flow patterns obtained during stall development on aerofoils, and on the problem of measuring two-dimensional characteristics", C.P. 1146: Aeronautical Research Council, Tech. Rep., 1971.

[45] H. Sarlak, A. Frère, R. Mikkelsen, and J. N. Sørensen, "Experimental investigation of static stall hysteresis and 3-dimensional flow structures for an NREL S826 wing section of finite span", *Energies*, vol. 11, no. 6, 2018.

[46] S. A. Yon and J. Katz, "Study of the unsteady flow features on a stalled wing", *AIAA Journal*, vol. 36, no. 3, pp. 305–312, 1998.

[47] A. E. Winkelman and J. B. Barlow, "Flowfield model for a rectangular planform wing beyond stall", *AIAA Journal*, vol. 18, no. 8, pp. 1006–1008, 1980.

[48] "Reynolds-number effects in flow around more-or-less bluff bodies", *Journal of Wind Engineering and Industrial Aerodynamics*, vol. 89, no. 14, pp. 1267 –1289, 2001, Bluff Body Aerodynamics and Applications, ISSN: 0167-6105.

[49] M. Marinos, "Experimental and computational study of three-dimensional separation and its control using passive vortex generators", PhD thesis, National Technical University of Athens School of Mechanical Engineering Fluids Sector, 2013.

[50] P. Freymuth, "Three-dimensional vortex systems of finite wings", *Journal of aircraft*, vol. 25, no. 10, pp. 971–972, 1988.

[51] R. A. Piziali, "2-d and 3-d oscillating wing aerodynamics for a range of angles of attack including stall", NASA Technical Memorandum 4632, Tech. Rep., 1994.

[52] S. J. Schreck and H. E. Hellin, "Unsteady vortex dynamics and surface pressure topologies on a finite pitching wing", *Journal of Aircraft*, vol. 31, no. 4, pp. 899–907, 1994.

[53] D. Tang and E. Dowell, "Experimental investigation of three-dimensional dynamic stall model oscillating in pitch", *Journal of aircraft*, vol. 32, no. 5, pp. 1062–1071, 1995.

[54] P. Wernert, W. Geissler, M. Raffel, and J. Kompenhans, "Experimental and numerical investigations of dynamic stall on a pitching airfoil", *AIAA journal*, vol. 34, no. 5, pp. 982–989, 1996.

[55] F. Coton and R. M. Galbraith, "An experimental study of dynamic stall on a finite wing", *The Aeronautical Journal*, vol. 103, no. 1023, pp. 229–236, 1999.

[56] A Spentzos, G Barakos, K Badcock, B Richards, P Wernert, S Schreck, and M Raffel, "Cfd investigation of 2d and 3d dynamic stall", in *AHS 4th Decennial Specialist?s Conference on Aeromechanics, San Francisco, California*, 2004.

[57] J. G. Leishman and G. L. Crouse, "State-space model for unsteady airfoil behavior and dynamic stall", in *30th AIAA Structures, Structural Dynamics and Materials Conference*, Mobile, AL, Apr. 1989.

[58] W. T. Evans and K. W. Mort, "Analysis of computed flow parameters for a set of sudden stalls in low-speed two-dimensional flow", NACA TND-80, Tech. Rep., 1959.

[59] J. G. Leishman and T. S. Beddoes, "A generalised model for airfoil unsteady aerodynamic behaviour and dynamic stall using the indicial method", in *Proceedings of the 42nd Annual forum of the American Helicopter Society*, Washington DC, 1986, pp. 243–265.

[60] C. Chantharasenawong, "Nonlinear aeroelastic behaviour of aerofoils under dynamic stall", PhD thesis, Imperial College London (University of London), 2007.

[61] R. T. Jones, "Operational treatment of the nonuniform-lift theory in airplane dynamics", NACA-TN-667, Tech. Rep., 1938.

[62] Y. C. Fung, *An introduction to the theory of aeroelasticity*. Mineola, New York: Dover Publications, Inc., 1993.

[63] B. Lee, S. Price, and Y. Wong, "Nonlinear aeroelastic analysis of airfoils: Bifurcation and chaos", *Progress in aerospace sciences*, vol. 35, no. 3, pp. 205–334, 1999.

[64] T. Theodorsen, "General theory of aerodynamic instability and the mechanism of flutter", NACA-TR-496, Tech. Rep., 1935.

[65] A. Choudhry, R. Leknys, M. Arjomandi, and R. Kelso, "An insight into the dynamic stall lift characteristics", *Experimental Thermal and Fluid Science*, vol. 58, pp. 188–208, 2014.

[66] T. Lutz, W Würz, and S Wagner, "Numerical optimization and wind-tunnel testing of low reynolds number airfoils", in *Fixed and Flapping Wing Aerodynamics for Micro Air Vehicle Applications*, T. Mueller, Ed., vol. 195, Reston, VA: American Institute of Aeronautics and Astronautics, Inc., 2001, pp. 169–188.

[67] G. Dimitriadis, *Introduction to Nonlinear Aeroelasticity*. John Wiley & Sons, 2017.

[68] T. Theodorsen, "General theory of aerodynamic instability and the mechanism of flutter", NACA, Tech. Rep. NACA TR-496, 1935.

[69] R. T. Jones, "The unsteady lift of a finite wing", NACA, Tech. Rep. NACA TN-682, 1939.

[70] Y. C. Fung, *An Introduction to the Theory of Aeroelasticity*. Dover Publications, 1993, ISBN: 9780486678719.

[71] D. A. Peters, S. Karunamurthy, and W.-M. Cao, "Finite state induced flow models; part i: Two-dimensional thin airfoil", *Journal of Aircraft*, vol. 32, no. 2, pp. 313–322, 1995.

[72] E. H. Dowell, Ed., *A Modern Course in Aeroelasticity*, 4th. Kluwer Academic Publishers, 2004.

[73] E. Albano and W. P. Rodden, "A doublet-lattice method for calculating lift distributions on oscillating surfaces in subsonic flows", *AIAA Journal*, vol. 7, no. 2, pp. 279–285, 1969.

[74] J. Katz and A. Plotkin, *Low Speed Aerodynamics*. Cambridge University Press, 2001.

[75] M. Karpel, "Design for the active flutter suppression and gust alleviation using state-space aeroelastic modeling", *Journal of Aircraft*, vol. 19, no. 3, pp. 221–227, 1982.

[76] G. Dimitriadis, *Introduction to nonlinear aeroelasticity*. Chichester, West Sussex, UK: John Wiley & Sons, Inc., 2017.

[77] G. Dimitriadis, N. F. Giannelis, and G. A. Vio, "A modal frequency-domain generalised force matrix for the unsteady vortex lattice method", *Journal of Fluids and Structures*, vol. 76, pp. 216–228, 2018.

[78] E. Reissner, "Boundary value problems in aerodynamics of lifting surfaces in non-uniform motion", *Bull. Amer. Math. Soc.*, vol. 55, no. 9, pp. 825–850, Sep. 1949.

[79] M. G. Chopra, "Hydromechanics of lunate-tail swimming propulsion", *Journal of Fluid Mechanics*, vol. 64, no. 2, pp. 375–391, 1974.

[80] M. G. Chopra and T. Kambe, "Hydromechanics of lunate-tail swimming propulsion. part 2", *Journal of Fluid Mechanics*, vol. 79, no. 1, pp. 49–69, 1977.

[81] E. C. James, "Lifting-line theory for an unsteady wing as a singular perturbation problem", *Journal of Fluid Mechanics*, vol. 70, no. 4, pp. 753–771, 1975.

[82] A. R. Ahmadi and S. E. Widnall, "Unsteady lifting-line theory as a singular perturbation problem", *Journal of Fluid Mechanics*, vol. 153, pp. 59–81, 1985.

[83] T. Van Holten, "Hydromechanics of lunate-tail swimming propulsion. part 2", *Journal of Fluid Mechanics*, vol. 77, no. 3, pp. 561–579, 1976.

[84] P. J. Phlips, R. A. East, and N. H. Pratt, "An unsteady lifting line theory of flapping wings with application to the forward flight of birds", *Journal of Fluid Mechanics*, vol. 112, pp. 97–125, 1981.

[85] L. Dragos, "The theory of oscillating thick wings in subsonic flow. lifting line theory", *Acta Mechanica*, vol. 54, pp. 221–238, 1985.

[86] P. D. Sclavounos, "An unsteady lifting-line theory", *Journal of Engineering Mathematics*, vol. 21, pp. 201–226, 1987.

[87] M. Drela, "Integrated simulation model for preliminary aerodynamic, structural, and control-law design of aircraft", *American Institute of Aeronautics and Astronautics*, Structures, Structural Dynamics, and Materials and Co-located Conferences, 1999.

[88] M. R. Nabawy and W. J. Crowther, "On the quasi-steady aerodynamics of normal hovering flight part ii: Model implementation and evaluation", *Journal of The Royal Society Interface*, vol. 11, no. 94, p. 20 131 197, 2014.

[89] M. R. Nabawy and W. J. Crowthe, "A quasi-steady lifting line theory for insect-like hovering flight", *PLOS One*, vol. 10, no. 8, e0134972, 2015.

[90] J. Boutet and G. Dimitriadis, "Unsteady lifting line theory using the wagner function", in *55th AIAA Aerospace Sciences Meeting, SciTech 2017*, Grapevine, Texas, Jan. 2017.

[91] J. S. Izraelevitz, Q. Zhu, and M. S. Triantafyllou, "State-space adaptation of unsteady lifting line theory: Twisting/flapping wings of finite span", *AIAA Journal*, vol. 55, no. 4, pp. 1279–1294, 2017.

[92] A. M. Kuethe and C.-Y. Chow, *Foundations of Aerodynamics: Bases of Aerodynamic Design*, 4th ed. Wiley, Jan. 1986, ISBN: 9780471806943.

[93] H. Glauert, *The Elements of Aerofoil and Airscrew Theory*, 2nd ed., ser. Cambridge Science Classics. Cambridge University Press, Jul. 1983, ISBN: 9780521717342.

[94] R. T. Jones, "Operational treatment of the nonuniform-lift theory in airplane dynamics", NACA, Tech. Rep. NACA TN-667, 1938.

[95] G. Dimitriadis, J. Gardiner, P. Tickle, J. Codd, and R. Nudds, "Experimental and numerical study of the flight of geese", *Aeronautical Journal*, vol. 119, no. 1217, pp. 1–30, 2015.

[96] R. J. S. Simpson and R. Palacios, "Induced-drag calculations in the unsteady vortex lattice method", *AIAA Journal*, vol. 51, no. 7, pp. 1775–1779, 2013.